PHD

Fabrication and Applications of Low OH Photonic Crystal Fibres

Gris Sanchez, Itandehui

Award date:
2013

Awarding institution:
University of Bath

Fabrication and Applications of low OH Photonic Crystal Fibres

submitted by

Itandehui Gris Sánchez

for the degree of Doctor of Philosophy

of the

University of Bath

Department of Physics

November 2012

Contents

A mis padres María Luisa y Zótico y
a mi hermana Ireri
A Carles

Acknowledgements

I would like to express my most sincere gratitude to my supervisor, Jonathan Knight for his continued guidance, advice and support during this time.

I am grateful and I feel fortunate of having had the chance to explore new territories in life growing in many senses, thanks to all who have contributed to that. Thanks to my mexican cultural background which has inspired and nurtured my dreams many times.

I would like to acknowledge my sponsor CONACyT (National Council of Science and Technology of Mexico) for the support granted.

A fun and inspiring dog character should be thanked, Mina for all the fun and good times.

An immense and warm thank you to my parents María Luisa and Zótico and to my sister Ireri, for your constant love, support and guidance, you are always with me.

My deepest thanks to Carles, for your love and patience and for being part of my life.

Abstract

The aim of this thesis is to consistently fabricate low OH content silica solid-core photonic crystal fibres of different core diameters, identified as low spectral attenuation at 1383 nm. Three different methods are proposed. Two of them are focused on preventing the OH contamination of glass during fabrication whilst the third method is focused on obtaining low OH fibres by reducing the OH content of already contaminated glass. The local attenuation at the ends of these low OH fibres is notoriously worsen when they are exposed to the atmospheric water vapour, the levels of this attenuation depending very strongly with core diameter. The low OH levels achieved (0.19 ppm) in the small-core photonic crystal fibres open the scope to applications in non linear optics where standard levels of absorption are detrimental. In particular, the principle of a widely tunable source (across the OH absorption peak at 1383 nm) delivering femtosecond pulses beyond 2 μm is demonstrated experimentally.

Chapter 1

Introduction

Glass is used as a base material in a vast diversity of areas that include life sciences, aerospacial instruments, photonic devices, telecommunications and more recently display technologies, to mention some. The extensive use of glass has also entailed a continued investigation in fundamental materials science allowing innovation in glass properties and fabrication processes. This has provided a solid platform for the mentioned technologies, and specially to what concerns this thesis photonic crystal fibre fabrication. Silica glass is the most common material used for the fabrication of optical fibres.

Optical fibres are a fundamental part of modern life and one of the major breakthroughs of the last century, they have even transformed the way we communicate. The fibres used in today's telecommunications systems are fabricated to high standards by automated and well controlled processes using the highest quality materials. As a result optical fibres have reached an extremely high performance which includes ultra low loss and low OH content [1], high mechanical strength and even resistance to ageing due to hydrogen diffusion [2].

The requirements and specifications of new optical fibre applications demand more versatility to manipulate light that challenge the capabilities of standard optical fibres. Photonic crystal fibres have enabled ways to manipulate light not possible before and have become a more solid technology. One of the main drawbacks of photonic crystal fibre (PCF) current fabrication processes is the difficulty of repeatability because such processes are not as refined as for standard fibres. The most common PCF fabrication technique, *stack and draw*, involves hand made construction of the preform which might introduce changes in the process and fabrication conditions. Also small variations of the fabrication conditions can induce changes in the fibre structure and glass properties, bearing changes in the refractive index of the material and consequently modifying the optical properties of the fibre. The motivation of the present work has been to obtain consistently low OH content PCF's by means of a

thorough control of the fabrication process. This investigation led to the identification of different fabrication conditions (i. e. humidity, processing time and thermal treatments) and their impact on the fibre transmission performance (i.e. losses).

Interestingly the first demonstration of light guiding was observed in water jets [3], and its precisely the aim of this thesis to minimize the interaction of silica glass PCF's and water vapour present in laboratory. In optical fibres the absorption due to OH is well known, it has motivated research in materials properties and the optical fibre fabrication. By improving losses in optical fibres their use can be extended, in this thesis small-core PCF's were used as part of a tunable soliton source.

1.1 Thesis structure

As described in this chapter, the work compiled in this thesis spans from the low OH PCF's fabrication processes to the use of low OH small-core fibres in tunable pulsed sources. It gathers together the fabrication processes description, characterisation and analysis of the transmission and attenuation spectra of fibres fabricated under different conditions and the applications of low OH content PCF's. It comprises a collection of PCF fabrication experiments to obtain low losses and low absorption at OH related wavelengths. The proposed fabrication methods have proved to effectively reduce the fibre absorption caused by OH contaminants allowing the use of PCF's in even wider range of applications and wavelength ranges.

Chapter 2 provides an introduction to silica glass and its properties as well as the nature of intrinsic or induced defects, in silica glass fibres and the absorption bands related to them. The implication of such defects in the formation and diffusion of OH in the silica network is also described.

Chapter 3 introduces the stack and draw PCF fabrication technique used to obtain the fibres fabricated for this thesis. The different loss mechanisms are also summarised along with the existent techniques to measure losses in optical fibres.

In Chapter 4 three methods to fabricate low OH PCF's are presented describing the effects on PCF's attenuation of moisture in the laboratory during fabrication, the effects of the processing time and those of the annealing. The solid-core PFC's (SC-PCF's) and the fabrication processes were fabricated and designed by the author of this thesis. The attenuation obtained for small-core SC-PCF's using the annealing fabrication method has been remarkably low, and for a 2 μm core SC-PCF at the first OH-stretching overtone (1383 nm) is the lowest reported to the date. Using this fabrication method low OH levels were consistently achieved in SC-PCF's.

The effects on the absorption at OH related wavelengths of solid and hollow-core low OH

PCF's with unsealed ends exposed for several weeks to the moisture present in laboratory environment are presented in Chapter 5. The degradation of the fibres' performance over time and the localization of OH contamination on the fibre ends are analysed. It is also shown that water vapour is present in the holes of the fibre structure as well as in the laboratory.

Chapter 6 begins by introducing the nature of soliton self-frequency shift (SSFS) and applications of SSFS in diverse fields. The experimental characterisation of the fibre group velocity dispersion supported by numerical calculations is also presented. The demonstration of a widely tunable source using low OH small-core PCF carried out in collaboration with Stephen A. Dekker and other members of the Centre for Ultrahigh Bandwidth Devices for Optical Systems (CUDOS) research group at University of Sidney is presented too. The tuning range is the widest obtained so far for tunable sources using SSFS. Finally the generation of solitons by SSFS beyond 2 μm is demonstrated in low OH PCF's by the author.

A summary of the results obtained in this thesis is presented in Chapter 7, it also includes perspectives of future work related to fibre fabrication and materials. The results presented in this thesis have been published in peer reviewed journals and are listed in Appendix A.

Chapter 2

Silica glass: structure, defects, "water" diffusion and OH groups

In this chapter the author will introduce the characteristics of silica glass and will provide a description of the defect points found in silica which are related to optical absorption observed in spectral attenuation of the fibres fabricated for this thesis. Formation and diffusion of OH have been a long standing problem in optical fibres transmission performance and is introduced here too.

2.1 Silica glass structure

Silica glass is an amorphous three dimensional structure (or random network [4]) whose basic component is the tetrahedron SiO_4 that has a silicon atom in the centre bonded to four oxygen atoms [5], represented schematically in Figure 2-1. Commonly two oxygen atoms of the tetrahedra are shared with other SiO_4, leading to the chemical formula: SiO_2, also known as amorphous silicon dioxide, fused silica, silica glass or simply silica. It is widely accepted that lengths between Si−O, O−O and Si−Si are 1.58 Å , 2.6 Å and 3.2 Å respectively [6]. The angle between Si−O−Si can vary between 120° and 180° [4, 7]. The thermal properties can change according to the type of glass. In this case the softening temperature and annealing temperature of the glass used to fabricate the photonic crystal fibres investigated in this thesis are specified by the manufacturer [8] to be 1600°C and 1120°C respectively. Thanks to its mechanical strength which arises from the covalent bonds,

low electrical conductivity and transparency ranging from the ultraviolet to the infrared (determined by the wide bandgap of ∼9eV [9, 10]) silica use has expanded to optoelectronics, microelectronics and as the main material for optical fibre fabrication and derived devices such as optical amplifiers, fibre lasers or wavelength filters. Manufacture costs of glass are low compared to crystals because silica glass preparation can be carried out in a shorter time scale making the mass fabrication costs feasible for glass industry. The difficulty of investigating non-crystalline materials (i.e. silica) lies in the fact that a periodic unit cell can not be defined, as opposed to in crystals. Consequently the understanding of the physics behind amorphous structures is somewhat limited compared to that of crystals. The structure of silica has been described as a continuous random network (CRN) [4, 11] using techniques based on neutron scattering and X-rays. In this model the basic structural unit of silica is the same as for α-quartz (crystal) so that in the short range both forms of SiO_2 amorphous and crystalline have similarities in their properties (transparency, mechanical strength and low electrical conductivity). Silica has been frequently used as a model to study amorphous materials because of its simple chemical structure. The origin of defect points and their effect on silica properties in particular, has attracted the attention of many researchers. Such defects are mainly associated with optical absorption (OA) and photo-luminescence (PL) and are described in the following section.

In this thesis, the method used to obtain information about the characteristics of the silica glass fibres was by the study of the optical absorption or attenuation obtained by the cutback technique (explained in Chapter 3) after the transmission measurements. Changes in fabrication method are reflected in the absorption features of the attenuation spectrum. The spectral absorption features were observed to be related to the different fabrication processes.

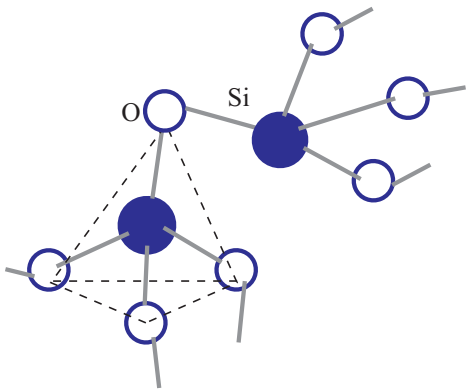

Figure 2-1: Representation of the tetrahedra model for SiO_2. White circles represent oxygen and blue circles represent silicon.

2.2 Silica point defects

A point defect in an amorphous material described as a CRN is an irregularity in the structure and the typical dimensions of the defect are of the order of the interatomic distance. Defects can be classified as intrinsic or extrinsic. The first type consists of the material components only, an example of these point defects are atom vacancies, and the latter includes atoms different from the material composition, in silica glass the most common being OH or chloride impurities. It is well known that radiation of different kinds (UV, X, γ, and β rays) can damage the silica network creating defects [9, 12] determined by the type of material and irradiation and on the irradiation energy [13]. Another cause of the formation of point defects in silica is the rapid change in temperature during glass formation, as in the case of silica optical fibre fabrication. The rapid changes in temperature also create mechanical stresses [14, 15]. Several types of defects have been found in silica and are classified as dangling defects [16] or as oxygen defect centres (ODC) related to the photosensitivity of silica [17–19]. Defects in silica affect its chemical stability thus affecting its guiding and mechanical properties. There are various methods and techniques to investigate point defects and their effects on the material properties. Electron paramagnetic resonance (EPR) spectrometry is used to identify paramagnetic defects (E' centres, non bridging oxygen hole centres (NBOHC), peroxy radicals (POR), and self-trapped holes [17]) which give place to optical absorption. Research on the radiation induced defects on GeO_2 silica glass is still on going [13].

In optical fibres different defect centres have been examined using techniques like electron spin resonance (ESR) [20], optical absorption [21] and photoluminescence [22]. Losses observed in optical fibres are closely related to point defects. In particular the spectral features observed in the absorption of the optical fibres fabricated for this thesis are related to the E' centres and the NBOHC described in the following section.

2.2.1 E' centres

The E' centres are point defects that consist of an unpaired silicon electron also known as *dangling* silicon defect commonly represented as $\equiv$Si$\bullet$ where silica is bonded to three other oxygens denoted as "$\equiv$" and the "$\bullet$" represents the unpaired electron [17]. There are different types of E' centres [17, 23–25] the most common being the so called E'$_\gamma$. One of the classifications of the E' centres is based on historical perspective. All other classification is based on the type of irradiation to induce the E' centres and on the material used [5, 18]. Although there is still theoretical work in progress in order to determine the structure of these defect centres, one of the most accepted models to describe the E' defect centres structure was proposed by Griscom et al. [24]. The model consists of an electron trapped in non

bonding sp^3 hybrid orbital on a silicon at the site of an oxygen vacancy. E' centres were first observed in α-quartz [23, 26], and based on the similarities of the hyperfine structures measured by ESR it was concluded that the E'$_\gamma$ defect centres in quartz are essentially the same in silica glass [5, 24]. The optical absorption band associated to the E'$_\gamma$ centres is 213.7 nm (5.8eV) [18].

In optical fibres the formation of the E' defect centres occurs both in the neck down region of the preform whilst in the furnace (during the fibre draw) where a rapid change of temperature takes place, freezing the defects that form at high temperatures [27, 28], and afterwards during the cooling process. The E' defects in fibres are therefore a result of the whole drawing process. Concentration of E' centres is greater on the surface than in the centre of the fibres because the cooling down rate or quenching rate is faster on the surface than in the centre of the preform. While recombination of defects slows down as the glass surface cools, the recombination in the central region continues at higher rate because the quenching rate is slower. The recombination probability of the E' centres is inversely proportional to the cooling down rate. The number of E' centres depends on the thermal history of the fibre preform [29] determined by fabrication parameters, such as core diameter [27, 29, 30], draw speed and drawing temperature [27, 28].

2.2.2 Non bridging oxygen hole centres

Non bridging oxygen hole centres, also known as dangling oxygen defects, represented as (≡Si−O•), are classified together with the E' centres and peroxy radicals (POR) as dangling defects [16]. Oxygen sites in silica are potential precursors of E' centres (≡Si•) and NBOHC (≡Si−O•), this process can be represented by the equation 2.1 [17, 31, 32]:

$$\equiv \mathrm{Si{-}O{-}Si} \equiv \rightarrow \equiv \mathrm{Si{-}O}\bullet^{+} \bullet \mathrm{Si} \equiv \tag{2.1}$$

From this equation it can be inferred that when one precursor breaks (i.e. a strained Si−O−Si) an E' centre and a NBOHC appear.

Another NBOHC formation mechanisms exist in addition to the breakage of a strained Si−O−Si bond, for example by breaking a peroxy linkage, described by equation. 2.2 [16], or by breaking an O−H bond in a silanol group as shown in equation 2.3 [16]:

$$\equiv \mathrm{Si{-}O{-}O{-}Si} \equiv \rightarrow \equiv \mathrm{Si{-}O}\bullet^{+} \bullet \mathrm{O{-}Si} \equiv \tag{2.2}$$

$$\equiv \mathrm{Si{-}O{-}H} \rightarrow \equiv \mathrm{Si{-}O}\bullet^{+}\mathrm{H} \tag{2.3}$$

It was observed by Hibino et al. [33] that the NBOHC formation (also known as colour

centres [21]) in optical fibres consists on the breakage of Si−O bonds induced by the draw tension that creates shear stress σ in the neck down region, the shear stress is expressed in equation 2.4,

$$\sigma = \frac{F}{A} \tag{2.4}$$

where F is the drawing tension and A the cross sectional area of the neck down region [33]. For a constant tension the shear stress and therefore the formation of NBOHC increases as the fibre diameter decreases.

By loading fluorine or hydrogen in the silica network the dangling Si• or O• bonds can be terminated to reduce the number of defects [34] improving the the resistance to radiation. In the case of hydrogen loading it can lead to formation of silanol groups worsening the fibres performance in the visible and near-IR wavelengths. Annealing on the other hand relaxes the silica matrix reducing defects and eliminating OH [27, 35–38]. Both the annealing process and number of OH groups in silica are influenced by the presence of small molecules like hydrogen, oxygen and water according to Nuccio et al. [39]. Diffusion of water, its reaction with silica glass, subsequent formation of OH groups (silanol) and the impact on glass properties is of great importance for optical fibres.

2.3 "Water" diffusion into silica glass

Diffusion in solids is the transport of molecules from one region to another driven by the gradient of concentration. Adolf Fick introduced the idea of the diffusion coefficient D and proposed a linear empirical relation between the flux and gradient concentration of the diffusing particles, known as Fick's first law, expressed in equation 2.5 [38, 40]:

$$J_x = -D\frac{\partial c}{\partial x} \tag{2.5}$$

where J_x is the flux of the diffusing particles (molecules, atoms or ions) and $\partial c/\partial x$ is the concentration gradient in the diffusion direction x [41]. The concentration gradient increases in opposite direction to the diffusing flux indicated by the negative sign. The flux J_x units are mol/m^2/s (moles per unit area per unit time), concentration c is the number of particles per volume and the diffusivity D is in m^2/s [40].

Another aspect of the diffusion coefficient D is its dependence on temperature, D generally follows the Arrhenius relation 2.6 [40]:

$$D = D_0 exp(-\frac{Q}{k_B T}) \tag{2.6}$$

where the Q is the activation enthalpy of diffusion, k_B the Boltzman constant, T the absolute temperature and D_0 a factor also known as *frequency factor*. D_0 and Q are called *activation parameters of diffusion* and depend on the solid composition and on the diffusing molecule and are temperature independent [40, 42].

Microscopically, the diffusion process is driven by the *Brownian motion* of atoms and molecules [43, 44]. Some of the possible diffusion mechanisms described to date are: interstitial (also known as direct interstitial), collective (direct exchange or ring mechanism), vacancy (dominant in metals), divacancy, interstitialcy, and interstitial-substitutional exchange mechanisms [40]. The interstitial mechanism, illustrated in Figure 2-2, is the simplest of the diffusion mechanisms, it does not require a defect to activate the diffusion mechanism. Because of this, the diffusion coefficient tends to be high for small migrating atoms like H, C, N and O [40]. The mechanism consists of the incorporation of the diffusing particles in interstitial sites of the host material lattice. The subsequent diffusion of the solute is given by the jumps to nearby interstitial sites [40]. The vacancy diffusion, illustrated in Figure 2-3, is the jump of the solute to an adjacent vacancy, for example dangling defects in silica.

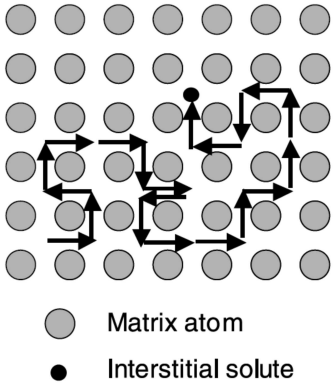

Figure 2-2: Illustration of interstitial diffusion mechanism (after reference [40]).

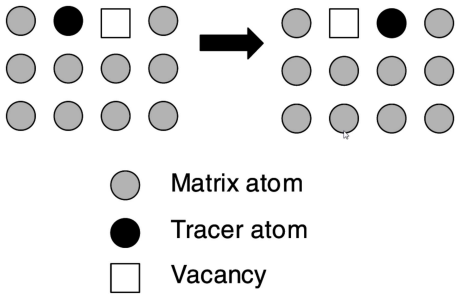

Figure 2-3: Illustration of vacancy diffusion mechanism (after reference [40]).

Diffusion species in silica can be classified according to their type [45] or interaction with the host material [6]. Noble gases have low interaction with the silica network. The interaction of molecular gasses like H_2, O_2 and HF for example, is weak whereas the interaction of anions (e.g. OH^-, Cl^-, F^-) with silica glass is classified as strong. Other diffusing species are the so-called network constituents (e.g. GeO_2, B_2O_3, H_2, P_2O_5) and network modifiers (e.g. AlO_3, rare earths, heavy metal oxides as impurities). The diffusion of the above species contribute greatly to modifying silica properties like electrical conductivity, viscosity and optical absorption [46].

The openness of the material structure, vacancies or defects and their size as well as the mass, charge, and size of the diffusing particles are characteristics that define the diffusion process itself [6]. Silica glass is a porous structure in which small molecules can diffuse rapidly through the silica lattice (i.e. ions or molecular gases) [47]. Diffusion of ions, (i.e. OH diffusion in silica) is mainly based on chemical reactions or exchange mechanisms [14], illustrated in Figure 2-4.

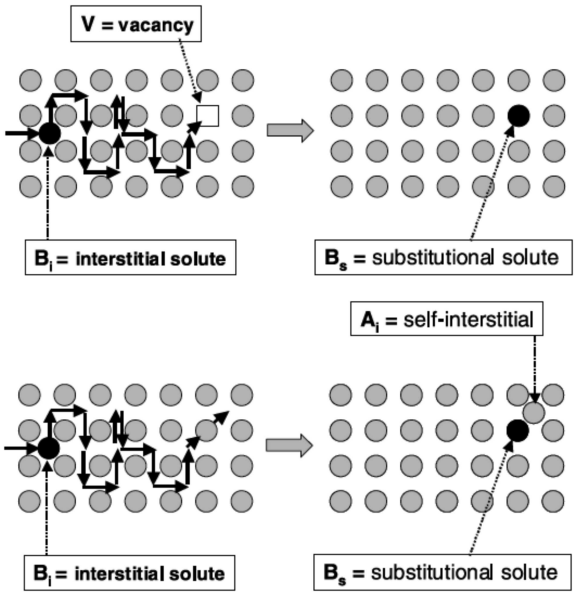

Figure 2-4: Illustration of exchange difusion mechanism (interstitial-substitutional). Top: dissociative mechanism. Bottom: kick-out mechanism (after reference [40]).

Diffusion of water in glass was identified in the 1950's by Moulson [48]. Later in 1978 OH groups in silica glass optical fibres were observed to modify the numerical aperture and in general related to worsening of the fibre performance [49]. Diffusion is a complex and widely investigated mechanism. A particular case of diffusion in silica glass is that of OH ions

commonly referred to as "water" diffusion. The diffusion of water in silica is of particular interest and relevance for its use in technological applications like optical fibres or planar waveguides [45]. Hydrolysis is the reaction of water vapour H_2O_{vapour} with the silica surface or siloxane Si−O−Si. This reaction, shown in equation 2.7, is energetically more favourable on strained Si−O−Si bonds because the stress reduces the bonding energy [50]. In molten glass, surface energy (surface tension) is lower compared to vitreous silica and gets covered by silanol groups (Si−OH) [35, 51–53] very rapidly just after its formation [47].

$$H_2O_{vapour} + \equiv Si{-}O{-}Si \equiv \rightleftarrows 2(\equiv Si{-}O{-}H)_{glass} \tag{2.7}$$

The "residual valences" of siloxane [35] react with water vapour at room temperature to form silanol groups. The hydroxylated surface (surface covered with silanol groups) has high chemical reactivity and its stability depends heavily on OH concentration and on temperature [54]. Once the water vapour is dissociated on the silica surface the diffusion of OH carries on.

The fact that the reaction in equation 2.7 has very little change in enthalpy makes the process reversible almost entirely by annealing. Dehydroxylation ($2\,SiOH \rightarrow Si{-}O{-}Si + H_2O$) [54] is the process to reduce the OH on the silica surface. OH content in silica glass has been observed to reduce under annealing treatments [37, 39, 54].

After experimental observations Davis et al. [55] proposed two scenarios to explain water diffusion in silica determined by temperature and structural relaxation. One assumes high temperature (850°C) at which silica glass relaxation and reaction occurs rapidly compared to the time it takes water to diffuse. In this case the diffusion mechanism can be approached by Doremus model. In this model the molecular water vapour diffuses through silica and penetrates it until it finds a defect or strained site to react with, forming silanol [56]. The other is based on Fick's diffusion model and assumes temperatures <850°C in which the relaxation and reaction times are slower compared to the diffusion times limited only by the diffusion coefficient D, assuming movement of H_2O molecules with no reaction.

Solubility and diffusion of water species in silica, namely OH groups, depend on concentration and on the thermal history of the glass [14, 57] (i.e. glass relaxation [55]). Solubility is inversely proportional to the size of the diffusing molecule [47]. Sudden changes in temperature can cause defects making OH more readily soluble [6]. Reducing the fictive temperature will help to reduce the number of sites where OH can bond thus reducing the solubility [58]. Fictive temperature (T_f) is the temperature at which glass forms and depends on how fast the glass cools down when it forms. T_f is a parameter used to characterise the state of the glass [6, 41, 59–61].

2.3.1 OH groups in silica glass

A hydroxyl (OH), which is a substructure of the water molecule, bound to a silicon atom forms silanol [35], represented as Si−O−H. Silanol groups are commonly referred to as *OH groups* only. Silanol groups are an extrinsic type of defect in silica bulk. The transmission properties of silica fibres are strongly degraded by the presence of OH groups on the silica surface or in the bulk and observed as abortionist at different wavelengths in the transmission spectrum.

Using Raman and infrared spectroscopy techniques the fundamental absorption band of the OH stretching groups in silica glass has been widely studied in silica bulk [62–67]. The structure of the fundamental and overtone OH-stretching absorption bands, which depend on the interaction of the hydroxyl with the silica network, have been investigated more recently by comparing numerical (quantum-mechanical calculations) and experimental work [67]. The shape of the mentioned absorption band does not depend on OH concentration nor on the fabrication technique used to obtain the glass [67] in the concentration range from 10^{-1} ppm and 10^{3} ppm (parts per million per weight) of OH in silica glass. The OH concentration in the fibres fabricated for this thesis lies within that range. The OH-stretching fundamental absorption band in silica is located at 3672 cm^{-}1 (2723 nm). It can be decomposed into different absorption components (Gaussian and Voigt components [67]). The different absorption bands are identified in the list below according to their interaction with the silica network and other OH groups. Although the standard units for the spectroscopic absorption measurements are cm^{-1} for consistency with this thesis the values of the absorption bands are also presented in nm:

- Absorption band at 3690 $\pm$2 cm^{-1} ($\sim$ 2710 nm) corresponds to free OH groups. These groups do not interact with other OH groups and are only bonded to the silica network by the oxygen as illustrated in Figure 2-5 denoted as ω_0.
- Absorption band at 3660 $\pm$4 cm^{-1} ($\sim$ 2732 nm) corresponds to OH groups bonded weakly to a bridging oxygen ω_1 (see Figure 2-5) and to hydrogen bonded OH groups (clusters with no rings) in linear configuration ω_3.
- Absorption band at 3630 $\pm$6 cm^{-1} ($\sim$ 2754 nm) corresponds to OH groups hydrogen bonded to a bridging oxygen (i.e. ≡Si−O−Si≡) (ω_2) and to OH groups (clusters forming rings) hydrogen bonded in a linear configuration (ω_4) as seen in Figure 2-5.
- Absorption band at 3565 $\pm$14 cm^{-1} ($\sim$ 2805 nm) corresponds to OH groups hydrogen bonded in a cyclic configuration (in phase or ω_5 and out of phase ω_6) (see Figure 2-5).

The four components of the fundamental OH-stretching absorption band are found in different fractions in the glass, and the intensity of the IR absorption for each groups is also

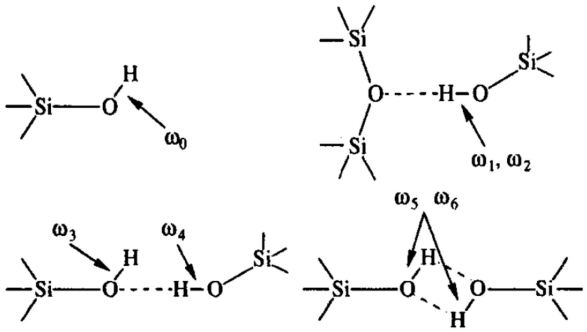

Figure 2-5: Representation of different OH configurations in silica glass (from reference [67]).

different. Free OH groups are the most abundant whilst the most absorptive OH groups are those which are hydrogen bonded [67]. Therefore OH concentration is not equivalent to IR absorption strength, this depends on the type of OH group.

Also for the first OH-stretching overtone centred at 1.38 μm, the absorption band components have been identified according to their configuration and interaction with silica. The component corresponding to the free OH groups is found at 1381 nm. At 1391 nm is the overtone of the OH groups interacting with other OH groups and at 1412 nm is the overtone of the OH groups interaction with the silica network [68]. The classification and notation used to describe OH groups in silica is presented in different forms at slightly different wavelengths according to various authors, for the sake of clarity a summary of the suggested absorption bands for different OH groups configurations is presented in table 2.1.

Name [67]	Fundamental absorption (nm) [67]	Name [64],[68]	Fundamental absortpion (nm) n=1 [64]	1^{st} stretching overtone (nm) n=2 [64]	1^{st} stretching overtone (nm) n=2 [68]
ω_0	2710	n$\widetilde{\nu}_1$(OH)	2710	1377	1381
ω_1, ω_3	2732	n$\widetilde{\nu}_2$(OH)	2728	1385	1391
ω_2, ω_4	2754	n$\widetilde{\nu}_3$(OH)	2766	1385	1412
ω_5, ω_6	2805	n$\widetilde{\nu}_3$(OH)	2849	-	-

Table 2.1: **Comparisson of absorption wavelengths of OH in silica according to different authors.**

In photonic crystal fibres, apart from the first OH-stretching overtone in silica bulk, another two absorption bands relating to surface OH (SiOH) have been reported, one at 1364 nm and the other at 1390 nm. The absorption bands correspond to the first overtones of non-hydrogen bonded OH and hydrogen bonded OH to the silica surface respectively [69, 70], illustrated in Figure 2-6.

Because the silicon atoms on the silica surface are not in an equidistant arrangement

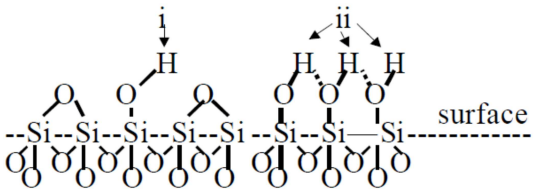

Figure 2-6: Illustration of nonhydrogen (i) and hydrogen (ii) bonded OH groups configurations on silica surface (From reference [69]).

(as in a crystal) the OH attached to the surface will be distributed with various distances to other OH groups. Therefore, the chemical properties and the IR absorption will differ depending on the configuration of the OH groups formed. Figure 2-7 illustrates different possible configurations of OH on a silica surface . Configurations F and G have been used to explain experimental data (related to the identification of different OH groups on silica surface [35]), although further condensation of the OH groups is possible, which simplifies the configuration into Si−O−H again.

The number of OH groups in silica particles formed in water is affected by various factors, one of them depends on the location of the OH in the silica surface [35]. This is illustrated in Figure 2-8A, "buried" OH distorts the surface and can only be removed by annealing at high temperatures. In small radii silica particles (<100nm) the OH groups are easier to remove because they are held farther apart, as illustrated in Figure 2-9a. In large radii particles (e. g. flat surfaces see Figure 2-9b) OH can form more stable hydrogen bonded pairs. Dehydration at the contact points of silica particles where there is a negative radii of curvature, illustrated in Figure 2-9c, is harder.

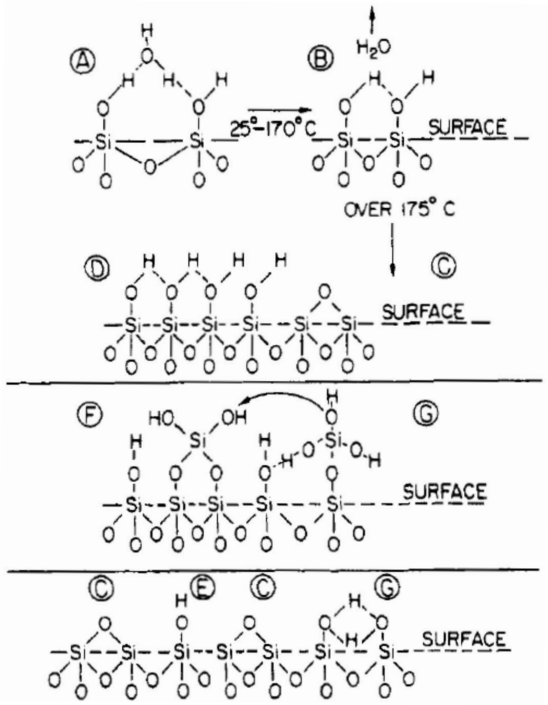

Figure 2-7: Representation of different proposed configurations of OH on silica surface. *A*, vicinal hydrated, *B* vicinal anhydridus, *C* siloxane-dehydrated, *D* hydroxilated surface, *E* isolated, *F* germinal, *G* vicinal hydrogen bonded. *F* and *G* probably do not exist on a dried surface (from reference [35]).

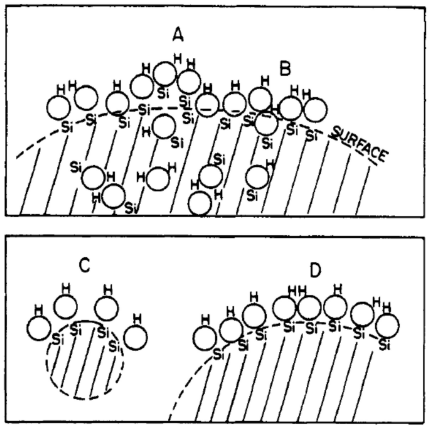

Figure 2-8: Representation of different factors that affect OH distribution on silica particle formed in water (from Reference [35]). *A*, "buried" OH; *B*, OH groups just underneath the surface; *C*, OH on a small radii particle; and *D*, on a larger radii particle (from reference [35]).

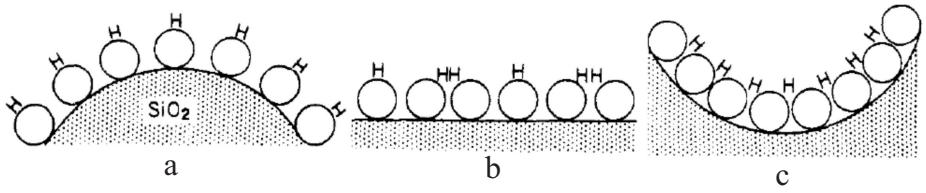

Figure 2-9: Representation of the effect of silica surface curvature. a) small "positive ", b) large radius of curvature, c) small negative radius of curvature (from reference [35]).

2.4 Conclusions

Defects have a great influence on the chemical stability of silica, damaging their mechanical strength and its transmission characteristics by increasing the absorption at OH related wavelengths.

Slight changes in the fabrication process (e.g. drawing temperature, drawing tension or drawing speed) or fabrication conditions (e.g. relative humidity, room temperature or processing time) of optical fibres including PCF's modify the structural relaxation of silica, consequently affecting the solubility and diffusion of water in the silica network.

The effects on the spectral absorption of OH groups in silica depend on the configuration of such groups and their concentration.

Chapter 3

Fabrication and loss mechanisms of photonic crystal fibres

Optical fibre performance has improved since the first "modern" fibres were fabricated [71]. In particular a lot of effort has been put towards the reduction of losses, including the reduction of Rayleigh scattering and OH content. This has led to the current state of the art of ultra low loss fibre fabrication [1, 72]. Photonic crystal fibre fabrication techniques have also evolved. The *stack and draw* technique, used to obtain the fibres investigated in this work, is the most common method used to fabricate PCF's and is described in this chapter. The different intrinsic and extrinsic loss mechanisms in optical fibres are also introduced in this chapter.

3.1 Introduction

Conventional optical fibres are dielectric optical waveguides that conduct light by total internal reflection (TIR) which occurs at the interface between the core and cladding. The core to which light is confined is the region with higher refractive index (see Figure 3-1). In photonic crystal fibres [73–76] there are different guiding mechanisms which depend on the regular micro-structure around the core and on the core material. The layout of such microstructure radically changes the optical properties of the fibres. Although there are many types of PCF's, in general they can be classified as solid core and hollow core fibres.

Most solid core PCF's consist of one type of glass. Frequently the cladding is formed by a periodic array of air holes that may form a two-dimensional photonic crystal. The parameters used to describe the cladding structure are d and Λ, which correspond to the hole diameter

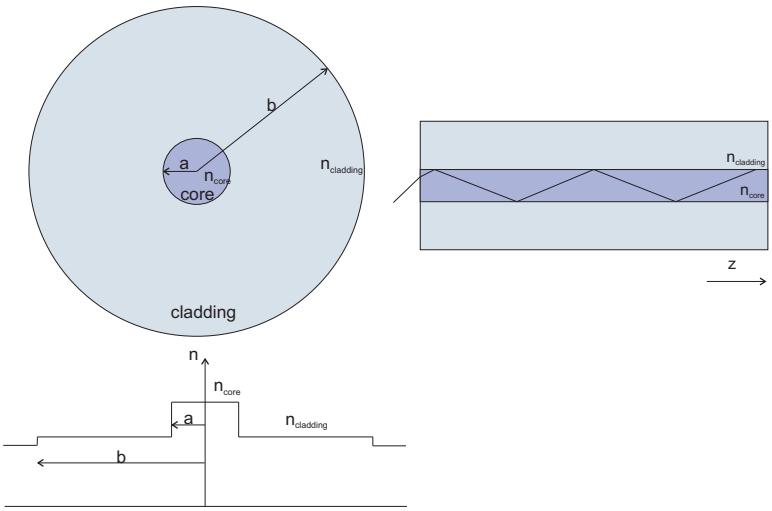

Figure 3-1: Illustration of a step-index fibre and refractive index profile. On the right is a representation of the TIR guiding mechanism.

and the pitch respectively, and are illustrated in Figure 3-2. As in conventional step-index fibres, in solid-core PCF's the light is guided at the core-cladding interface by *(modified) total internal reflection*. The "effective" refractive index of the cladding n_{eff} formed by air and glass is lower than that of the solid pure silica core. A qualitative description of the effective refractive index was proposed by Birks et al. [77].

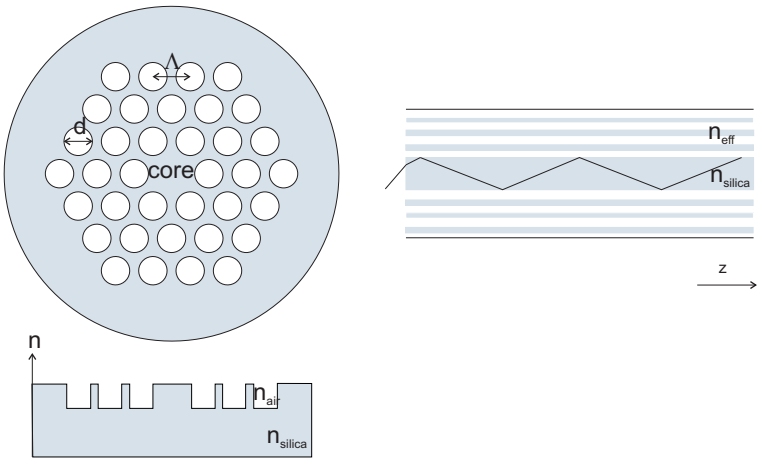

Figure 3-2: Illustration of a solid core PCF and refractive index profile. The pitch Λ, and the hole diameter d are the parameters that characterise the geometry and guiding properties of the fibre. On the right is an illustration of the modified TIR guiding mechanism.

In hollow core PCF's the guiding mechanism exploits the photonic bandgap effect [78, 79]. In this mechanism light travels in a defect (core) of a two-dimensional photonic crystal structure (cladding). The design of the cladding defines the range of wavelengths that can not propagate through the cladding, so that the light at those wavelengths can only propagate in the air core even though the refractive index of the air is lower than that of the cladding.

3.2 Photonic crystal fibres fabrication

Usually fabrication of PCF's is divided into two stages: preform fabrication and fibre drawing. There are several preform fabrication techniques like extrusion [80], preform drilling [81], sol-gel casting [82] and the stack and draw technique [73].

The preform construction in the *stack and draw technique* consists of building up a stack of silica glass capillaries and solid rods of ∼1 mm in diameter, usually in a pattern which resembles a honey comb. The stack is placed inside a silica tube of ∼ 20 mm of diameter whose dimensions vary according to the design. The inner and outer diameter of the capillaries determine the amount of glass in the cladding of the fibre as well as the pitch Λ and hole diameter d illustrated in Figure 3-2. Commonly the ratio d/Λ is used to refer to the air filling fraction in the cladding of the PCF. The jacketed stack is usually drawn down into canes of a few millimetres in diameter and 1 m long. To obtain an acceptable fibre diameter the cane is jacketed into a thick tube. The cross section diameter of the preform, illustrated in Figure 3-3 is of ∼1 cm and usually 1 m long, the jacketed cane constitutes the preform.

The first step of the process to draw fibre, canes or preform material (capillaries and rods) is very similar. The preform (stack, tube or rod) is fed into the furnace of a drawing tower as illustrated in Figure 3-4 and held from the top by the feed unit, whilst the bottom end is kept inside the furnace at ∼2000°C. At this temperature after a few minutes the glass softens and forms a glob that drops, this part of the processes is known as the "drop off ". In this region the preform (tube, rod or stack) diameter reduces to the fibre (capillary, rod or cane) diameter and it is known as the neck-down region. The canes, capillaries or rods are pulled by the tractor system and then collected afterwards whilst the feed unit is set to a speed commonly around 5 mm/min. The fibre is drawn by the winding system and collected. The thickness is controlled by changing the feed and draw speed. By changing the furnace temperature the fibre drawing tension is controlled and typical values are around ∼1980°C.

From the top a pressure line is connected to the preform, as shown in Figure 3-4 to inflate the hole size by increasing the pressure. To collapse the interstitial spaces left between capillaries a vacuum line is connected also from the top of the preform. When the preform is drawn into fibre the whole structure is scaled down to dimensions that vary according to

the design, with a standard fibre outer diameter being 125 μm.

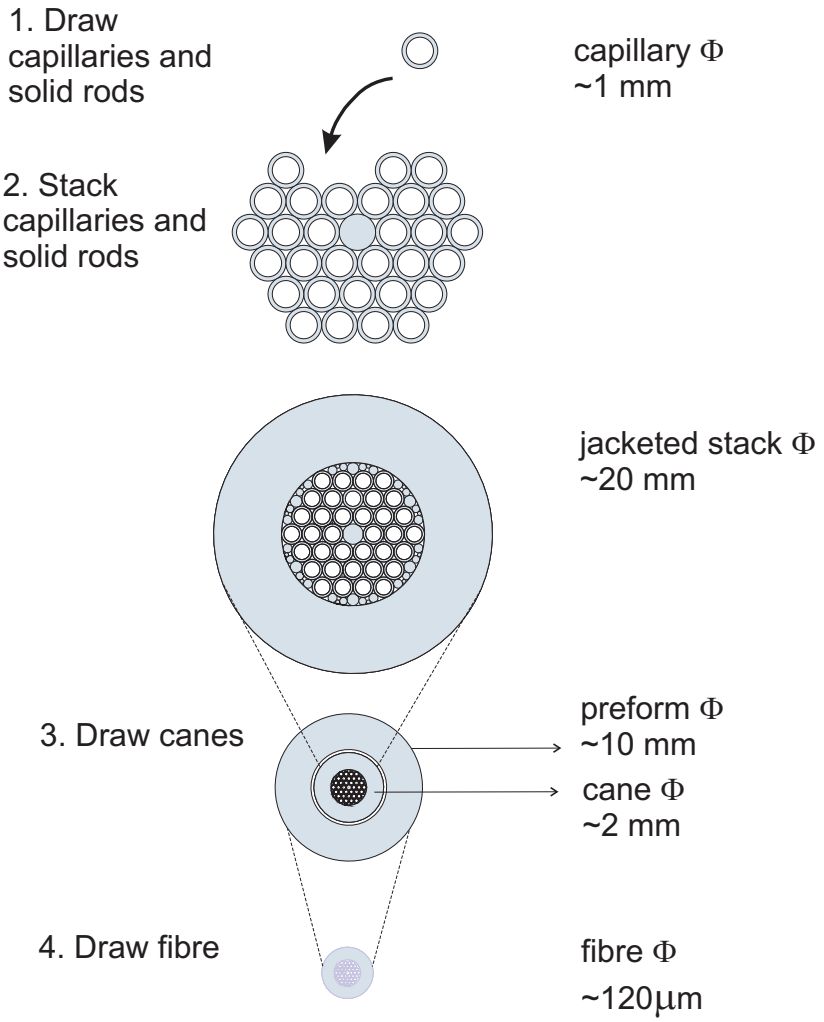

Figure 3-3: Representation of the stack and draw PCF fabrication process.

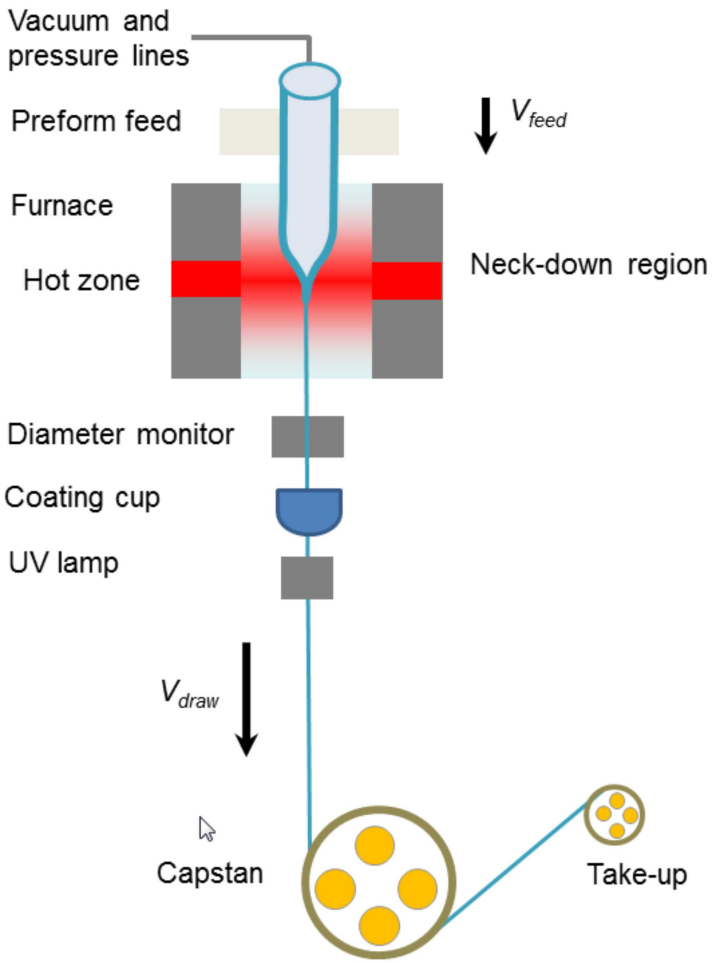

Figure 3-4: Schematic representation of a drawing tower.

3.3 Loss mechanisms in photonic crystal fibres

Loss in optical fibres is the exponential decay of the power carried by the guided modes along the fibre length described in equation 3.1 in terms of the input and output powers P_{in} and $P_{out_{(j)}}$ over a fixed length l of fibre:

$$P_{out_{(j)}} = P_{in} e^{-\alpha_{(j)} l} \tag{3.1}$$

where α_j is the power attenuation coefficient and j is the modal index and takes into account the geometry of the fibre and the spacial distribution of the *j-th* mode.

Losses in optical fibres are usually classified into two mechanisms, those related to ab-

sorption and those related to scattering [83]. The sum of these effects are also known as attenuation.

Absorption is an inelastic process and in silica optical fibres consists of the transformation of energy carried by the light (electromagnetic wave) into another form of energy like vibration of the molecules or electrons of the glass. It may be intrinsic to the silica glass, or due to impurities or to defects (colour centres) created during the fabrication process. Absorption due to electronic transitions is observed for wavelengths in the ultraviolet region, at these wavelengths photons carry enough energy to excite bound electrons to higher energy levels. The molecular vibrational frequency of the glass starts dominating for wavelengths >1600 nm.

Absorption in silica optical fibres is also determined by the quality and purity of the glass itself. In the early days of fibre fabrication, transition metals present in the glass fabrication process were also a source of absorption [83]. Nowadays one of the main sources of impurities and therefore of absorption in glass is OH. The wavelength range of the transparency window of silica is coincident with the first (see table 2.1), second, and third OH-stretching overtones located around 1380 nm, 950 nm and 725 nm respectively [84], hence the interest on reducing losses in optical fibres due to OH. During glass fabrication OH can diffuse from the preform tube during the MCVD (modified chemical vapour deposition) process. It can also form by reaction of the hydrogen contained in the starting materials or present in the gas used during the glass fabrication process. Another possible source of OH contamination is the reaction of water vapour present in the atmosphere with the silica surface and its subsequent diffusion into the bulk glass (as described in Chapter 2). Glass manufacturers nonetheless have developed new glass fabrication techniques that reduce the OH diffusion further [8]. Finally, another source of absorption is that caused by defects in silica glass also known as colour centres described in Chapter 2.

In fibres the dominant scattering effect is elastic scattering which occurs when the typical dimension of the glass fluctuations (e.g. inhomogeneities or bubbles) are smaller than the wavelength of the incident light, known as Rayleigh scattering. The Rayleigh scattering is proportional to λ^{-4} so that for shorter wavelengths the losses due to this mechanism will be greater. Other source of scattering are the waveguide imperfections due for example to capillary waves [85] and surface roughness in PCF's [85, 86]. Of these two, Rayleigh is the dominant scattering process for optical fibres. Other scattering processes are Raman and Brillouin [87–90] which are associated with non linear effects in fibres. In the wavelength range from ∼700 nm to ∼1600 nm, known as the *transparency window* of silica, the losses due to absorption (electronic and molecular) and scattering reach their lowest level, and is widely exploited in a myriad of applications.

In PCF's confinement and bending loss mechanisms are related to the fibre geometry

(i.e. cladding design and core diameter). The evanescent field of the guided mode extends to infinity and in principle it could only be completely confined to the core of a fibre with a cladding with infinite number of air holes. Although this is not possible, with an adequate cladding extent confinement losses can be reduced to negligible levels [91–93].

As in conventional fibres bending losses are also present in PCF's [94, 95]. Bending losses are observed when the radius of curvature of the coiled or bent fibre is less or equal than a critical bending radius which depends on the cladding design of the fibre. When the fibre is bent tightly the fundamental mode couples to higher-order modes that leak out of the fibre core. Bending losses in PCF's are closely related to the diameter of the holes around the core. Mode confinement can be achieved by increasing the air-hole to pitch ratio d/Λ [94]. If the wavelength λ of the fundamental guided mode is much smaller than Λ the mode will "spread" on to the neighbouring glass that forms the cladding and will finally escape. Improvements in PCF's bending losses have been reported by modifying the cladding holes configuration [96].

3.4 Loss measurements

According to equation 3.1, in order to calculate the attenuation it would be necessary to measure the power at the input of the fibre, which is not trivial. The cut-back technique illustrated in Figure 3-5 avoids this limitation by measuring the output power P_{in} for a length of fibre l_1, compared to the output power P_{out} measured over a shorter length l_2, maintaining the input power constant. Then using the expression in equation 3.1, one can calculate the loss over the remaining piece of fibre with the equation 3.2.

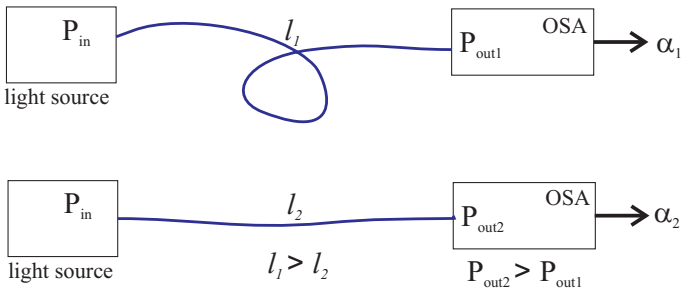

Figure 3-5: Illustration of the cutback technique to measure the attenuation in an optical fibre.

$$\alpha = \alpha_1 - \alpha_2 = -\frac{10}{(l_1 - l_2)} log_{10} \frac{P_{in}}{P_{out}} \tag{3.2}$$

where

$$\alpha_1 = -10(log_{10}\frac{P_{out1}}{P_{in}})/l_1 \quad \alpha_2 = -10(log_{10}\frac{P_{out2}}{P_{in}})/l_2 \tag{3.3}$$

α_1 and α_2 are the transmission measurements (losses) in dBm (the internal reference of the OSA is 1 mW) obtained from the OSA that correspond to the lengths l_1 and l_2 (commonly in km), P_{out1} and P_{out2} are the output powers in W for the lengths l_1 and l_2 respectively, and P_{in} is the input power from the light source in W.

Some of the disadvantages of the cut-back measurements are that it is a destructive technique, and that for l_1 and (or) $l_2 \lesssim 10$ m the power carried over by higher order modes that are present only for the first few meters of fibre, can bias the measurement in PCF's. For the same reason loss measurements in multimode fibres using this method are not accurate. Another limitation of this technique is that it gives an average estimate of the attenuation of the fibre and assumes that the attenuation is constant throughout the fibre. An example of non homogeneous attenuation in fibres is presented in Chapter 5, where the attenuation of the contaminated ends of the fibres investigated have higher local attenuation than that of uncontaminated middle section fibre.

Lateral scattering is a technique which detects the scattered power at two different points of the fibre obtaining the fibre loss in a similar way to the cutback technique. The optical time domain reflectometer technique (OTDR), insertion loss and joint loss are alternative non destructive loss measurement techniques [97] used in telecommunication systems .

3.5 Conclusions

Along with the characterisation of other aspects of optical fibres, the analysis of attenuation contributes to the understanding of the physics underlying these waveguides. A lot of knowledge has also been gained regarding the properties of the materials used for fibre fabrication, in particular for silica glass, and the effects on the fibre's transmission of the fabrication parameters like temperature and tension used during the fibre draw. By understanding the nature of loss mechanisms in silica PCF's new materials and fabrication processes can be engineered to reduce the attenuation in fibre. The interest in reducing losses has been in great extent motivated by industry but also by the the scientific interest in amorphous solids properties where silica is often used as a model because of its characteristics and simple structure.

Chapter 4

Low OH silica glass photonic crystal fibres

In this chapter three different fabrication methods to reduce the effects of OH contamination on the spectral attenuation of solid-core photonic crystal fibres, in particular at 1383 nm, are investigated and observed. In order to consistently obtain PCF's with low OH content, a tight control over the process and parameters used during fabrication is required. Repeatability in fabrication has allowed us to observe the relationship between the fibre spectral characteristics and the fabrication conditions. To achieve low OH PCF's the author has implemented some modifications to the standard PCF fabrication process. For the first method a protecting atmosphere was proposed to protect the silica glass from atmospheric moisture throughout the fabrication process. The second consisted of reducing the fabrication processing time. The third method consisted of annealing, prior to the fibre draw, a preform already contaminated by OH. This third method gave the lowest spectral attenuation reported to date for a 2 μm core diameter SC-PCF fabricated with commercially available glass. The OH concentration achieved with this method is close to that which is intrinsic to the starting material. This third method is the most effective fabrication method to consistently obtain low OH PCF including small-core PCF's ($<$2 μm). The strong relationship between the OH absorption peak at 1383 nm and core size for a range of fibres with different core diameters was investigated including cores below 2 μm. The rapid growth of the absorption at the first OH stretching overtone (1383 nm) observed for such core diameters was studied and was compared to numerical results.

4.1 Advances in low loss optical fibres

With the advent of data transmission systems based on conventional optical fibres back in the 1960's [98], the idea of reducing the losses in optical fibres arose so that such optical waveguides could be used as part of a practical communication medium [99]. Initially the goal was to reduce the attenuation to 20 dB/km by minimizing impurities in the material. The production of high purity glass at the Corning Glass Works had already led to low loss fibres by doping the core with germanium dioxide and using the chemical vapour deposition (CVD) method [100]. Bell laboratories developed the modified CVD (MCVD) in 1974 and managed to lower the attenuation at 1.06 μm to 3 dB/km [101]. In 1976 Nippon Telegraph and Telephone Public Corporation (now NTT) and Fujikura Cable Works reduced the attenuation further by reducing the OH losses, achieving an attenuation of 0.47 dB/km at 1.2 μm [102]. Later in 1979, by reducing the geometric imperfections in a Ge-doped preform the loss was 0.2 dB/km at 1550 nm [103].

The attenuation improvements in optical fibres continued motivated by telecommunications in order to increase the capacity of data transmissions, thereof the importance of reducing the absorption of the first OH-stretching overtone to maximize the operational bandwidth, resulting in a lower number of costly systems used to amplify the attenuated signal in undersea optical fibres. This would increase the data transport capacity in optical fibres and allowed their use in new laser applications. The attenuation reported in 2000 by Thomas et al. [104] in the range from 1260 nm to 1625 nm was already very close to the so-called clarity limit (of 0.276 dB/km at 1383 nm and 0.187 dB/km at 1550 nm), in other words very close to the lowest possible attenuation in silica glass fibres limited by two intrinsic physical mechanisms: at short wavelengths the Rayleigh scattering and at longer wavelengths silica molecular absorption. Later at OFS laboratories, hydrogen ageing effects that caused the OH to increase in Ge doped fibres were investigated; hydrogen present around the fibres and silica defects (NBOHC and E' centres) react to form the hydroxyls [2]. The ageing effects were prevented by controlling the fabrication process and materials which reduced defect centres, counteracting the ageing in fibres by applying a D_2 treatment (to shift the OH absorption at 1383 nm to the OD absorption at longer wavelengths out of the telecommunications window) and preventing the glass from alkali contamination [105, 106]. Such Ge doped ultra-low attenuation ageing-resistant fibres have been commercially available since 2007. To reduce further the attenuation in optical fibres it is necessary to reduce the Rayleigh scattering [107], which was the first approach by Sumitomo Ltd. In 1986 they achieved 0.154 dB/km at 1570 nm [108], for a pure silica core fibre (PSCF) and by 2002 this was reduced to 0.1484 dB/km at the same wavelength [72]. More recently, work has been done to achieve a "water-free" PSCF with fluorine-doped cladding, reported by Yamamoto

et al. in 2004 [1] with 0.247 dB/km and 0.170 dB/km at 1383 nm and 1550 nm respectively.

In SC-PCF's, low OH content has become relevant for fibres whose optical performance is related to 1383 nm absorption band (or OH overtones) such as supercontinuum generation (SC) [109–114], soliton self-frequency shift (SSFS) [115], and parametric conversion processes [116] and their applications. HC-PCF's for instance are currently being considered as a potential option for long-haul telecommunications to increase the network data transmission capacity, field in which recent progress has been reported [117].

Soon after the fabrication of the first SC-PCF, the first demonstration of low loss arrived by Tajima et al. in 2002 [118] reporting 0.8 dB/km at 1383 nm and 0.28dB/km at 1550 nm for core diameter of $\sim$12 μm using vapour axial deposition (VAD) to fabricate the glass, and a dehydration process along with dry conditions during the fibre draw. In 2007 the same group reported 0.4 dB/km at 1383 nm and 0.18 dB/km at 1550 nm by reducing the surface imperfection [119]. Although very low attenuation values are reported the fabrication method is not described in detail and the diameters of the core are not clearly specified. In 2006 an attenuation of 38 dB/km at 1383 nm and 6.9 dB/km 1550 nm was reported for a 2.5 μm core diameter SC-PCF by Monteville et al. [120], achieved by chemically cleaning the tubes and polishing them finely to reduce OH and general losses. Current commercially available low-loss SC-PCF of 4.8 μm core diameter hold an attenuation <15 dB/km at 1383 nm (including background absorption) and <2.5 dB/km at 1550 nm and for a 1.8 μm core diameter <140 dB/km at 1383 nm [121] (including background absorption).

A lot of research on silica glass properties and fabrication techniques has been done by various research groups around the globe since the first optical fibre and still continues today. The aim of the work presented in this chapter is to contribute to that work by making available the findings regarding the fabrication process to obtain consistently low loss SC-PCF's by reducing OH final content including for core diameters <2 μm.

4.2 Design and fabrication parameters of low OH and low loss photonic crystal fibres

The preforms to fabricate the fibres analysed in this thesis were fabricated with the *stack and draw* technique [73] described in Chapter 3. The capillaries and rods, to build the stack, as well as the canes and fibres were drawn using a *Heathway* optical fibre drawing tower with a graphite heating furnace. The spectral transmission was measured in the range of 400 nm to 1750 nm using a halogen lamp as a white light source and an optical spectrum analyser (OSA) to record the spectral transmission. The attenuation of the fibres was characterized using the cut back technique, performing a transmission measurement first over a long piece of fibre,

cutting the fibre and subsequently measuring again the transmission over the remainder piece, keeping the same end of the fibre coupled to the light source as described in section 3.4. For the 5 μm core fibres the initial length l_1=300 m and the final length l_2=50 m, for the 2 μm core fibres l_1=200 m and the l_2= 50 m and for fibres with core diameters <2 μm l_1=150 m and the l_2= 50 m. Transmission measurements were carried out three times for each length, every time cleaving half a centimetre off the end coupled to the OSA. Transmission data were averaged afterwards in order to obtain the fibre attenuation. The attenuation α in dB/km was calculated according to the equation 3.2 derived from equation 3.1. The uncertainty of the attenuation obtained for fibres with 5 μm, 2 μm and <2 μm is respectively $\pm$ 2.3 dB/km, $\pm$2.4 dB/km and $\pm$2.6 dB/km.

Every effort was made to maintain all the conditions the same during the fabrication of identical fibres, nonetheless there are differences in their spectral absorption that can be attributed to a number of factors including different humidity conditions, differences in the initial OH content of the starting material (as the core rods were originated from different starting rods as well as the capillaries derived from different tubes which might have different contents of OH), and even the changes in the furnace behaviour after replacing graphite element or the muffle tube.

As discussed in section 4.5.3 in some cases the difference in absorption levels observed at 1383 nm for fibres with the same core diameter is larger than the uncertainty as seen in Figure 4-14. In principle if the fabrication conditions and materials are identical one would expect a larger absorption at 1383 nm for a fibre with smaller core diameter than that observed for a larger core. The notorious difference particularly at the first OH overtone of the attenuation curves of a 2μm core fibre in Figure 4-14 (annealed preform) and the 2.3 μm core fibre in Figure 6-4 is probably due to difference in starting material OH content and certainly due to a difference in the fabrication conditions.

One of the main issues in PCF fabrication is the repeatability, especially of low loss fibres, hence the aim is to tightly control the whole fabrication process by recording and describing in detail the steps followed, including feed speed, draw speed, tension and pressure. Relative humidity (RH%) was monitored during the fabrication process for most of the fibres. The drawing parameters used to obtain the 5 μm core diameter fibres are presented in table 4.1.

feed speed (mm/min)	draw speed (m/min)	tension(g)	pressure (kPa)
5	32	190	10

Table 4.1: **Fibre drawing parameters to obtain 5 μm core diamteter SC-PCF's.**

The design of the PCF's used in the experiments to reduce OH content consists of a central rod surrounded by one ring of six capillaries stacked in a jacketing tube with an

inner diameter of 4.3 mm and an outer diameter of 10 mm shown in Figure 4-1(a). The preform is drawn into 3 mm canes (Figure 4-1(b)), and to obtain the fibre a cane is jacketed in a tube with 3.2 mm and 10 mm inner and outer diameter respectively. The diameter of the fibre and fibre core using this geometry are 125 μm and 5 μm respectively, in Figure 4-1(c) is the SEM picture of a one-ring fibre. The simple design allowed rapid fabrication, facilitating repeatability of the fibres.

To study the attenuation at 1383 nm in small-core diameter SC-PCF's from 2 μm down to 1.2 μm, a different geometry that allowed us to scale down the core diameter was implemented, while maintaining an acceptable fibre outer diameter as presented in Figure 4-2(b). The design consisted of three rings of air holes and a jacketing tube with dimensions of 15 mm and 9.2 mm corresponding to outer and inner diameter. The stack was drawn into 2 mm canes, and jacketed in a 10 mm $\times$ 2.1 mm tube for the fibre draw. Figures 4-2(a), (b) and (c) show the respective SEM pictures for a cane, a fibre and the cladding region of a fibre fabricated with this design.

The material used to fabricate the one-ring-structure fibres was synthetic silica glass Suprasil F300 from Heraeus [8] (for both core rod and capillaries) and for the 3 ring structure fibre Suprasil F500 was used for rods and capillaries. Both glasses only differ in the OH content with typical concentrations of 0.2 ppm and 0.02 ppm respectively, the exact OH concentration of the raw material is not known. No additional chemical drying treatment (i.e. halogen-based processing) was performed to the glass. A few fibres with three ring structure were fabricated using F300 glass for capillaries (spectra not shown herein). With the idea to reduce the attenuation further a clear option was to use F500 glass. One would expect an improvement in the OH content of the fibres fabricated with F500 glass according to the specified OH content of the glass. Although there was no obvious reduction in the OH content of such fibres compared to the fibres fabricated with F300, F500 glass was preferred for the fabrication for small core fibres ($<2\mu$m) as it was already available.

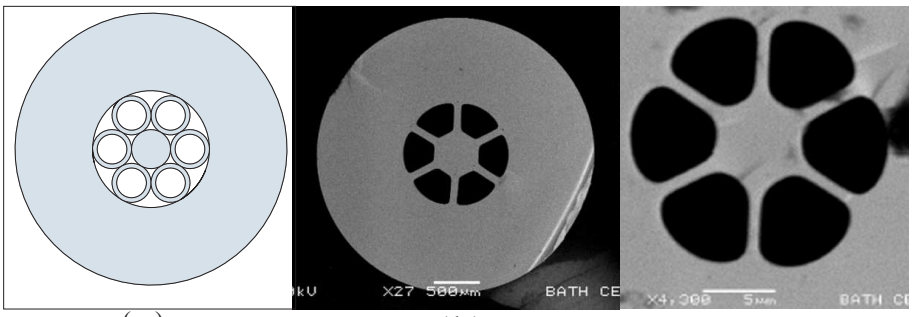

(a) (b) (c)

Figure 4-1: (a) Representation of a stack of 1 ring of capillaries surrounding a solid silica rod core. (b) SEM picture of 3 mm cane used to obtain low OH PCF's. (c) SEM picture of the core and cladding region of a 5 μm core diameter fibre.

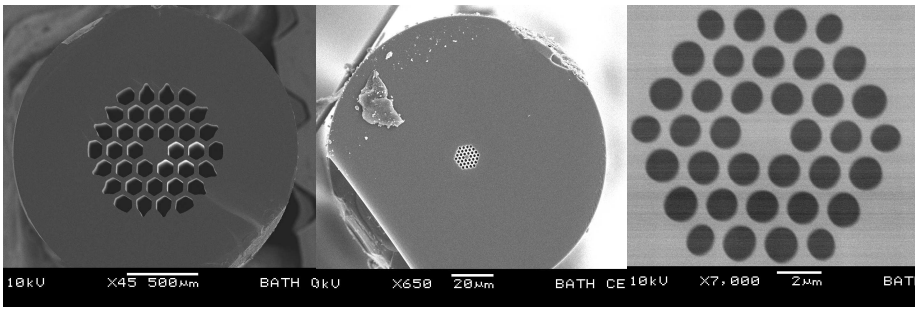

(a) (b) (c)

Figure 4-2: SEM pictures of (a) a 2 mm cane with 3 ring structure, (b) a 2 μm core diameter PCF and (c) the core and cladding region of a 2 μm core diameter fibre.

4.3 Low OH and low loss photonic crystal fibres fabricated within a protecting atmosphere

4.3.1 Fabrication process description

The fibres were fabricated in a temperature controlled clean room in which the humidity conditions oscillate during the year according to the weather, increasing particularly in summer and decreasing in winter. Hence the objective of this experiment was to reduce as much as possible the contact of the drawn material (i.e. capillaries, rods, stacks and canes) with the moisture in the air by using a protecting inert atmosphere (N_2) during and after fabrication in order to reduce the final OH content in the fibre.

During the draw a set of in-house fabricated modules shown in Figure 4-3, continuously purged with N_2 to protect the glass from moisture during the draw, were attached to the drawing tower structure. The first module was placed just below the furnace and above the diameter laser control, the second between the laser control and the cane pulling belts and the third was below the pulling belts, so that the modules protected the material just before collection.

The detailed description of the fibre fabrication process using a protecting atmosphere is described below.

Preparation

Preparation consisted of the following steps:

1. Place the jacketing tube for the stack inside a new plastic bag or plastic tube previously adapted to connect a nitrogen line from one end, leaving the opposite end open (to insert the capillaries later on).
2. Connect the bag to N_2 flow making sure that there is flow inside the jacketing tube to guarantee a protecting atmosphere for the capillaries that will be stacked inside.
3. Place the jacketing tube inside the bag horizontally on a support or stacking rig.
4. Attach the protecting modules to the tower as shown in Figure 4-3.
5. Start N_2 flow to purge the modules. Keep N_2 flowing during capillaries, rod, and canes draw.
6. Start up the drawing tower as usual.

7. Wipe the tube and the solid rod with a clean dry cloth just before starting the draw (no isopropyl alcohol was used). To reduce the possibilities of OH contamination the tubes were not washed.

Capillary and rod draw process

The process for drawing the capillaries is identical to the standard process except for the N_2 flow in the protecting modules during fabrication. The silica tube or solid rod is clamped to the preform feed unit at the top of the drawing tower before the draw.

Stacking and preform preparation

The design comprising only one ring of air holes and a central rod facilitates stacking directly into the jacketing tube, as opposed to two steps needed to stack a larger structure. The capillaries naturally fit forming a hexagonal ring around the core, eliminating the use of the stacking rig for this design. The use of a stacking rig, although possible, would make the protecting atmosphere more complex to control. Stacking and jacketing are integrated in one step.

A total of seven capillaries form the initial structure before the central rod is drawn as shown in Figure 4-4. The central rod is drawn following the same steps as for the capillary draw. The central capillary is replaced with the rod by carefully pulling it out from the end connected to the N_2 flow (opening a small hole on the plastic bag and sealing it with tape afterwards) and simultaneously pushing in the freshly drawn rod from the opposite end.

Cane draw

Whilst being constantly purged with N_2 the jacketed stack is prepared to draw the canes by holding the capillaries with PTFE tape (Teflon tape) and sealing the interstitial spaces between them with epoxy glue at one end. Once the stack is prepared it is transported within the protecting bag to the preform feed unit of the tower to clamp it and start the draw to obtain the canes. During the draw the stack structure is also continuously purged from the top end with N_2. The canes were cut to 1.1 m length and kept inside a clean plastic tube, also purged using N_2.

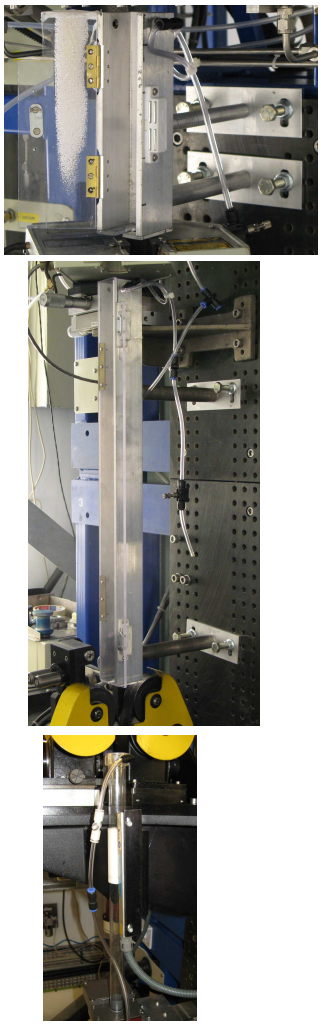

Figure 4-3: Pictures of the protecting modules attached to the tower connected to nitrogen flow, one just below the furnace and above the diameter laser control (top), the second one between the laser control and the tractor belts (middle) , c) (bottom) the third one was placed below the pulling bands.

Fibre draw

Finally to draw the fibre, a cane is placed inside a thick-walled F300 tube (also purged with N_2) to obtain a fibre with acceptable dimensions. The preform is clamped to the preform feed unit at the top of the tower and purged with N_2 prior to the drop off. During the fibre draw no N_2 flow was used in the protecting modules. The vacuum used to collapsed the jacket on top of the cane was -10 kPa and the pressure used to pressurize the cladding holes was 20 kPa.

Whilst protecting the drawn material with an inert atmosphere (N_2) to minimize OH presence during fabrication was the initial idea, the design also allowed a fast fabrication process. In particular to collect and stack in the same step of the process reduces the fabrication time considerably. Rapid processing was observed to be an important variable for obtaining low OH PCF's, and led to a second fabrication method described in section 4.4.

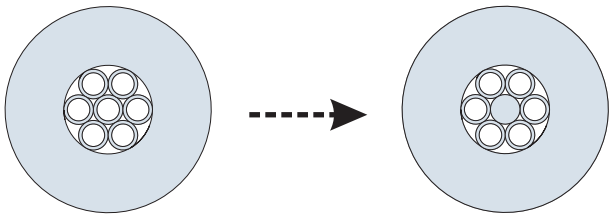

Figure 4-4: 1 ring stack preparation: first step 7 capillaries are stacked (left) then the central capillary is replaced by a solid rod (right).

4.3.2 Atmospheric control PCF fabrication experiments

Using the protecting atmosphere fabrication method several experiments were performed and are summarised in Figures 4-5 and 4-6.

All N_2 SC-PCF fabrication

As part of a preliminary atmospheric control process the raw material was protected by keeping it in a bag filled with N_2 prior to drawing. After some experiments it was observed that the spectral attenuation was not affected when the raw silica tubes and rods were exposed to the laboratory environment, or at least it was not possible to detect changes in the measured transmission. One can expect that once the raw material is drawn into capillaries, rods and canes it is more prone to OH contamination (because of the abrupt change of glass temperature and thermal memory related, effects i.e. T_f, [6, 41, 59–61]) and its exposure to the draw environment leads to an increase of OH content in the final fibre.

4.3. Low OH and low loss photonic crystal fibres fabricated within a protecting atmosphere

Moisture was minimized during the fabrication of capillaries, rod and canes in modules by using N_2 and also purging the storing tubes with N_2. In Figure 4-5 the observed spectral attenuation is compared for three different fibres with a 5 μm core diameter. Two of them were derived from identical canes obtained under the protecting atmosphere, both stored for one week, one in a N_2 atmosphere and the other stored open to air. Both spectra were compared with that obtained from a control fibre fabricated with the standard process (i.e. no N_2 used during drawn). The cane used to fabricate the control fibre was also exposed for 1 week to atmospheric conditions prior to the fibre draw.

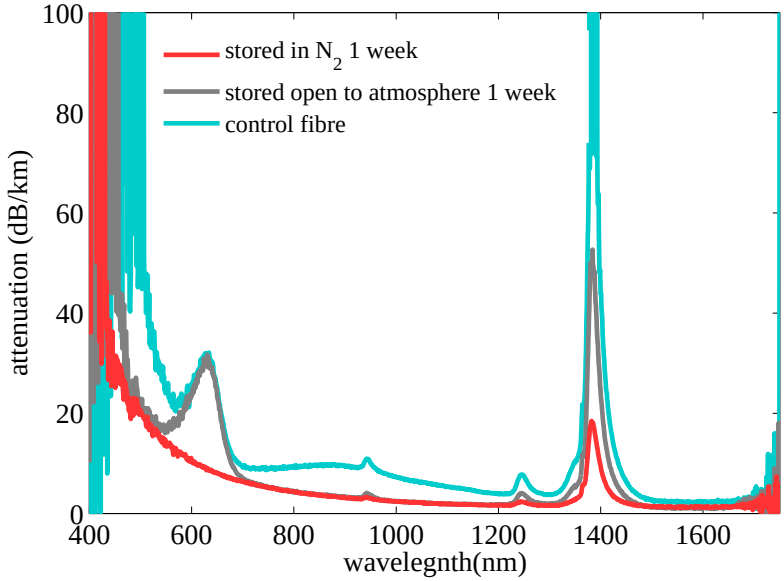

Figure 4-5: Effects on fibre attenuation using the protecting atmosphere (i.e N_2) during fabrication. Attenuation of fibres fabricated from canes stored for one week in a tube purged using nitrogen flow (red) and stored open to air (grey) compared to the control fibre fabricated with no protecting atmosphere also stored open to atmosphere (blue).

For this experiment the lowest attenuation corresponds to the fibre fabricated and stored under a protective N_2 atmosphere with an absorption of 16 dB/km at 1383 nm. The attenuation of the fibre stored open to atmosphere at 1383 nm was 52 dB/km, the combination overtone at 1250 nm and the second OH overtone at 950 nm also increased, and the feature related to a defect centre known as NBOHC (non-bridging oxygen hole centres) at 630 nm [16, 27, 33] started to appear. The control fibre attenuation curve also shows the 630 nm absorption peak, an absorption at 1383 nm of more than 100 dB/km, and an increase of attenuation at shorter wavelengths along with a feature altering the attenuation in the region between 700 nm and 1200 nm.

Effects on SC-PCF attenuation of stack and canes storing conditions

The attenuation curves presented in Figure 4-6 correspond to two different fibres both fabricated from canes that were drawn using the standard process (no N_2 flow used during fabrication of rods, capillaries and canes). One of the canes was stored for 3 hours in a tube filled with N_2, and the other was left open to air during 1.5 hours. An OH absorption at 1383 nm of 8 dB/km, the lowest observed for a 5 μm core SC-PCF at this wavelength, corresponds to the fibre made from the cane stored in N_2 atmosphere. The different spectral features observed for the fibre made from the cane exposed to atmosphere are a higher absorption at 1383 nm (15 dB/km) and a slight decrease on the general attenuation. A higher attenuation is expected for the unprotected preform as observed with 15 dB/km that correspond to a concentration of 0.26 ppm of OH (according to Humbach et al. [84]) in contrast to 8 dB/km equivalent to 0.13 ppm for the protected preform. The results of this experiment show the importance of a dry processing and storing environment and clearly illustrates the rapid degradation at 1383 nm in the preform exposed for only 1.5 hours. Besides the effects of the conditions during fabrication and storage on the spectral attenuation of SC-PCF's, another important effect was that of time. Comparing the spectral attenuation from Figs. 4-5 and 4-6 of fibres derived from canes exposed to atmosphere 1 week and 1.5 hours an increase in the attenuation at 1383 nm is observed for a larger processing time. The effect of processing time on SC-PCF's attenuation is explored and discussed in section 4.4.

Atmospheric water present in the fabrication environment reacts with silica glass creating OH [38] which increases the final concentration of OH groups in the fibres. OH and broken strained Si−O links are both known to be precursors of defects like the 630 nm absorption peak (NBOHC) [16, 31, 32]. For the 5 μm core diameter fibres the 630 nm peak only appears when the absorption at 1383 nm reaches values above 22 dB/km equivalent to 0.36 ppm (see for example Figure 4-10). During fabrication silica glass changes its configuration and rearranges [41] creating strains and defects in the material [27, 36], where water vapour can dissociate and the OH can attach to the silica network [38]. This effect depends on the fictive temperature (T_f) [6, 41, 59–61].

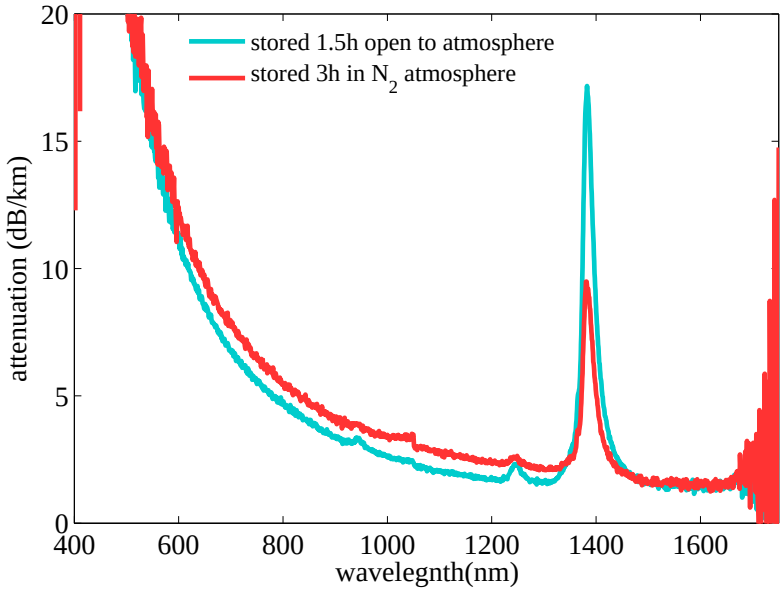

Figure 4-6: Attenuation of fibres from canes fabricated with standard process stored under different conditions. After fabrication cane was stored in N_2 during 3 hours before fibre draw (red curve) the other cane was exposed 90 minutes to atmospheric conditions (blue curve).

4.4 Low OH and low loss PCF by reducing processing time

4.4.1 Fabrication process description

The one ring simple design allowed a very rapid fabrication process which motivated this investigation into the effect of fabrication time on SC-PCF's attenuation. Typically the total time required to fabricate a PCF from start to finish ranges from a couple of days up to a week for large structures. The time that the material is left exposed to water vapour present in the laboratory between one stage to the next depends on the design and on the availability of fabrication facilities. The stacking time required to build up structures comprising a large number of capillaries, for example a hollow-core bandgap fibre, is considerably longer than that needed to fabricate one ring cross-section (i.e. six capillaries and a central rod). A rough estimate for the total fabrication time for a PCF with 8 rings is one week; fabrication of capillaries and packing rods can take 1 or 2 days, stacking more than 240 capillaries will take 2 or 3 day, and finally 2 days for canes and fibre fabrication. The standard stacking process is done in a clean room where no other special precautions are taken to protect the drawn glass from OH contamination.

For this experiment the fabrication time was controlled during the multiple stages. The average time to fabricate a stack with 6 capillaries ring is less than one hour. The fabrication steps and drawing parameters were the same than those used in the atmospheric control method except that a protecting atmosphere was not implemented at all in order to observe the effects on spectral attenuation only due to processing times as shown in Figures 4-7, 4-8, and 4-9 with different exposure times of the canes to laboratory environment and Figure 4-10 obtained from stacks exposed different amounts of time.

The fabrication process presented in the following section was in fact motivated by the requirement to create cladding structures of more than one ring. An alternative fabrication method was necessary to reduce the unavoidable OH contamination whilst fabricating large stacks.

4.4.2 Time control SC-PCF fabrication experiments

For these experiments the focus was to build up the stacks and fabricate the canes in the shortest possible time with no special protection from atmospheric moisture and expose the canes different amounts of time to observe the attenuation dependence in particular at 1383 nm. The time to fabricate each stack and corresponding canes used in this experiments was approximately 2 hours.

Effect of fabrication delays on PCF attenuation

Two identical canes were exposed to air different amounts of time, 90 minutes and 8 days. Figure 4-7 shows the attenuation measured for the 5 μm core diameter fibres obtained. The lowest attenuation corresponds to the fibre fabricated with the shortest delay, whereas the feature at 630 nm and an attenuation of 56 dB/km at 1383 nm is observed in the fibre derived from the preform exposed 8 days. Consistently with the observations made in section 4.3.2 the 630 nm absorption band is observed when the attenuation at 1383 nm is larger than 22 dB/km.

In Figure 4-8 the absorption centred at 1383 nm for 4 fibres fabricated with different delays, derived from the same stack and using the same fabrication process, is presented. One cane was stored for 90 minutes open to atmosphere, another cane was stored for 4 hours in a protective atmosphere before fabrication, while a third cane was stored for 1 week in N_2 before being exposed to air for 8 hours before the fibre draw. The fourth cane was left exposed to air for 8 days. For this second set of fibres the lowest attenuation corresponds to the fibre with fastest processing, the attenuation increased with delay in fabrication and consequently the highest attenuation is observed from the fibre obtained from the cane exposed the longest.

A comparison of the absorption of fibres derived from canes exposed to air 90 minutes, 18 hours and 7 days, and from a cane stored in nitrogen 3 hours is shown in Figure 4-9. Despite the fact that one of the canes was exposed to air for only 90 minutes, its attenuation at 1383 nm is higher than that for fibre derived from a cane stored in N_2 for 3 hours which highlights the importance of humidity conditions during fabrication. On the same figure, the 630 nm peak is not observable for fibres with OH absorption slightly less than 20 dB/km whereas for the other two fibres it is. A broad absorption feature observed around 900 nm seems to be related with higher levels of OH as well as with high attenuation at short wavelengths.

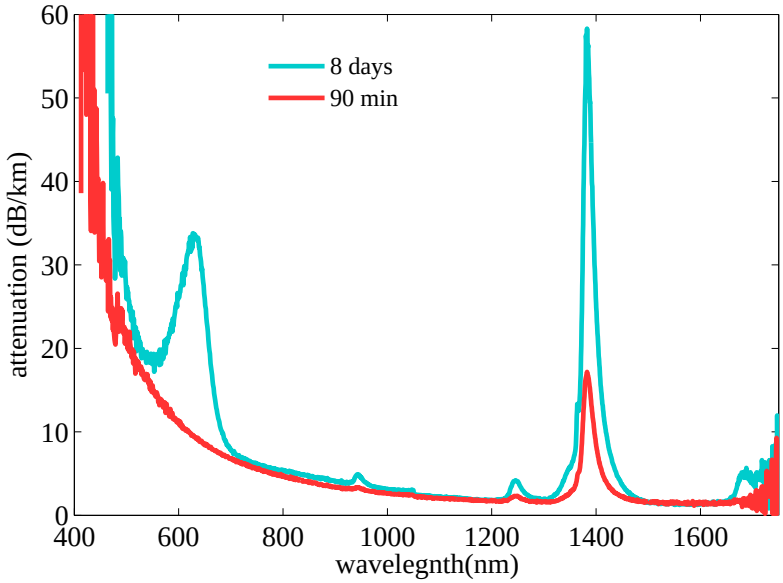

Figure 4-7: Time dependence attenuation of fibres obtained from canes stored open to air during different times, 90 minutes (red curve) and 8 days (blue curve).

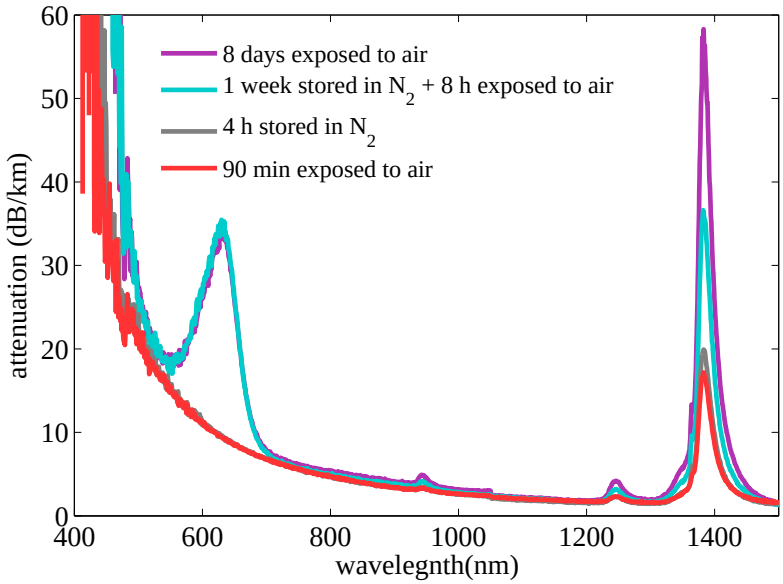

Figure 4-8: Time dependence attenuation at 1383 nm for of 5 μm core diameter PCF's obtained from canes exposed to air prior to fibre draw. Attenuation increases as the delay is longer. Attenuation spectra correspond from bottom to top to canes exposed: 1.5 hours to air, cane stored 4 hours in N_2 atmosphere, stored in nitrogen for 1 week and exposed to air 8 hours prior fibre draw and finally cane exposed 8 days to air.

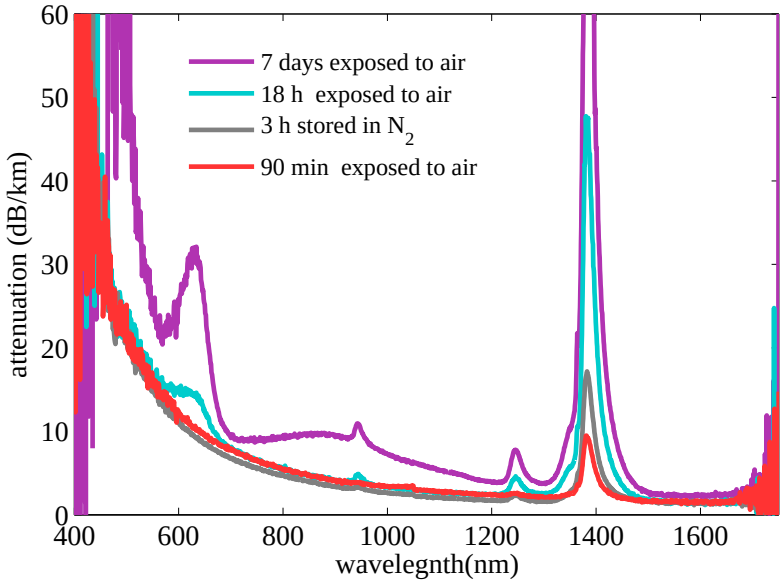

Figure 4-9: Time dependent attenuation of 5 μm core diameter PCF's at 1383 nm. Attenuation increases with the longest exposure time of the cane to air. From bottom to top 90 minutes, 3 hours, 18 hours and 7 days.

Susceptibility to OH contamination for distinct fabrication stages

In a separate experiment a stack was fabricated and exposed to atmospheric conditions (20°C and 30 RH%) for 16 days before being drawn into canes. The fibre was obtained immediately after the canes were drawn. A second fibre was drawn from a cane exposed for one week to air (20°C and 40 RH%) drawn just after building the stack.

In Figure 4-10 the attenuation curves for the fibres obtained are presented. The fibre derived from the stack exposed 16 days to air shows lower absorption at 1383 nm (25.8 dB/km) but higher at 630 nm compared to the fibre derived from a cane exposed 7 days. The higher absorption at 1383 nm of the latter fibre could be arguably attributed to higher humidity conditions during the draw, on the other hand, it was exposed less than half the time the stack was. It appears that defects where OH can form (during the material exposure to air) are more abundant on cane than on stack stage. The large 1383 nm absorption peak and the reduced absorption at 630 nm in the fibre derived from the exposed canes seems to be related to the growth of the broad absorption at 900 nm and to the shorter wavelength absorption increase. That dynamic is not present in the fibre derived from the exposed stack, so it seems that the number of defects and OH content are yet not enough to trigger the changes observed on the other fibre where the 630 nm is reduced but the other spectral features appear.

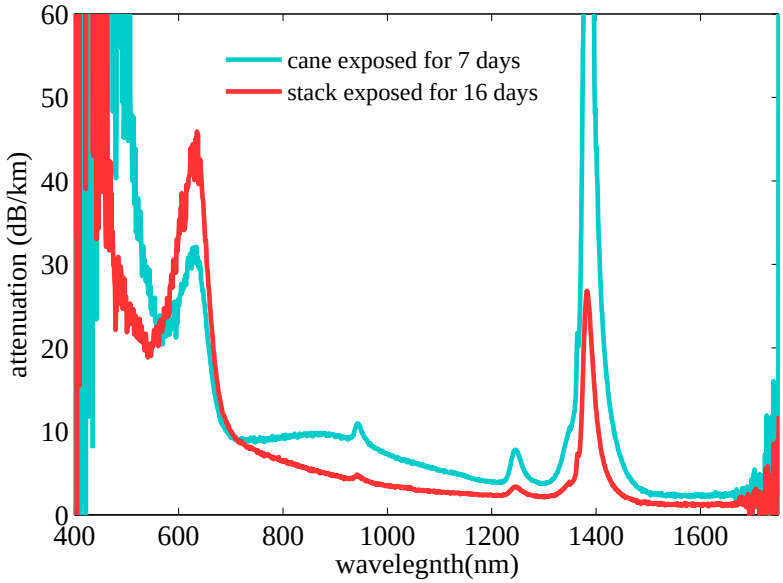

Figure 4-10: Attenuation for 5μm core PCF's, one derived from a stack exposed to air for 16 days (red curve) and other from a cane exposed for 1 week to air before fibre draw (blue curve).

Regarding the time control experiments, the lowest attenuation is obtained for the fastest fabrication turn-around, as seen consistently in Figures 4-7, 4-8 and 4-9. Only a few hours of exposure to the atmosphere cause there to be a dramatic increase in attenuation at the first stretching OH overtone in silica. The drawing induced peak appears at 630 nm if there is a delay in the fabrication process of more than a few hours, the increased absorption below 600 nm and the feature around 900 nm appear also to be related with the increased OH caused by the delayed fabrication [122].

The results obtained from the atmospheric control and time control experiments reveal that the final OH content depends on the fabrication laboratory conditions (RH%) and the delays in fabrication. From the attenuation presented in Figure 4-10 it was observed that the susceptibility to OH contamination depends also on which fabrication stage is exposed to atmosphere. Both the stack and cane have inherently different thermal histories and there is a difference in the diameter of the central rod in the cane and in the stack. The scaling factor, or draw down ratio (DDR) between the diameter of the original silica rod as purchased and the core diameter in the cane is 47, and for the core in the stack is 14. The core diameter in the cane is smaller than the core in the stack stage, and the more the core diameter is reduced the more strains and broken Si−O bonds are generated in the material [36] these are more abundant in the cane stage than in the stack which makes the core in

the cane more prone to OH formation.

4.5 Low OH and low loss PCF's obtained using annealing treatment

With the two previous methods, the attenuation for 5 μm core diameter fibres was successfully reduced, but for larger stacks (needed to obtain fibres with a core diameter of <2 μm) the implementation of those methods was not simple, hence the idea to reduce the OH contamination in SC-PCF's by annealing arose. For this method the atmospheric control method was used and added the annealing step just before the fibre draw.

The method was tested first with the one ring structure. For this one ring geometry the fabrication of the capillaries, rods and canes was done as previously described in the protecting atmosphere fabrication method. The annealing was carried out prior to drop off, the preform was passed through the furnace three times while being purged with nitrogen throughout. The preform was baked along 80 cm length. The temperature was set so that the pyrometer reading was 1880°C, while the feeding speed was 40 mm/min. Just before starting the drop off, N_2 flow is stopped to prevent the inflation of the structure. With such fabrication parameters it was expected to see changes in the spectral attenuation of fibres as a result of the annealing therefore temperature was chosen to be well above the annealing temperature of glass and the feed speed was set fast enough so that the structure and preform did not melt. These parameters were also a good balance between fabrication time (to allow repeated fabrication) and effectiveness to anneal the NBOHC defects eliminating the absorption at 630 nm absorption peak as well as reducing the attenuation at 1383 nm discussed further in this section.

4.5.1 Fabrication process description

1. Follow the preparation steps used in the atmospheric control fabrication process to draw the capillaries, central rods and canes.
2. Set the furnace temperature to 1880 °C.
3. Set feed speed to 40 mm/min for 5 μm core PCF (20 mm/min for 2 μm core PCF).
4. Load the preform into the furnace (15 cm).
5. Start the feeding.
6. Stop after baking 80 cm for 5 μm core PCF and 60cm for 2 μm core PCF.

7. Retract the preform to the original position in the furnace (15 cm).
8. Repeat 2 more times.
9. At the end of the third round stop the N_2 flow.
10. Increase the furnace temperature up to 2100°C.
11. Start the drop off and draw the fibre as normal.

    The feed speed of 40 mm/min was tested on the preforms to obtain core sizes in the range of diameter of 2 μm and smaller but the results were not satisfactory. The feed speed of 20 mm/min showed good results. As the preform is bigger and has more glass and air it needs longer baking time to get sufficiently hot in order to anneal the defects.

After proving the method several times with 5 μm core fibres the method was used to fabricate 2 μm core diameter fibre. To fabricate the stack with 3 rings as required for the 2 μm core fibres the standard *stack and draw* technique was used implying that the stacking process started only after all the capillaries and rods were collected. The central rod and six capillaries were kept in a tube with nitrogen flow until stacked. The stack was jacketed in a thick walled tube (25 mm × 13 mm) also enclosed in a bag with N_2 flow. The baking was carried out over 60 cm of the preform at 20 mm/min. The following day the preform was drawn into 2 mm canes that were stored in a plastic tube continuously purged with N_2 flow. The total fabrication taken time to build up the stack was 7 hours and the room conditions during the process were 20°C and 26 RH%.

4.5.2 Experiments using the annealing method

All the preforms used in these experiments were annealed as described previously in the annealing fabrication process.

Low OH 5 μm core diameter PCF by annealing preform

The annealing method was first performed to fabricate 5 μm core diameter fibres. Two identical canes from the stack exposed for 16 days were used to built the preforms used to obtain the control fibre and the fibre fabricated with the annealing process. In Figure 4-11 their spectral attenuation is shown. The lowest attenuation corresponds to the fibre derived from the annealed preform observing a reduced absorption at 1383 nm of 15 dB/km and the 630 nm is eliminated. When the preform is annealed the drawing induced defects and shear stresses in the core caused by the draw are relieved reducing the absorption at 630 nm and 1383 nm respectively, the number of defect points is reduced as a consequence of the

silica glass relaxation and therefore the OH formation and the subsequent absorption in final fibre is also reduced. In contrast, the fibre derived from the control preform (formed with the control cane), in its attenuation spectrum the absorption of the drawing induced defect (35 dB/km) is observed along with a larger absorption at 1383 nm of 25 dB/km.

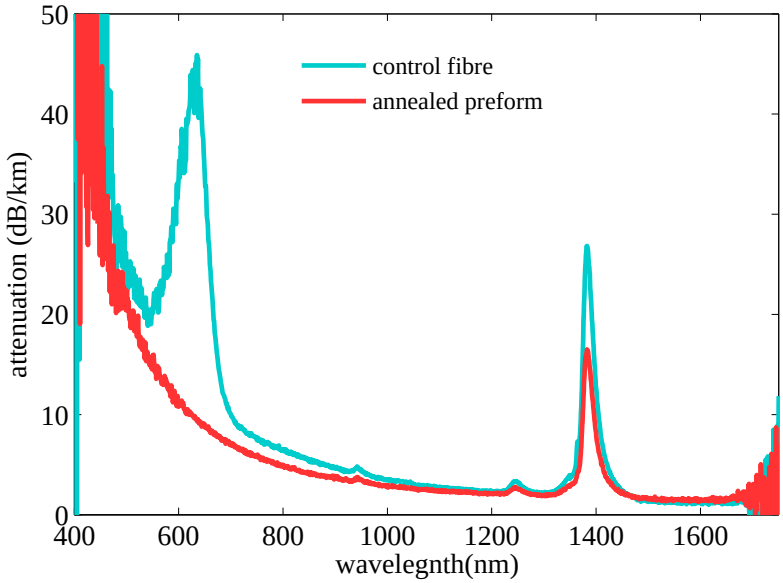

Figure 4-11: Spectral attenuation for 5 μm core PCF's, the blue curve corresponds to that of the control fibre fabricated with no special treatment to reduce OH content and the red curve to that of the fibre obtained after preform annealing.

Low OH 2 μm core diameter SC-PCF by annealing preform

For this experiment a stack with 3 rings of air holes was drawn into canes. The spectra shown in Figure 4-12 correspond to 2 μm core diameter SC-PCF drawn from two identical canes derived from the same stack. Again the lowest attenuation curve is that of fibre derived from a treated preform. In the spectrum of the control fibre (fabricated with no special treatment) a very high absorption is observed at 1383 nm of more than 100 dB/km, and it is also possible to observe the absorption peak at 630 nm (34 dB/km) and increased absorption for wavelengths 600 nm. An increased background absorption is expected as the core diameter of the fibre decreases because of the surface per unit of volume in small-core fibres is larger. Also a complex relaxation process of the silica glass network which involves fictive temperature T_f [36] affects the Rayleigh scattering [107], being that the higher T_f the lower the relaxation and consequently more absorption. The T_f for smaller core fibres is higher [60] because they cool down faster leading to a higher attenuation too.

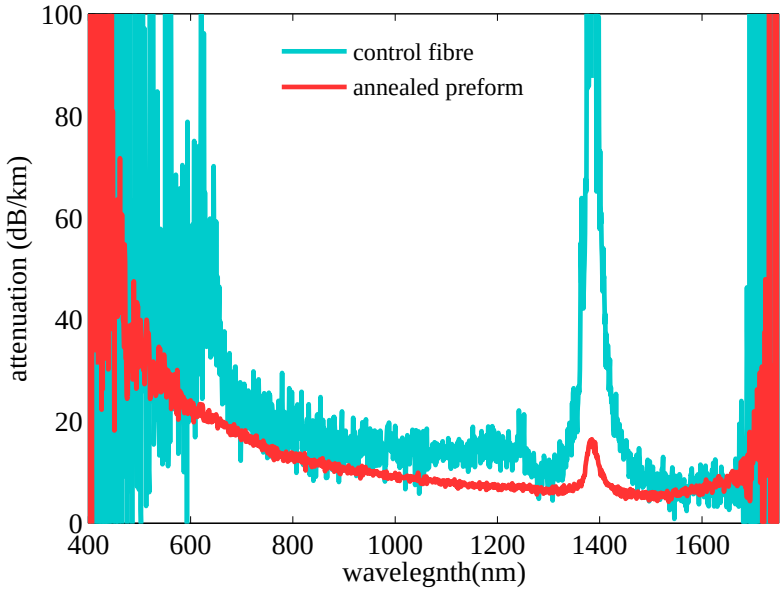

Figure 4-12: Spectral attenuation for 2μm core PCF's, the blue curve corresponds to that of the control fibre fabricated with no special treatment to reduce OH content, and the red curve to that of the fibre obtained after preform annealing.

4.5.3 SC-PCF Fabrication for high humidity conditions

A second stack with 3 rings was drawn following the same fabrication process as before but the attenuation observed (not shown) was extremely high, the relative humidity in the fabrication room was 60 RH% (much higher than for the previous stack) and a temperature of 20°C. Still under high humidity (60 RH%) the fabrication of a third stack with 3 rings was carried out implementing the protecting atmosphere, fast fabrication and annealing fabrication methods. To perform the fast stacking, some modifications were done and are listed below.

Preparation

The rig to stack the capillaries, consists of a fixed base of stainless steel and 4 movable steel supports that can be adjusted to the size of the stack.

1. Set the first 2 supports of the stacking to a separation of 7.3 mm (see Figure 4-13)
2. Place an anti-static bar and N_2 flow above the stacking rig
3. Prepare a plastic tube with nitrogen flowing through it to store the central rod

Stack fabrication

1. Draw all the packing rods
2. Draw the central rod (normally a few were drawn in case of accidental breakage)
3. Keep the rod protected from moisture inside the plastic tube with nitrogen flowing in it
4. Draw capillaries and stack immediately after being collected
5. To form the first half of the three ring structure four rows are stacked (21 capillaries) and then central rod is put in place as depicted in Figure 4-13.
6. The upper stacking supports are added to maintain the stack shape
7. Continue to collect and stack the remaining capillaries until the structure is finished

Cane fabrication

1. Jacket the stacked structure immediately after finishing it. Previously using a glass cutter a slot was made at 8 cm from the end of the jacketing tube, the slot will be used to connect the vacuum afterwards.
2. Connect N_2 flow at one end of the preform through a nitrile glove attached to the preform at one end with PTFE tape.
3. Place the packing rods in place from the open end
4. The capillaries and packers are hold using PTFE tape so that they don't fall when the stack is set in vertical position.
5. Similarly to the cane preparation described in section 4.3.1 epoxy glue is used to seal the interstitial spaces between capillaries.
6. Brass fittings are placed at the end of the stack to connect vacuum and pressure lines to the stack in order to collapse the interstitial holes and to inflate, if necessary, the holes to maintain the shape.
7. The stack is taken to the tower in order to make the drop off
8. Draw canes
9. Put one cane into a jacketing tube also purged with N_2 immediately after being drawn.
10. Collect and store the other canes plastic tube purged with N_2

Fibre fabrication

1. Place the brass fittings at one end of the preform to connect the vacuum and pressure lines.
2. Prior to drop off N_2 is constantly flowing through the preform
3. Follow the annealing process
4. Do the drop off and draw fibre

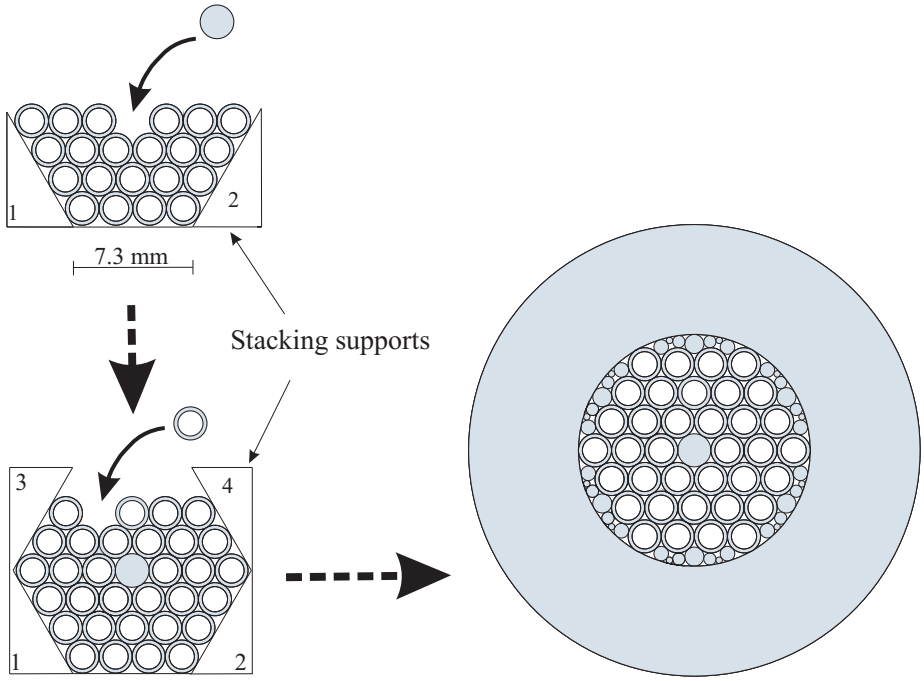

Figure 4-13: 3 ring stack preparation for high RH% conditions: on the stacking rig 21 capillaries were first placed and then the central rod, and subsequently the remaining capillaries were added to form the stack. The stack was jacketed in a thick tube, finally the packing rods were inserted whilst keeping N_2 flowing through the stack.

Low OH small-core PCF and high relative humidity

A 2 μm core fibre derived from the stack fabricated under high RH% combining the protecting atmosphere fast stacking and annealing methods. The attenuation of the 2 μm core fibre derived from annealed preform (experiment in section 4.5.2) is compared to that of the fibre derived from the cane obtained under high humidity in Figure 4-14.

Even under high humidity conditions it was possible to obtain a fibre with reasonably low OH with an absorption at 1383 nm of less than 20 dB/km still higher than 10 dB/km obtained for the fibre fabricated under low humidity conditions. The attenuation at shorter wavelengths is larger for the first fibre and the shape of the spectrum is unusual and was not observed in any other fibres.

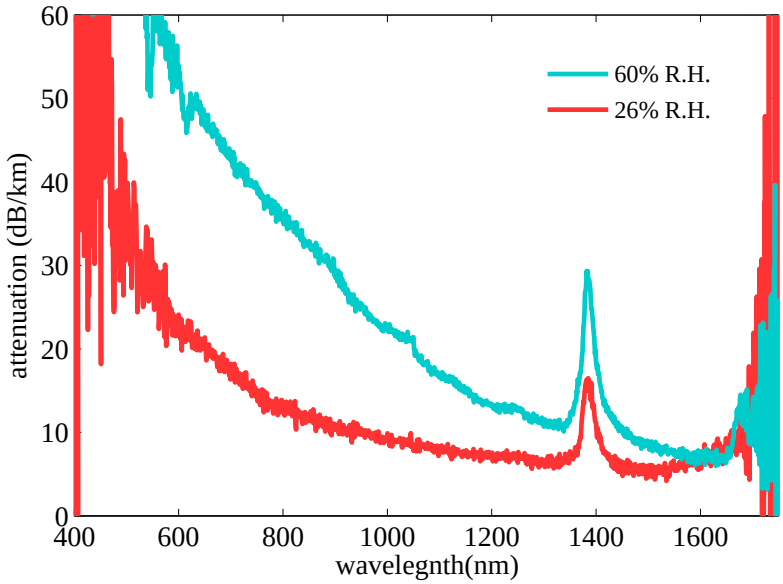

Figure 4-14: Spectral attenuation for 2μm core diameter PCF's. The curve showing a higher attenuation (blue line) corresponds to the fibre derived from stack and canes fabricated under high relative humidity (60 RH%) combining the protecting atmosphere, fast stacking and annealing methods whereas the other spectrum corresponds to a fibre drawn from stack and canes fabricated with only 26 RH% using only the annealing method.

Despite core diameter is the same in both fibres, the OH absorption observed at 1383 nm is different, on the red curve it is 10 dB/km whereas the height corresponding to the other fibre is roughly 20 dB/km. Thus taking into account the uncertainty (2.4 dB/km) in the best case the difference of OH levels between those two fibres would be 5.2 dB/km which is not exaggeratedly different but no insignificant. In this case the fabrication conditions were clearly different (i.e. higher RH%).

4.5.4 SC-PCF attenuation dependence on core diameter

To fabricate PCF's with core diameters ranging from 1.2 to 2 μm the cladding geometry was formed by three rings, and to obtain the fibres with core diameter >2 μm (4 μm, 4.5 μm and 6 μm) the cladding was formed by one ring. Figure 4-15 shows the spectral attenuation of the

fibres obtained. Four of the curves presented correspond to the PCF's with core diameters of 2 μm, 1.5 μm, 1.4 μm and 1.2 μm drawn from a single cane during the same fibre draw in that order. The feed speed and temperature settings were changed when reducing the core size of the fibres to avoid fibre break. For fibres with core diameter of 2.0 μm and above the tension (190 g) and draw speed (32 m/min) were kept very similar, to avoid fibre break the tension in fibres with diameters below 2.0 μm was reduced to 140 g and the draw speed 42 m/min. Both preforms were annealed prior to fibre draw, RH% during fibre draw was 35% and 27% for cores with diameters >2 μm and <2 μm respectively. The attenuation observed for the series of fibres used in this experiment increases for the fibres with smaller core diameters. As expected confinement losses are observed from 1500 nm in Figure 4-15 for the 1.2 μm core fibre, because the wavelengths is comparable and even larger than the core diameter and a significant part of the mode is not confined to core coupling to the cladding modes scattering out the fibre.

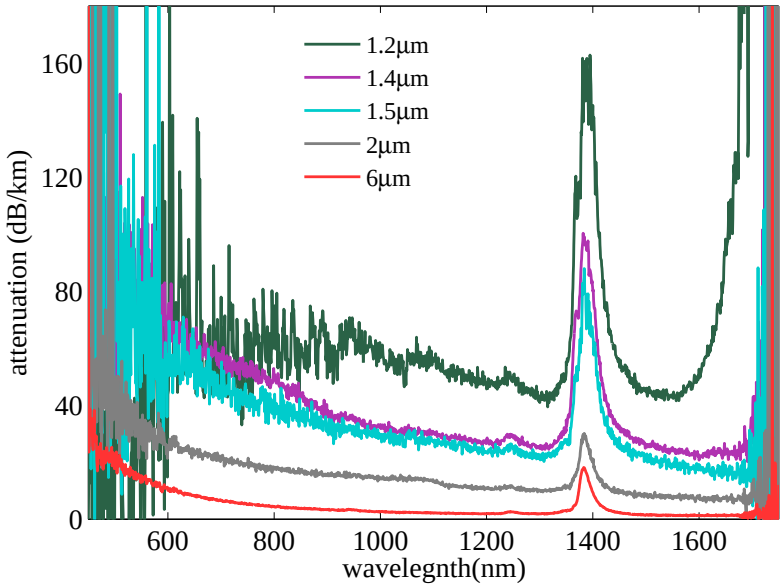

Figure 4-15: Spectral attenuation of low OH PCF with different core sizes derived from annealed preforms. From top to bottom: 1.2 μm, 1.4 μm, 1.5 μm, 2 μm, and 6 μm core diameter.

Investigation on the attenuation dependence on core diameter

The attenuation observed for fibres as a function of core diameter is presented in Figure 4-15, and in Figure 4-16 the magnitudes of the background and OH absorption at 1383 nm

are presented. The attenuation at 1383 nm for fibres of core diameters >2 μm maintains an almost constant level of approximately 20 dB/km, showing a rapid increase for core diameters <2 μm to values above 100 dB/km, while in the background scattering loss is also observed to increase more rapidly for core diameters <2 μm. For the 1.2 μm core diameter fibre confinement losses are clearly observed above 1500 nm.

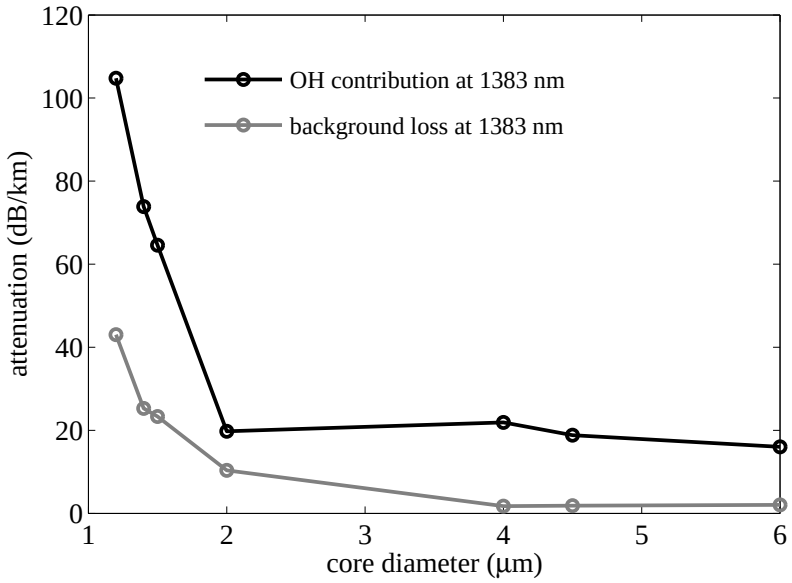

Figure 4-16: Magnitude of spectral attenuation measured at 1383 nm increases dramatically for fibres with a core size below 2 μm. The background loss component due to scattering also increases for small-core sizes and follows the behaviour of the ratio of volume area increase which is expected.

Three possibilities were considered to explain such growth in the absorption at 1383 nm for core diameters <2 μm. Surface scattering causes a generalized increase in attenuation and increases as core size decreases [85] but this does not explain the dramatic increase of attenuation at the OH overtone. The second possibility is the generation of more lattice defects associated with the damage of the silica network as a consequence of reducing the core of the fibre. That would facilitate the creation of sites where OH can bond and diffuse by vacancy hopping or interstitial mechanisms [40, 42]. Such defects can be expected to increase if the same size preform is drawn to a smaller final fibre as in the experiments performed. A third option to explain the increased attenuation for small-core fibres is the diffusion of contaminants (H or OH) on the surface a short absolute distance into the core during the fibre draw. For large cores the contaminated area would represent only a small fraction of the total area whereas for a small-core fibre the same diffusion length represents

a greater percentage of the total area contaminated by OH. Therefore the overlap of the fundamental guided mode with the contaminated walls of a large core is limited and small compared to the overlap of the fundamental mode guided in a small-core fibre with the same degree of OH contamination. The power of the fundamental mode as a function of distance from the core surface was calculated numerically using the finite element method (FEM). The calculations were performed for a circular strand of pure silica surrounded by air which is a good approximation to the highly non-linear PCF's used experimentally. The core geometry was modelled as a silica rod surrounded by a ring of OH doped silica, where the diffusion length of OH into the silica core is the ring thickness. To investigate the influence and changes on the total power of the OH contaminated region the ratio (P_{ratio}) between the power of the mode that overlaps with the contaminated ring (P_{ring}) and the total power of the mode (P_{total}) was calculated for different diffusion lengths and different core diameters, being $P_{ratio} = P_{ring}/P_{total}$. The plots of this ratio are presented in Figure 4-17. The conjectured diffusion lengths used ranged from 0.10 μm to 0.80 μm and the core diameters from 1 μm to 6 μm.

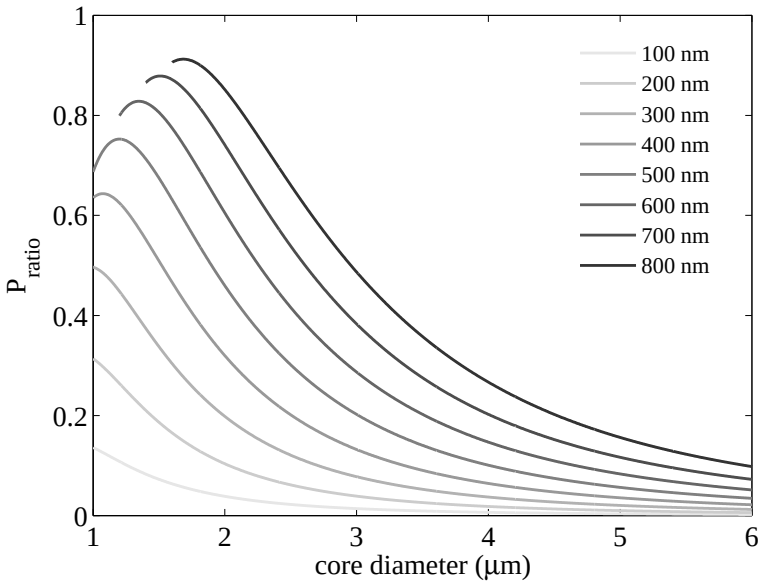

Figure 4-17: Ratio between the power of the fundamental mode contained within a diffusion ring starting at the core surface and the total power of the guided mode as a function of core diameter represented by by P_{ratio}). Each curve is calculated for diffusion lengths ranging from 0.1 μm to 0.8 μm for core diameters ranging from 1 μm to 6 μm. Curves do not go to unity because some of the total power resides outside the core

There is an increasing trend of P_{ratio} with decreasing core observed for core diameters

<2 μm in Figure 4-17 but is not enough to explain the observations from experiments as presented in Figure 4-16.

The observed correlation between the appearance of the 630 nm absorption band and an increased absorption at 1383 nm suggests that an increased number of lattice defect sites is generated in smaller-core fibres, which could explain the strong dependence on the attenuation at 1383 nm for small-core diameter fibres. The concentration of OH in silica is related to the absorption strength at 1383 nm [84], and as observed for small-core fibres the attenuation corresponds to a higher OH concentration to that specified in the raw materials. So it appears likely that the extra OH contamination is due to extrinsic OH diffusing from the surfaces of the silica into the bulk medium by diverse mechanisms [40, 42] (see 2.3), if the OH groups are assumed to bond in the same way for large and small cores.

Silica properties are determined to a great extent by the reaction of water vapour with the material defects. Extensive research about the interaction of OH groups and silica fibres has been done [62, 123], identifying different absorption wavelengths that depend on the chemical bonding of OH with silica. The fundamental OH absorption band is commonly decomposed into four Voigtian components [63, 66, 67, 124] which relate to OH groups bonded to silica in distinct manners. The different configurations identified are: hydrogen bonded (linear or cyclic configuration) or non-hydrogen bonded (free OH and weakly bonded to a bridging oxygen) [67] which absorb at different wavelengths. The concentration of OH in silica is not equivalent to IR absorption, because there are different concentrations for each configuration and a particular absorption intensity and wavelength is associated to each type. The probability of the light interacting with OH (i.e. being absorbed) depends on the OH group itself which has an associated concentration in the glass. If by reducing the core size the most absorptive OH group becomes more abundant, (i.e. hydrogen bonded OH groups), and at the same time the amount of the less absorptive OH groups (free OH for example) is reduced [36], that would explain the dramatic increase of the absorption at the first OH overtone for small-core fibres. Research related to intrinsic formation of OH in silica under thermal treatments is proposed [125] that could also contribute to the final levels of OH in the fibres, but that was not investigated in the experiments carried out by the author. The high absorption in small-core fibres at 1383 nm is worthy of further investigation to understand more fully the mechanisms of losses in silica fibres that could lead to further loss reduction in small-core PCF's.

4.6 Conclusions

With the atmospheric control method the attenuation was reduced for 5 μm core diameter fibres to 8.6 dB/km at 1383 nm corresponding to an OH concentration of 0.14 ppm and

1.5 dB/km of background absorption. The implementation of this method for large cladding structures to obtain small cores is impractical. By means of the time control fabrication process it was demonstrated the importance of exposure of drawn material to laboratory environment, as the lowest attenuation was achieved by the fastest fabrication turn around.

The annealing method was shown to effectively reduce OH absorption in PCF's derived from OH contaminated canes. It is simple to implement, with no extra chemical dehydration or etching. The annealing method is the only method that was found to obtain low loss fibres with core diameters <2 μm. In this work the author reported a 2 μm core SC-PCF with 11.6 dB/km of OH absorption (corresponding to 0.19 ppm of OH) and 7.6 dB/km of background absorption at 1383 nm.

Although sometimes the variations on the OH content measured for the SC-PCF's exceed the uncertainty (see Figure 4-14), the conclusions drew from the spectral attenuation of the fibres obtained from the experiments described in this thesis (using different fabrication methods) are nevertheless consistent, i.e. the 630 nm absorption peak was observed only when the absorption at 1383 nm was was above 22 dB/km.

Regarding the strong dependence of attenuation on core diameter, the dramatic attenuation increase observed for fibres with core sizes below 2 μm at 1383 nm can not be attributed solely to the losses due to the overlap of the fundamental mode with the OH contaminated core walls. Future work to investigate the underlying mechanism of the huge absorption increase at the first OH stretching overtone is worthy and the author foresees two possible directions. One is the intrinsic generation of OH during thermal treatments [125] and the other the growth of concentration of specific OH configurations like the OH group hydrogen bonded in cyclic configuration whose absorption is many times that of free OH groups [67], which could give place to the dramatic raise in the absorption at 1383 nm. It would be interesting to establish whether it is possible to fabricate very low loss small-core PCF's.

Chapter 5

Attenuation degradation of unsealed photonic crystal fibres caused by OH with time

The holes that run along the length of PCF's to form both a photonic crystal cladding or a hollow core are essential for their performance and advantageous for a range of uses including guiding light in air [79], particle guidance [126], or sensing applications [127–133]. It is precisely the hollow nature of these fibres that makes them prone to contamination and to subsequent degradation of their performance, particularly at OH related wavelengths. This can potentially impact PCF's applications which require low attenuation like CW supercontinuum generation [111] or soliton self-frequency shift (SSFS) [115]. Also mechanical failure observed in standard optical fibres is associated with corrosion caused by OH diffusion and formation [15]. PCF's used in laboratories for experimental work are commonly not protected from environmental contamination (i.e. water vapour), causing degradation of their performance particularly at 1364 nm and 1383 nm, which are related to the surface OH [69] and the first OH stretching overtone [64] respectively. Such degradation was in fact observed to affect the performance of the fibres used in the experiments related to SSFS described in Chapter 6 which motivated the investigation of PCF's time-dependent degradation caused by OH contamination [134] presented in this chapter.

5.1 Fabrication of PCF's for degradation experiments

To perform the series of experiments regarding the degradation of fibres, three solid-core PCF's (SC-PCF's), were specially fabricated with low OH content using the annealing fabrication method [37] described in Chapter 4, named A, B and C of 1.3 μm, 2.26 μm and 5.2 μm core diameter respectively. A hollow core PCF (HC-PCF) named fibre D fabricated with the low-loss transmission window centred at 1365 nm, the fibre was derived from a cane provided by Dr. B. J. Mangan. The spectral attenuation of all fibres shown in Figs. 5-1 and 5-2 was measured just after fibre fabrication using a tungsten lamp as white light source and an optical spectrum analyser (OSA). SEM pictures of the fibres are shown in Figure 5-3. The drawing fabrication parameters, and the core and cladding holes diameters are presented in table 5.1.

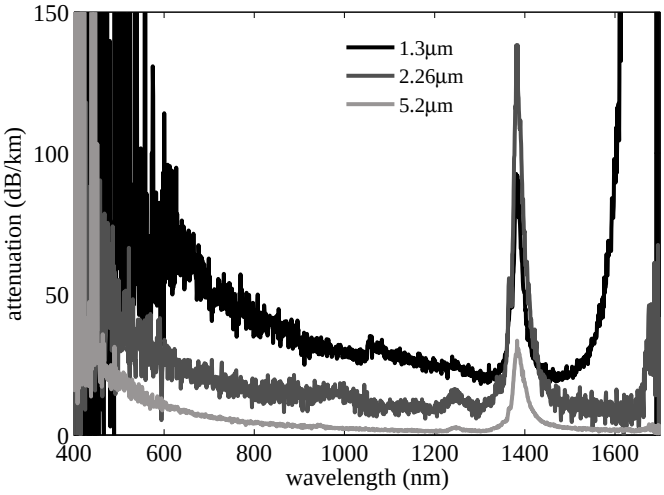

Figure 5-1: Spectral attenuation of the SC-PCF's with core diameters of 1.3 μm, 2.26 μm and 5.2 μm used in the fibre degradation experiments.

fibre	type	cladding hole diameter (μm)	core diameter (μm)	tension (g)	DDR
A	$SC-PCF$	1.16	1.3	142	15384.61
B	$SC-PCF$	1.8	2.26	190	8810.57
C	$SC-PCF$	9.44	5.2	180	3846.15
D	$HC-PCF$	3.4	10.03	162	N/A

DDR= Draw down ratio

Table 5.1: **Fibre drawing parameters**

As observed in Figure 5-1 the spectral attenuation for the small-core diameter fibres

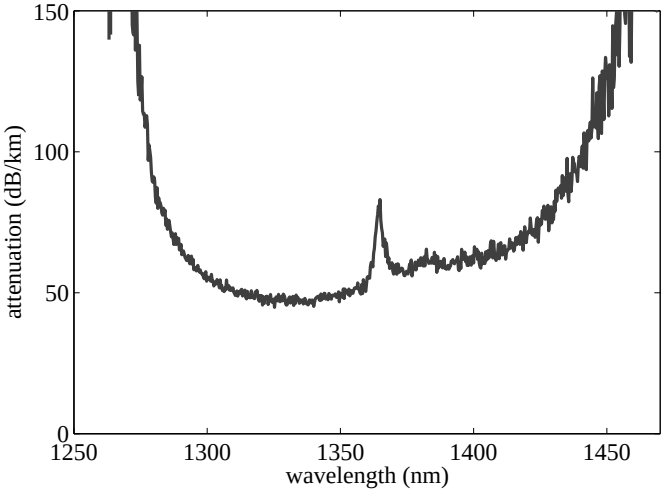

Figure 5-2: Spectral attenuation of the HC-PCF used in the fibre degradation experiments.

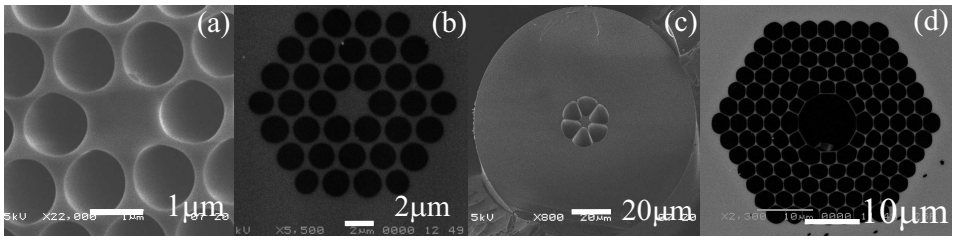

Figure 5-3: SEM pictures of the fibres used for the experiments. (a) 1.3 μm (fibre A), (b) 2.26 μm (fibre B), (c) 5.2 μm core diameter (fibre C) SC-PCF and (d) HC-PCF (fibre D).

(1.3 μm and 2.26 μm) is higher than that for the 5 μm core. In the spectrum from the 1.3 μm core diameter fibre an increased background scattering is observed and on the long wavelength range above 1450 nm the confinement losses [91–93] start to appear evident, the wavelength is longer than the core size so the light is not strongly confined. Because of the bandgap guiding mechanism the attenuation for the HC-PCF is observed in a narrower wavelength range (see Figure 5-2) than the observed for the SC-PCF's.

5.2 Time-dependent degradation of PCF's attenuation

The experiments carried out to investigate the effects of atmospheric exposure on the SC-PCF's and HC-PCF consisted of regularly measuring the transmission of the fibres exposed to laboratory conditions with unprotected ends over a minimum of 24 weeks [134]. The measurements were performed in the range from 1350 nm to 1450 nm using a fibre based supercontinuum as white light source coupled to the core of the fibre under test and recording its spectral transmission with an OSA. The spectrum from a tungsten lamp is flat in the region of interest thus spectrally neutral and convenient when analysing the transmission data. However a source with higher intensity was required to spectrally resolve the features at 1364 nm and 1383 nm for fibres A and B with core diameters of 1.3 μm and 2.26 μm respectively, hence the use of a supercontinuum source. The fibre lengths used to monitor the changes were 25 m for fibres A and B, 30 m for fibre C and 50 m for fibre D. The lengths were chosen so that the absorption at 1364 nm and 1383 nm could be measured since the first measurement, the length was short enough so that it would allow to measure the evolution even if the peak increased. Longer lengths would have resulted in weak and noisy signal.

5.2.1 SC-PCF's transmission degradation with time

In Figs. 5-4, 5-5, 5-6 and 5-7 the transmission measurements taken over time for fibres A, B, C and D respectively are presented. The spectrum of the SC source was recorded for each measurement, an example is illustrated in Figure 5-8b. The data represented in the fore mentioned figures is already corrected i.e. the corresponding SC spectrum was subtracted as explained in section 5.2.2. The curves were made to coincide at 1350 nm at this wavelength the spectra did not change much when coupling the supercontinuum source to the fibre core for each measurement, the transmission changes at the wavelengths of interest are easier to note. One possible reason for the difference in the transmission spectra at long wavelengths might be the result of coupling the light into slightly different position of the fibre core. The fluctuations seen in Figure 5-7 are due to H_2O vapour present in laboratory.

The absorption strength at 1364 nm, 1383 nm and 1398 nm visibly increased for all fibres

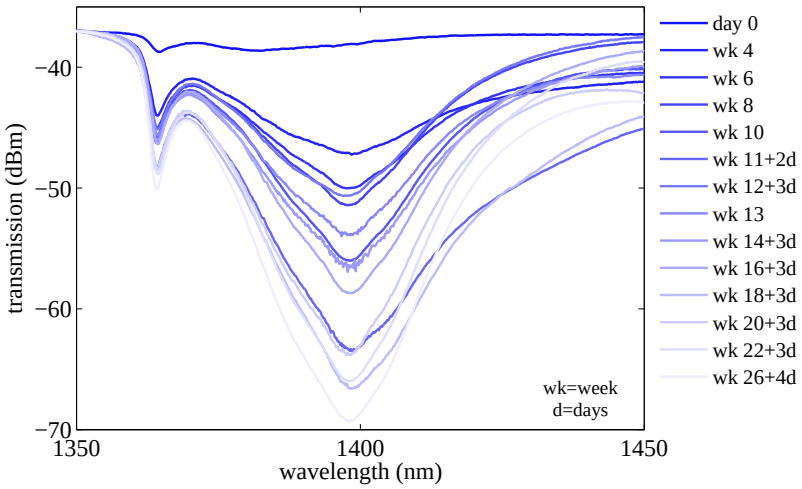

Figure 5-4: Transmission observed over 26 weeks on the 1.3 μm diameter fibre where the non conventional absorption peak located at 1398 nm dominates . The top curve (dark blue) is the transmission measured on day 0, the curve in the lightest blue corresponds to that measured on week 26.

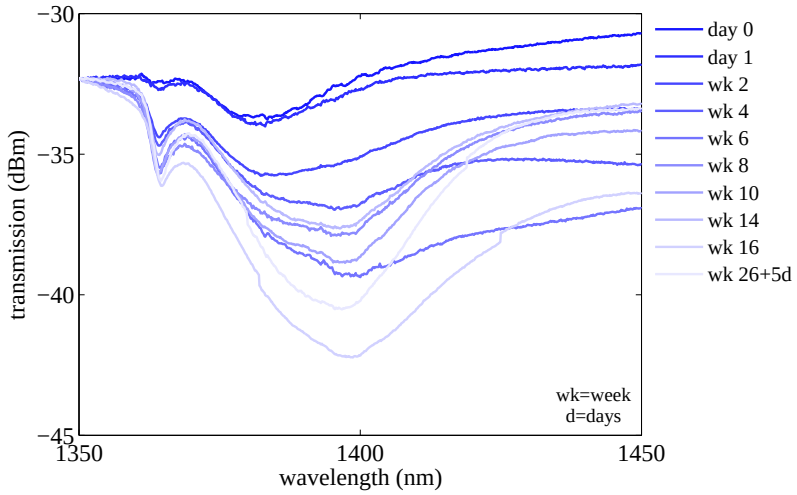

Figure 5-5: Transmission observed over 26 weeks on the 2.26 μm diameter fibre. The top curve (dark blue) is the transmission measured on day 0, the curve in the lightest blue corresponds to that measured on week 26.

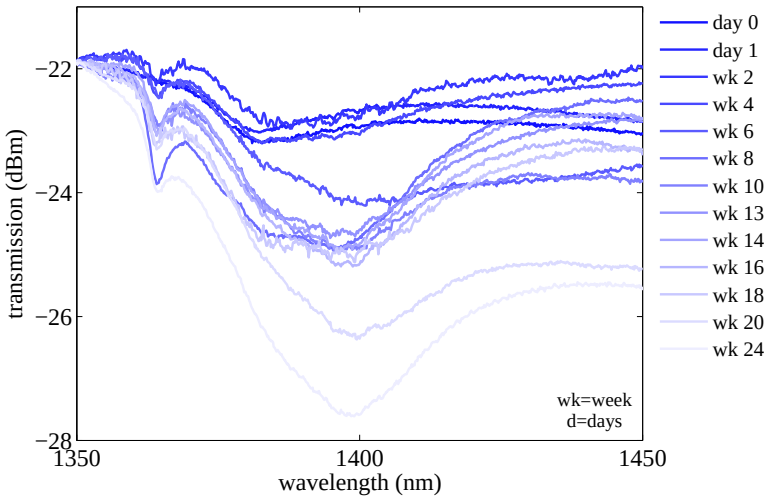

Figure 5-6: Transmission observed over 24 weeks on the 5.2 μm diameter fibre. The top curve (dark blue) is the transmission measured on day 0, the curve in the lightest blue corresponds to that measured on week 24.

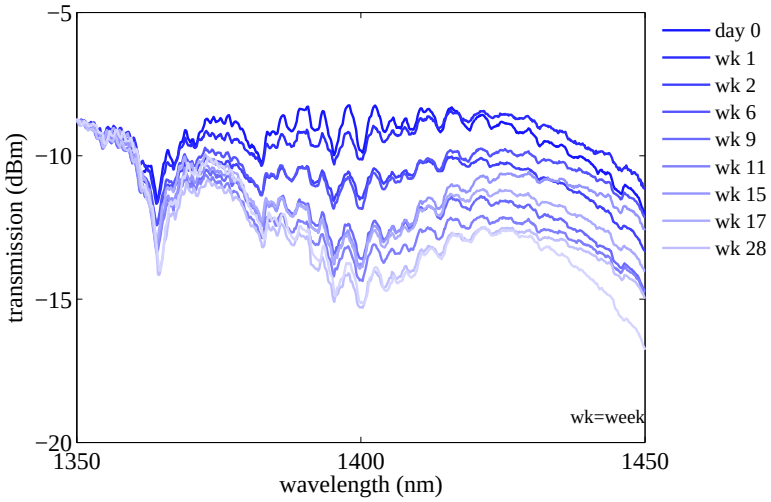

Figure 5-7: Transmission observed over 28 weeks on the HC-PCF. The top curve (dark blue) is the transmission measured on day 0, the curve in the lightest blue corresponds to that measured on week 28.

after their exposure to laboratory conditions over 24 weeks. To obtain the strength of such absorption bands the data were analysed as described in the next section.

5.2.2 Time-dependent absorption strength at 1364 nm, 1383 nm and 1398 nm

For all the fibres the recorded transmission data included the spectral contribution of the supercontinuum source. So as to extract the information related only to the fibre under test, the spectral contribution of the light source from the transmission measurements was eliminated by dividing the raw transmission data by the corresponding supercontinuum spectra, obtaining sets of *clean transmission data*. An example of the raw data, a supercontinuum spectra and clean transmission data is illustrated in Figure 5-8. Using the sets of *clean transmission data* the absorption strengths were calculated relative to a reference point defined at a nearby wavelength. In the case of the surface OH absorption band at 1364 nm the reference point was the value at 1364 nm of the straight line calculated to join the transmission points at 1360 nm and 1370 nm as illustrated in Figure 5-9. Also illustrated in Figure 5-9 is the reference point used to calculate the absorption strength at 1383 nm and 1398 nm, which was the value of the transmission at 1350 nm of the clean transmission data. The absorption strength is the difference between the transmission value at the reference point and the measured value at a particular wavelength which in this case were 1364 nm, 1383 nm, and 1398 nm.

The values of the absorption strength, as seen in Figs 5-10, 5-11, and 5-12, correspond to the growth of the absorption with time at 1364 nm, 1383 nm, and 1398 nm respectively, and are referenced to the absorption initially measured so that for time zero (when the fibre was initially exposed to atmosphere) the growth of the absorption is zero.

As seen in the transmission and growth absorption Figures (Figs. 5-4, 5-5, 5-6, and 5-7 and in Figs. 5-10, 5-11 and 5-12 respectively) the absorption at 1364 nm, 1383 nm and 1398 nm increased with time for all fibres. Due to practical reasons the transmission data points for fibres A and C were obtained in each case from two identical fibres resulting in a break in the curves but no real change in trend. The absorption of the smallest core fibre (1.3 μm diameter) shows the largest growth during the exposure time for all the wavelengths observed. Compared to the 1383 nm and 1398 nm peaks the growth of the surface OH absorption peak is modest. The broad absorption feature centred at 1398 nm, which to the knowledge of the author has not been reported before, was observed to become stronger with time, developing faster and more strongly in the case of 1.3 μm core fibre appearing after only 2 weeks of exposure. Although not as strong it is also observed in the 2.26 μm core fibre, and for the 5 μm core fibre this broad feature appears more clearly after week 20. As

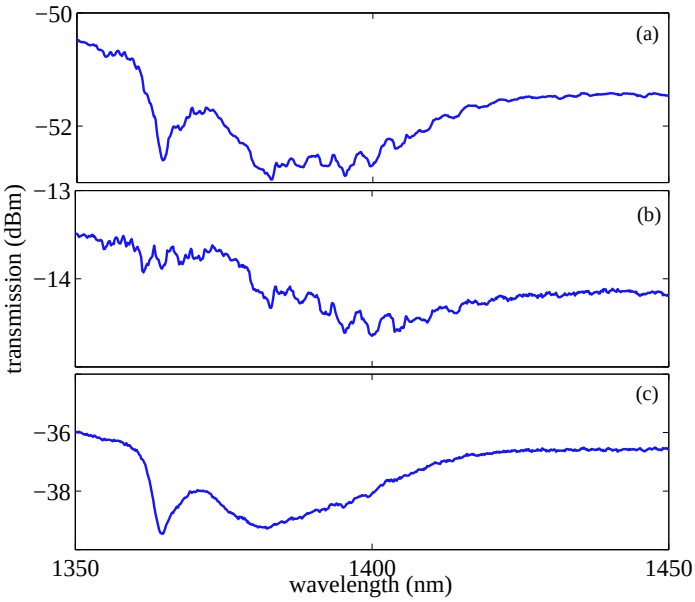

Figure 5-8: Example of transmission spectra from 1350 nm to 1450 nm of (a) the experimental data including the contribution of supercontinuum (raw data), (b) supercontinuum only and (c) the experimental data without the contribution of supercontinuum (clean data).

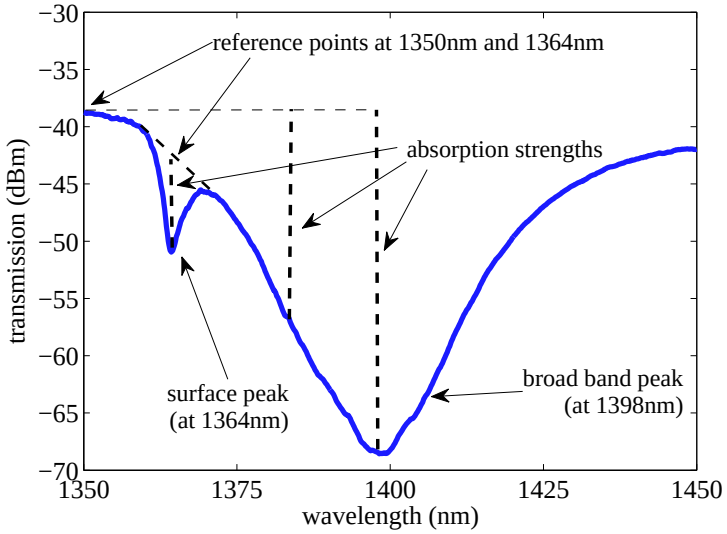

Figure 5-9: Illustration of the reference points used to calculate the absorption strengths at 1364 nm, 1383 nm and 1398 nm.

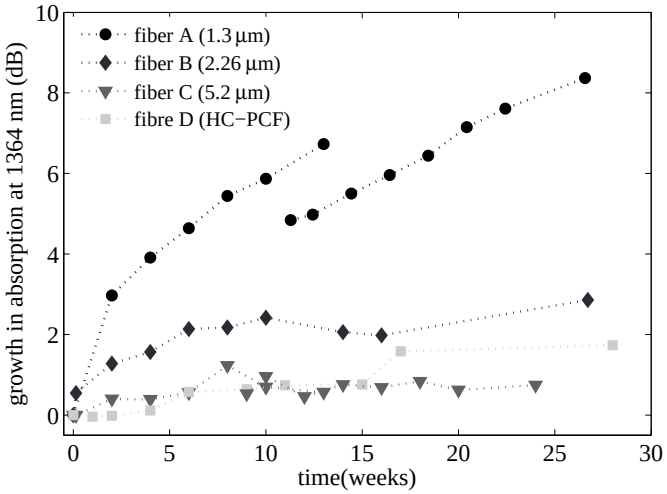

Figure 5-10: Growth of the absorption at 1364 nm with time for different core sizes 1.3 μm (circles), 2.26 μm (diamonds), 5.2 μm (triangles), and HC-PCF (squares).

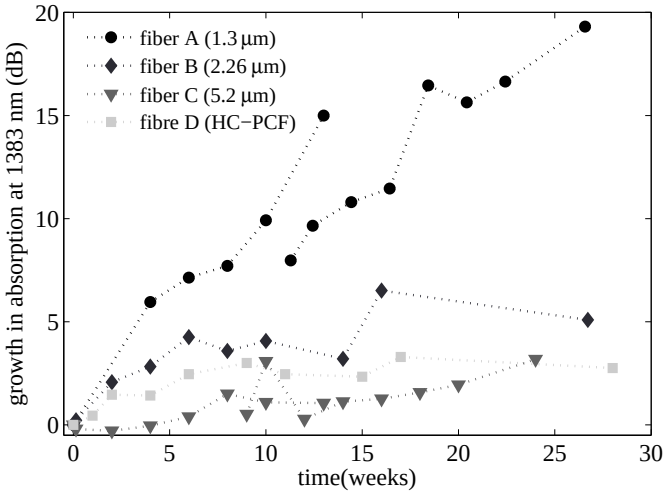

Figure 5-11: Growth of the absorption at 1383 nm with time for different core sizes 1.3 μm (circles), 2.26 μm (diamonds), 5.2 μm (triangles), and HC-PCF (squares).

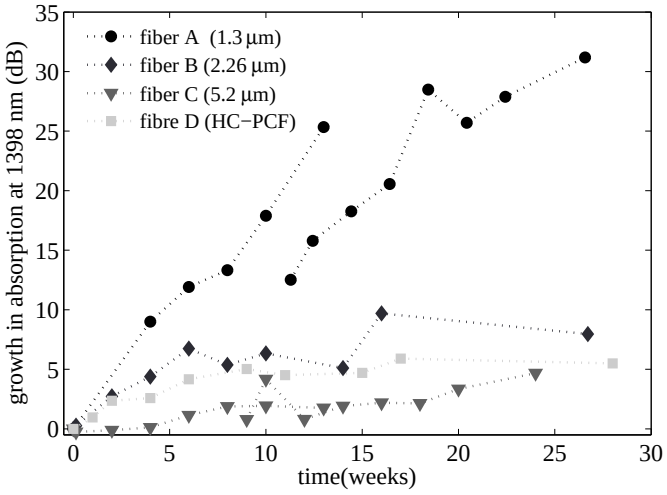

Figure 5-12: Growth of the absorption at 1398 nm with time for different core sizes 1.3 μm (circles), 2.26 μm (diamonds), 5.2 μm (triangles), and HC-PCF (squares).

the HC-PCF has virtually no bulk silica glass the increased absorption at 1383 nm is most probably related to the tail of the broad band absorption at 1398 nm. Because the broad feature also appears in fibre D the author of this thesis speculates that the absorption at 1398 nm is related to an interaction of the silica surface and OH (given that silica bulk in HC-PCF's is practically non-existent).

In silica fibres the concentration of defect sites (which depends on drawing temperature, drawing speed and fibre diameter) also called E$'$ centres is larger on the surface than in the centre of the fibre according to Hanafusa et al. [27] and Yin et al. [29]. The fibre core geometry can be described as a cylinder in which the surface to volume relation is 2/r where r is the core radius. This implies that for a fixed volume of silica glass, as r gets smaller more of that material is on the core surface. This is particularly relevant for the degradation of small SC-PCF's in that there is larger surface per unit of volume where defects form and therefore the core is more prone to degradation, matching the observed fast degradation.

The number of defects is also related to the thermal history of the preform so that the number of defects is higher for higher values of fictive temperature T_f [123]. During the draw of the different fibres the tension, temperature and drawing speed were very similar, as opposed to the large difference between the DDR's (draw down ratio) (table 5.1) of the different fibres in particular between fibre A and C. The DDR is the scaling factor between the original rod diameter and the final core diameter in the fibre. Fibres A and B were derived from a preform with a diameter larger than the diameter of the preform to fabricate fibre C. Therefore in order to obtain a small-core diameter and an acceptable fibre diameter

for fibres A and B a larger DDR is required compared to that used to scale down the preform to obtain fibre C (see table 5.1). This implies a different thermal history and consequently different T_f which ultimately defines the degree of susceptibility to OH contamination in the fibres.

Mobility and abundance of OH is closely related to site defects in the silica network (i.e. broken Si−O bonds), therefore the degradation observed in Figs. 5-4, 5-5, 5-6, and 5-7 is directly related to the defect centres on the silica surface determined by the T_f. In summary the more defects sites on the silica core surface the more OH formation is possible and its subsequent diffusion to the silica bulk is reflected in the absorption growth at OH related wavelengths in silica fibres.

5.3 Localization of PCF's degradation due to OH contamination

The degradation observed for all fibres, expressed as an increased absorption at OH related wavelengths and as a generalized increased absorption, was hypothesized to originate at the fibre ends contaminated with OH after being exposed to laboratory conditions. Therefore, to determine the degradation dependence on the length of the contaminated fibre ends cut-back transmission measurements were performed on the same fibres used in the time-dependent experiments [134] described in section 5.2.

5.3.1 Cutback transmission measurements for the PCF's contaminated ends

The supercontinuum light source was coupled into the core at one of the fibre ends, and transmission was measured. Next, a short length of fibre was removed from the output end, and the transmission measured through the remainder. This cutback transmission measurement procedure was repeated until no change was observed in the spectrum. Subsequently the fibre ends were exchanged so that the light was coupled into the core of the recently cleaved fibre end and the still contaminated end connected to the OSA to measure the spectrum. The procedure described above was followed, removing a short length and measuring the transmission until the spectrum did not change.

In Figs. 5-13, 5-14, 5-15 and 5-16 the clean transmission measured for different lengths is presented for the 1.3 μm, 2.26 μm, 5.2 μm core diameter (SC-PCF's) and the HC-PCF respectively, the lengths used are labelled on the corresponding figures. Also respectively the fibres were exposed for 26 weeks and 4 days, 26 weeks and 5 days, 24 weeks and 28 weeks.

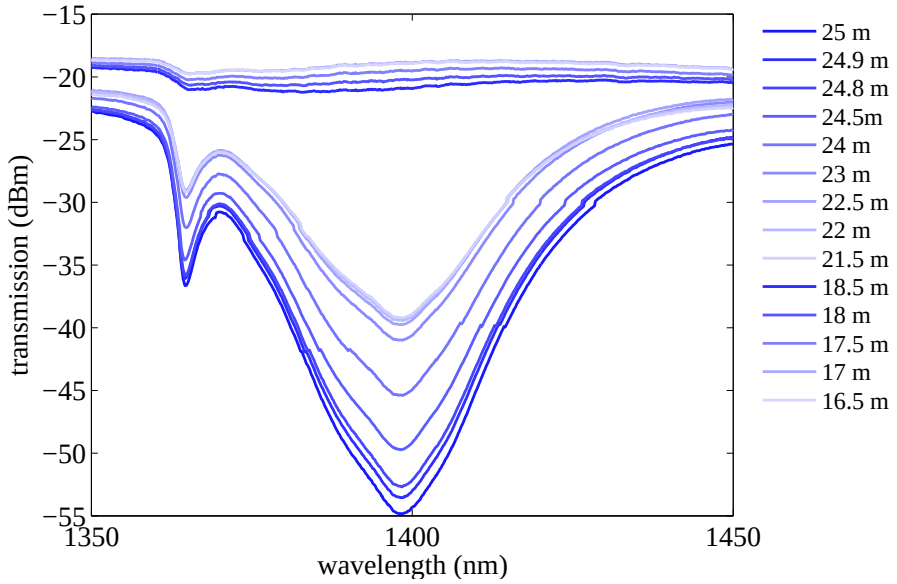

Figure 5-13: Cut back transmission measurements of the 1.3 μm core fibre for different lengths. Starting from 25 m (bottom) to 21.5 m on one end, and from 18.5 m to 16.5 m (top) on the other end. The data files corresponding to the fibre length between 21.5 m to 19 m were damaged so no transmission data is available at those lengths.

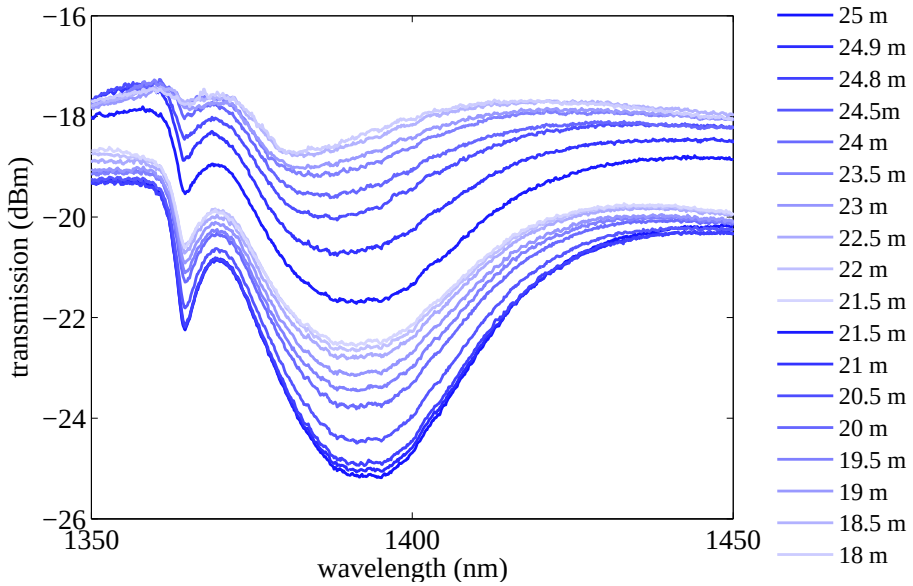

Figure 5-14: Cut back transmission measurements of the 2.26 μm core fibre for different lengths. Starting from 25 m (bottom) to 21.5 m on one end, and from 21.5 m to 18 m (top) on the other end.

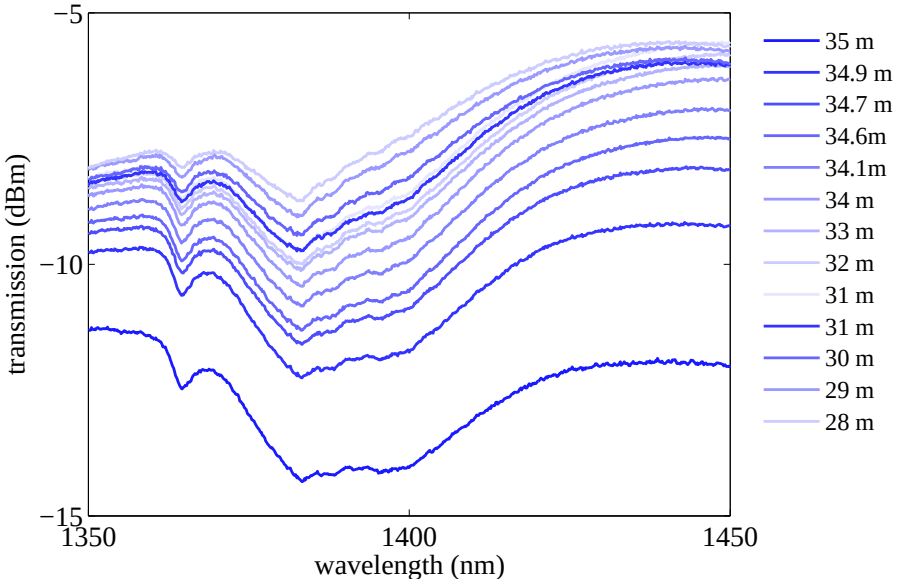

Figure 5-15: Cut back transmission measurements of the 5.2 μm core fibre for different lengths. Starting from 35 m (bottom) to 31 m on one end, and from 31 m to 28 m (top) on the other end.

Comparing the cutback transmission measurements shown in Figure 5-17 it is observed a relationship of the absorption peak situated at 1900 nm with the absorption bands at 1364 nm, 1383 nm and 1398 nm. As the contaminated ends were removed, the long wavelength absorption peak as well as the peaks at 1364 nm 1383nm and 1398 nm were reduced to the original levels. An absorption band located at 1894 nm, that corresponds to stretching mode of OH and the second SiO_4 vibration mode (ν_3+2ν_1), was reported for silica fibres by Humbachh et al. [84] but the separation of such vibration modes can not be identified in our observations.

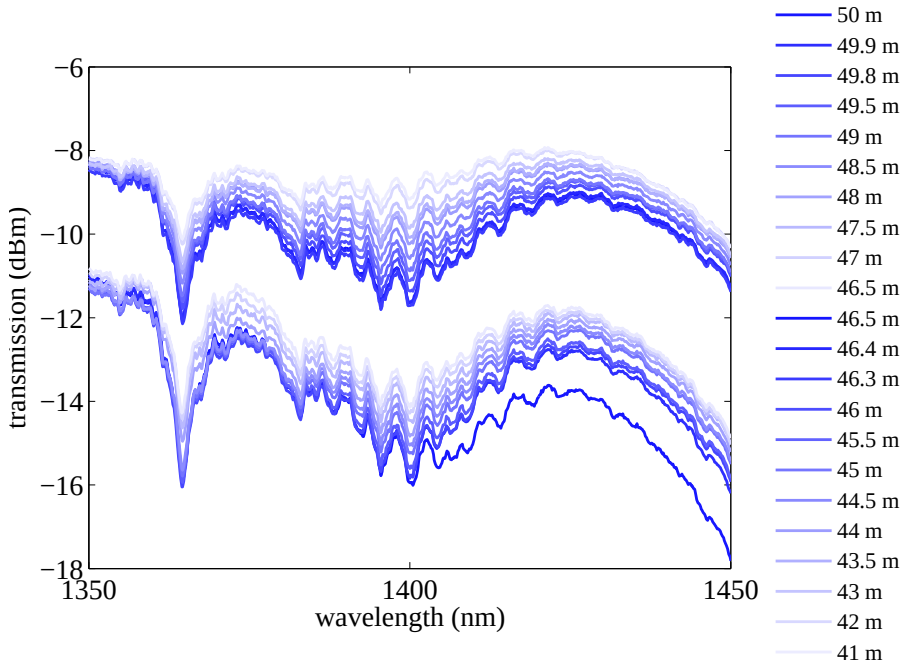

Figure 5-16: Cut back transmission measurements of the HC-PCF for different lengths. Starting from 50 m (bottom) to 46.5 m on one end, and from 46.5 m to 41 m (top) on the other end.

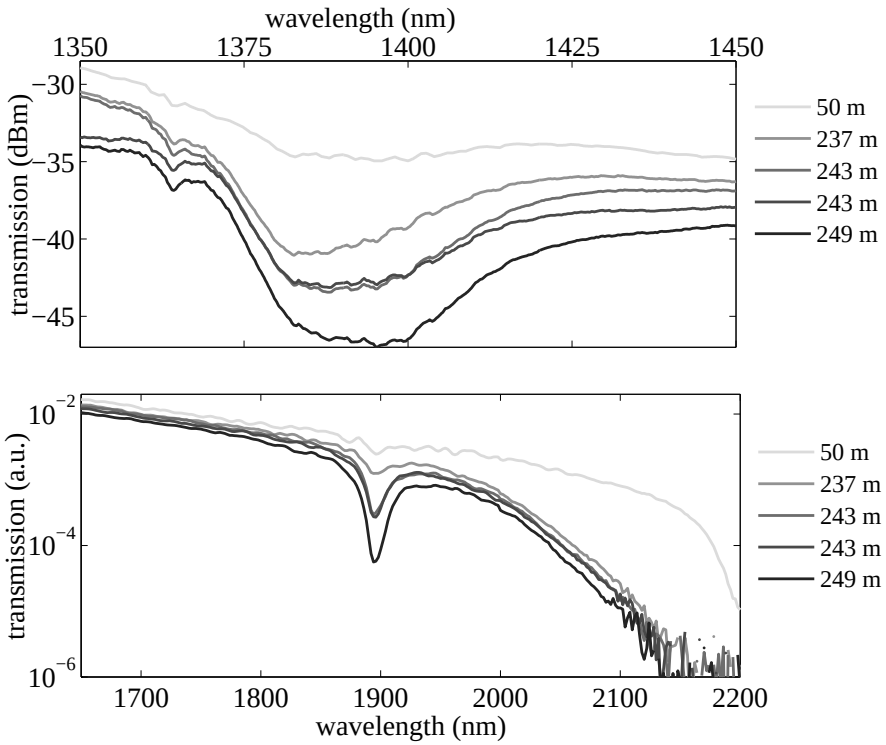

Figure 5-17: Cutback transmission measurements for a low loss 5μm core fibre exposed over 2 years to atmospheric conditions. Top: from 1350 nm to 1450 nm. Bottom: from 1650 nm to 2200 nm. For both ranges the transmission was measured over 249 m, 243 m and recoupling onto the other end then measuring over 243 m, 237 m and 50 m.

5.3.2 Position-dependent PCF transmission at 1364 nm, 1383 nm and 1398 nm

The same procedure used in section 5.2 to calculate the absorption strength for the time-dependent experiment was used to analyse the data of the localised degradation experiment obtaining the absorption strength at the fibre ends for the different fibres. The absorption obtained for all the fibres decreased as the contaminated ends were removed, which is equivalent to an increasing transmission as presented in Figs. 5-18, 5-19, 5-20 and 5-21. The data points are represented in each figure by circles, diamonds, triangles and squares which correspond to fibres A, B, C and D respectively. The values of the data points represented were normalised by the respective initial transmission value measured for each fibre.

For the different fibres the transmission dependence on the length of the contaminated ends, is compared at 1364 nm, 1383 nm and at 1398 nm in Figure 5-22. The data presented in Figs 5-18, 5-19, 5-20 and 5-21 are generally well fitted to exponential curves which are plotted on the same figures. Such fits describe the localization of degradation in the fibres' ends, and the exponential model used is described in the following section.

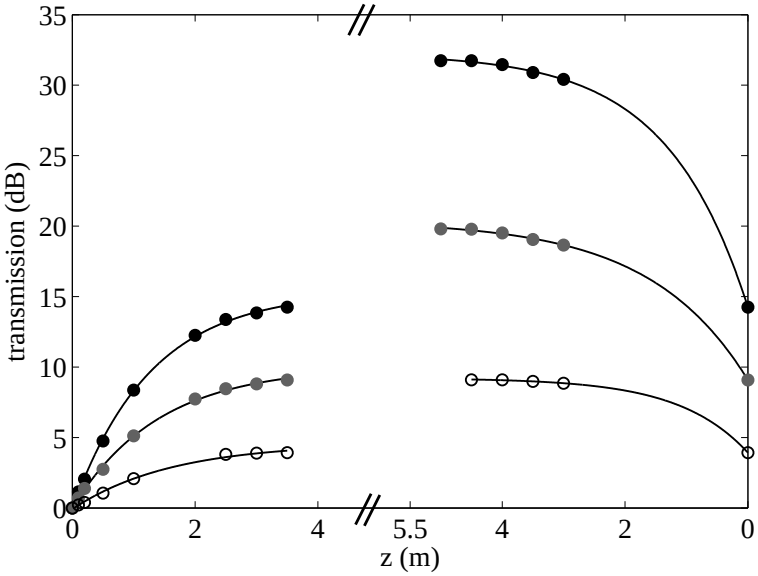

Figure 5-18: Increasing transmission observed for fibre A (1.3 μm core diameter) as the contaminated ends were removed. The circles correspond to data points at 1364 nm (white), 1383 nm (grey) and 1398 nm (black) and the lines correspond to the exponential fits, z is the length of the removed fibre ends from the 25 m long fibre. The data points were obtained from the measurements presented in Figure 5-13, the left set from x=25 m to x=21.5 m (from left to right) and the right set correspond to x=18.5 m down to x=16 m (from right to left).

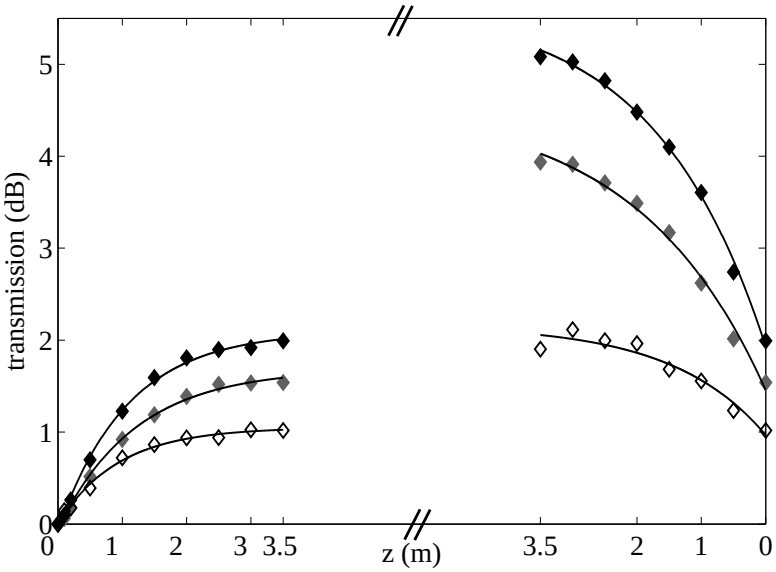

Figure 5-19: Increasing transmission observed for fibre B (2.26 μm core diameter) as the contaminated ends were removed. The diamonds correspond to data points at 1364 nm (white), 1383 nm (grey) and 1398 nm (black) and the lines correspond to the exponential fits, z is the length of the removed fibre ends from the 25 m long fibre. The data points were obtained from the measurements presented in Figure 5-14, the left set from x=25 m to x=21.5 m (from left to right) and the right set correspond to x=21.5 m down to x=18 m (from right to left).

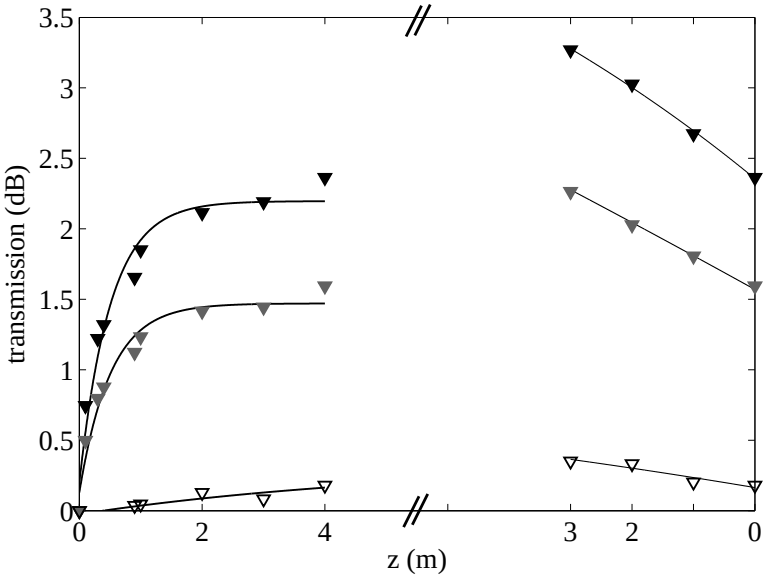

Figure 5-20: Increasing transmission observed for fibre C (5.2 μm core diameter) as the contaminated ends were removed. The triangles correspond to data points at 1364 nm (white), 1383 nm (grey) and 1398 nm (black) and the lines correspond to the exponential fits, z is the length of the removed fibre ends from the 35 m long fibre. The data points were obtained from the measurements presented in Figure 5-15, the left set from x=35 m to x=31 m (from left to right) and the right set correspond to x=31 m down to x=28 m (from right to left), the data points taken for the last set along with the level of OH contamination were not enough to observe the exponential trend as observed for the other end.

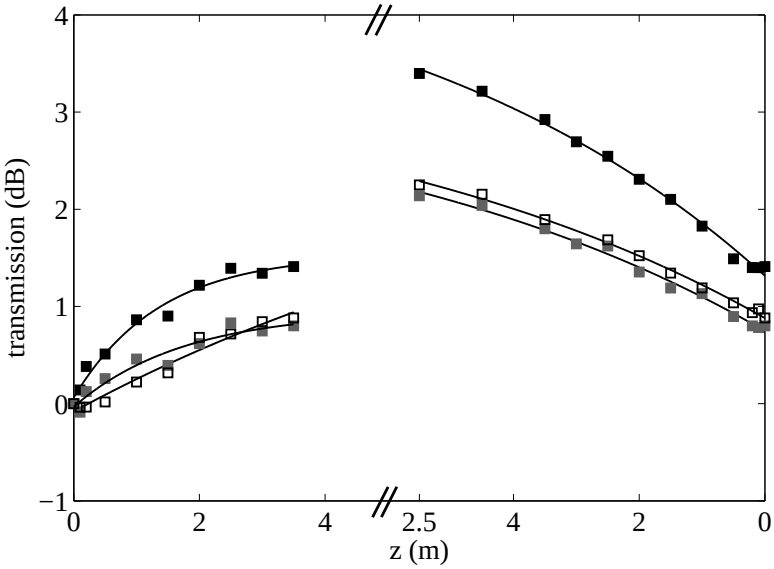

Figure 5-21: Increasing transmission observed for fibre D (HC-PCF) as the contaminated ends were removed. The squares correspond to data points at 1364 nm (white), 1383 nm (grey) and 1398 nm (black) and the lines correspond to the exponential fits, z is the length of the removed fibre ends from the 50 m long fibre. The data points were obtained from the measurements presented in Figure 5-16, the left set from x=50 m to x=46.5 m (from left to right) and the right set correspond to x=46.5 m down to x=41 m (from right to left).

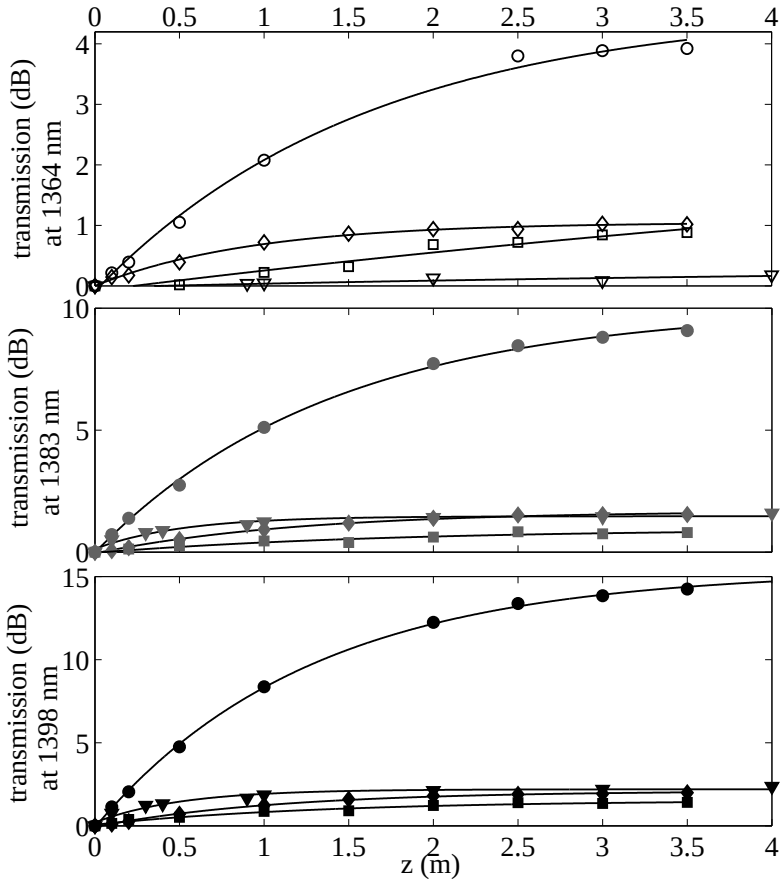

Figure 5-22: Comparison of the transmission of the experimental data and corresponding exponential fits in relation with the removed length of the contaminated ends. From top to bottom 1364 nm, 1383 nm and 1398 nm. Data points: circles correspond to a diameter of 1.3 μm, diamonds to 2.26 μm, triangles to 5.2 μm and squares correspond to the HC-PCF

5.4 Position-dependent PCF local attenuation

The model that fully describes the changes in the fibre transmission depending on the length of the contaminated ends is:

$$y(z) = a \cdot e^{b \cdot z} + c + \alpha_0 \cdot z \tag{5.1}$$

where y is the logarithm of the transmission that depends exponentially on length z (in m), a (in dB) is a scaling factor, $a+c$ is the initial value when $z=0$, b>0 in m^{-1} is the growth rate of the exponential which is interpreted as the change in transmission per unit length, c (in dB) is the value of the transmission on the fibre with uniform distribution of contaminants and α_0 is the value in dB/m of the initial attenuation (measured just before the experiments started). In this model the term $a \cdot e^{b \cdot z}$ dominates for small values of z whereas the term $\alpha_0 \cdot z$ dominates for long fibre lengths. This means that the transmission for short distances (i.e. fibre ends) is described well enough by the exponential term.

The position dependent local attenuation $\alpha(z)$ of the contaminated fibre ends is the derivative of equation (5.1):

$$\frac{dy}{dz} = \alpha(z) = a \cdot b \cdot e^{b \cdot z} + \alpha_0. \tag{5.2}$$

Equation (5.3) is obtained considering that $\alpha_0 << \alpha$ at the contaminated ends whose lengths are short compared to the total fibre length. The multiplying factor of 1000 is introduced to obtain α in dB/km

$$\alpha(z) = 1000 \cdot a \cdot b \cdot e^{b \cdot z} \tag{5.3}$$

According to this approximation, the data plotted in Figs. 5-18, 5-19, 5-20 and 5-21, (that correspond to the normalized transmission values from the localised of degradation experiments), were fitted to the exponential model described in equation (5.4), where α_0 is neglected

$$y(z) = a \cdot e^{b \cdot z} + c \tag{5.4}$$

The local attenuation represented in Figs. 5-23, 5-24, 5-25 and 5-26 was obtained from the derivative of the exponential fits. The level of OH contamination at one end of the 5.2 μm core fibre (fibre C) as well as the number of data points taken (from x=31 m to x=28 m Figure 5-20) were not enough to see the exponential trend on the transmission after removing the contaminated parts, therefore the local attenuation analysis is presented for one end only as seen in Figure 5-25.

The b coefficients which dictate the contamination growth rate depending on the length are included in table 5.2 for each fibre end. High values of the b coefficient imply that the transmission increases by a factor of e over a shorter length, that is to say that in the case of the 5.2 μm core SC-PCF (fibre C) the concentration of contaminants are mainly located in the first metre. The OH contamination is observed to affect the fibre performance more at 1383 nm and 1398 nm as an increased absorption. One would expect that with bigger holes water vapour is liable to enter a longer length into the fibre structure to subsequently contaminate the core silica bulk. However, being the holes surrounding the 5.2 μm core fibre larger than those of the small-core fibres, the observed degradation at the OH related wavelengths is not larger for bigger holes after one meter of contaminated ends. This can be observed in the local attenuation comparison for all the fibres at 1364 nm, 1383 nm, and 1398 nm in Figs. 5-27, 5-28 and 5-29 respectively. If the number of defects on the core surface is lower, as expected for larger cores, then OH formation on the surface is reduced and so is its further reaction with the silica bulk core. In the case of the 1.3 μm core and 2.26 μm core fibres the transmission at 1364 nm increases over a shorter distance compared to the other fibres. It seems that the amount of OH on the core surface of small-core fibres moves very rapidly towards the core centre increasing the absorption at 1383 nm and 1398 nm as observed in Figure 5-18 for fibre A (1.3 μm).

fibre	@1364 nm(m^{-1})	@1383 nm(m^{-1})	@1398 nm(m^{-1})
$Aend1$	0.6218	0.7131	0.7863
$Aend2$	0.8969	0.6277	0.7599
$Bend1$	1.075	0.8307	0.9221
$Bend2$	0.6887	0.4994	0.5785
$Cend1$	0.1852	1.958	1.98
$Cend2$	N/A	N/A	N/A
$Dend1$	0.1124	0.574	0.731
$Dend2$	0.138	0.1437	0.1631

Table 5.2: ***b* coefficient for fibres A, B, C and D for 1364 nm, 1383 nm and 1398 nm.**

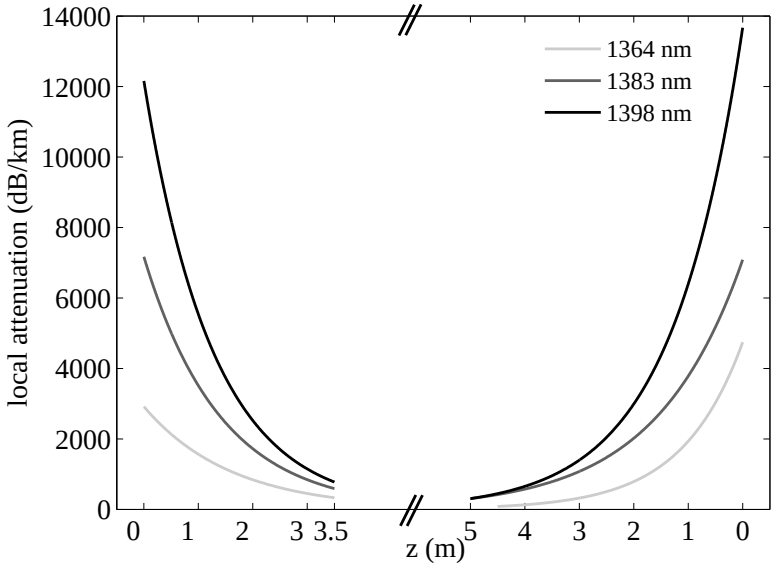

Figure 5-23: Local attenuation corresponding to the contaminated ends (exposed over 26 weeks) of the 1.3 μm core diameter fibre at 1364 nm, 1383 nm, and 1398 nm, z is the length of the removed fibre ends from the 25 m long fibre.

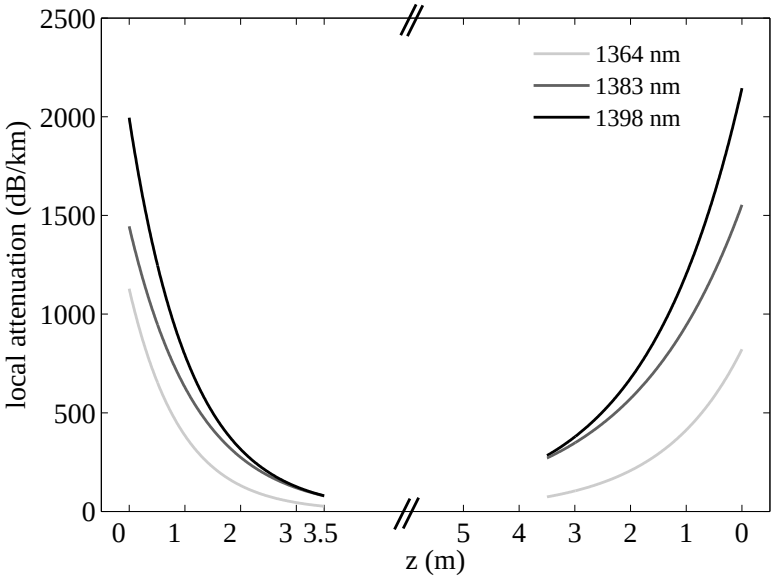

Figure 5-24: Local attenuation corresponding to the contaminated ends (exposed over 26 weeks) of the 2.26 μm core diameter fibre at 1364 nm, 1383 nm, and 1398 nm, z is the length of the removed fibre ends from the 25 m long fibre.

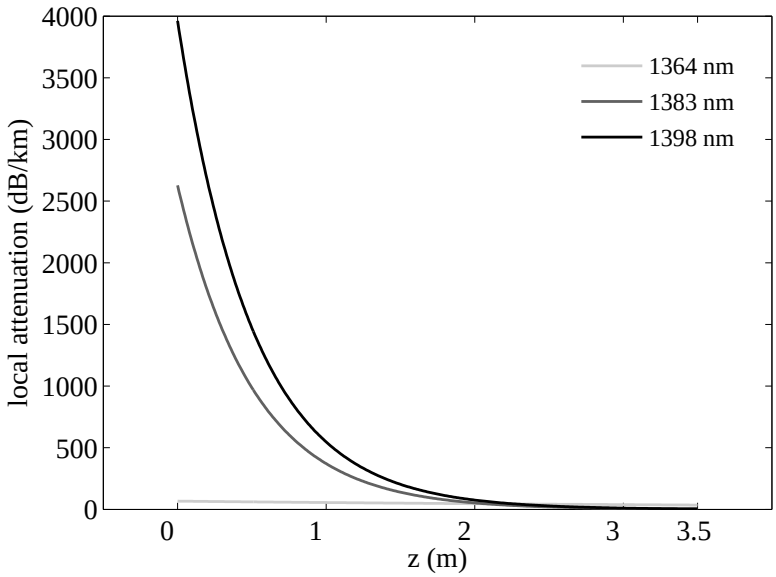

Figure 5-25: Local attenuation corresponding to one contaminated end (exposed over 24 weeks) of the 5.2 μm core diameter fibre at 1364 nm, 1383 nm, and 1398 nm, z is the length of the removed fibre ends from the 35 m long fibre.

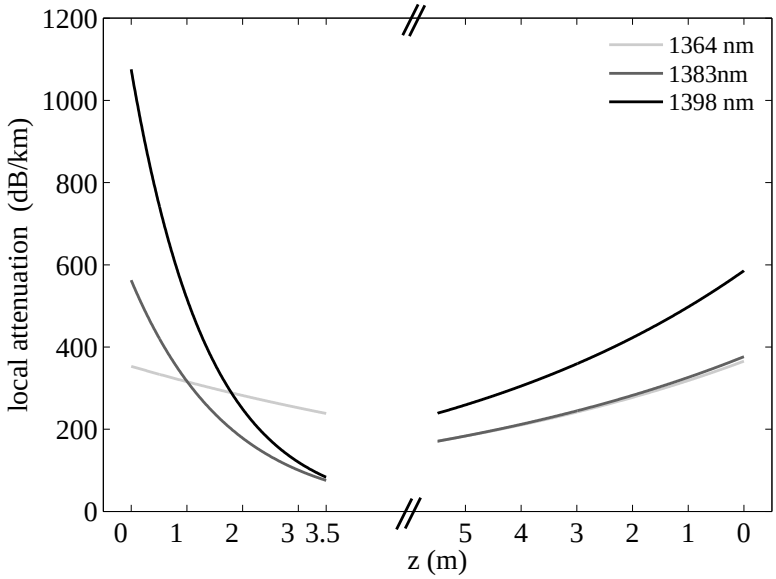

Figure 5-26: Local attenuation corresponding to the contaminated ends (exposed over 28 weeks) of the HC-PCF at 1364 nm, 1383 nm, and 1398 nm, z is the length of the removed fibre ends from the 50 m long fibre.

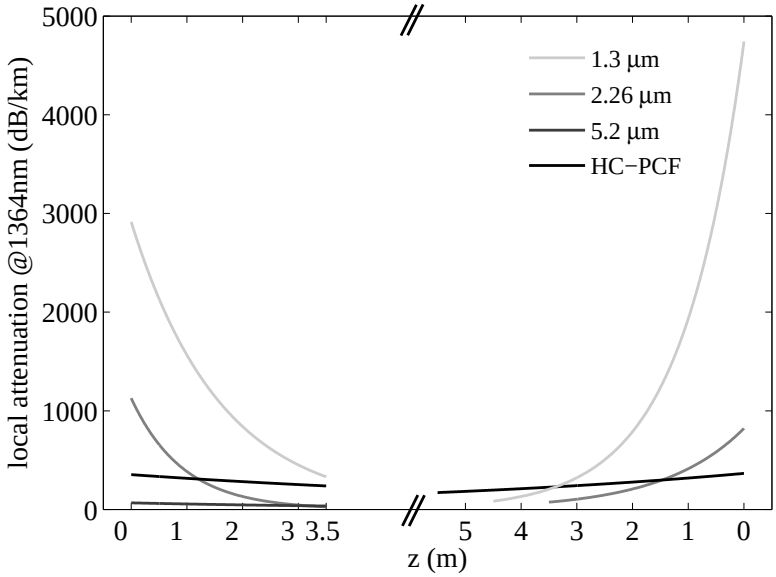

Figure 5-27: Comparison of the local attenuation at 1364 nm for the contaminated ends of fibres with core diameter of 1.3 μm, 2.26 μm, 5.2 μm and HC-PCF, z is the length of the removed fibre ends from the different fibres. The original length of the 1.3 μm and 2.26 μm core fibres was 25 m, 35 m for the 5.2 μm and 50 m for the HC-PCF.

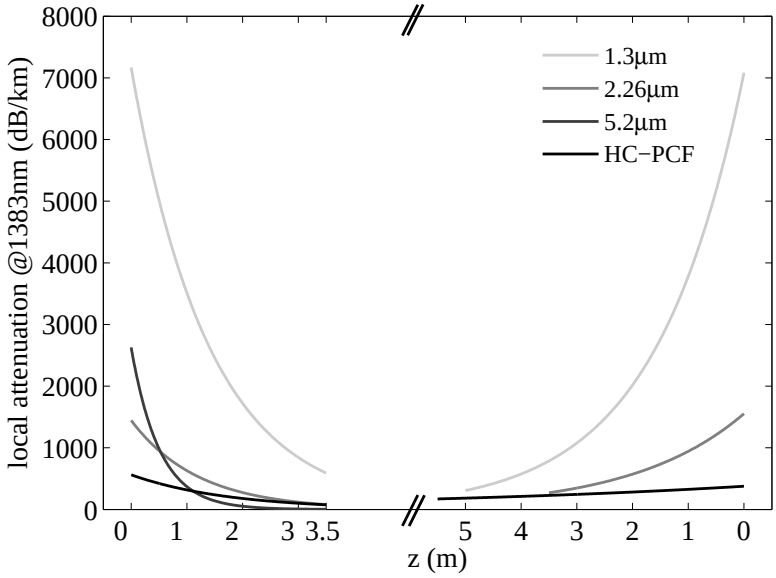

Figure 5-28: Comparison of the local attenuation at 1383 nm for the contaminated ends of fibres with core diameter of 1.3 μm, 2.26 μm, 5.2 μm and HC-PCF, z is the length of the removed fibre ends from the different fibres. The original length of the 1.3 μm and 2.26 μm core fibres was 25 m, 35 m for the 5.2 μm and 50 m for the HC-PCF.

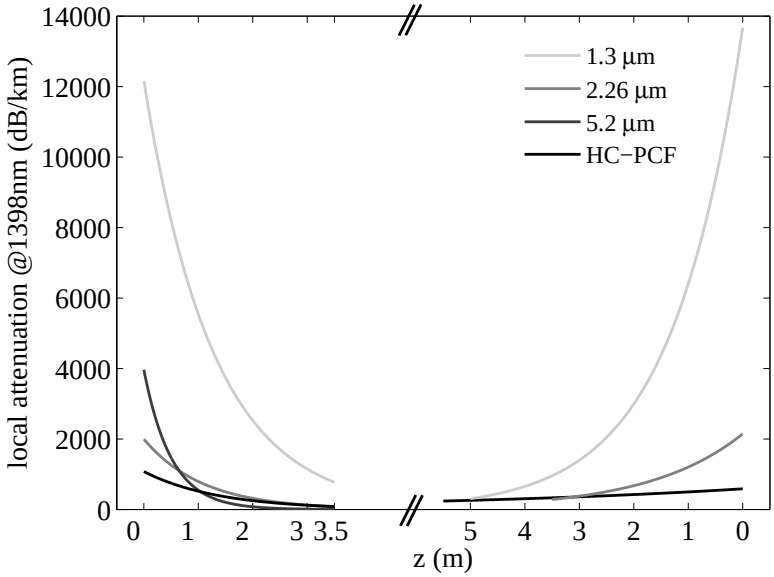

Figure 5-29: Comparison of the local attenuation at 1398 nm for the contaminated ends of fibres with core diameter of 1.3 μm, 2.26 μm, 5.2 μm and HC-PCF, z is the length of the removed fibre ends from the different fibres. The original length of the 1.3 μm and 2.26 μm core fibres was 25 m, 35 m for the 5.2 μm and 50 m for the HC-PCF.

5.5 Atmospheric water vapour inside PCF's air holes

A fine spectral structure was observed in the measured transmission spectra of the HC-PCF (fibre D) exemplified in Figure 5-30. To corroborate the origin of these absorption lines high spectral resolution measurements (0.1 nm) were performed in the range from 1350 nm to 1450 nm using a supercontinuum source for fibre D, and a tungsten lamp as a source for a 9 m piece of SMF-28. Both transmission spectra were recorded with an OSA and are illustrated in Figure 5-31 and 5-32. The absorption lines observed in the transmission measurements of fibre SMF-28 are attributed to water vapour in the laboratory and in the OSA. These fine absorption bands are wavelength coincident to those described by Curcio et al. [135] as absorbing species of atmospheric water vapour. The strength of such absorption is notoriously stronger for fibre D (Figs. 5-31 and 5-32) and is attributed to the presence of water vapour in the cladding and core holes.

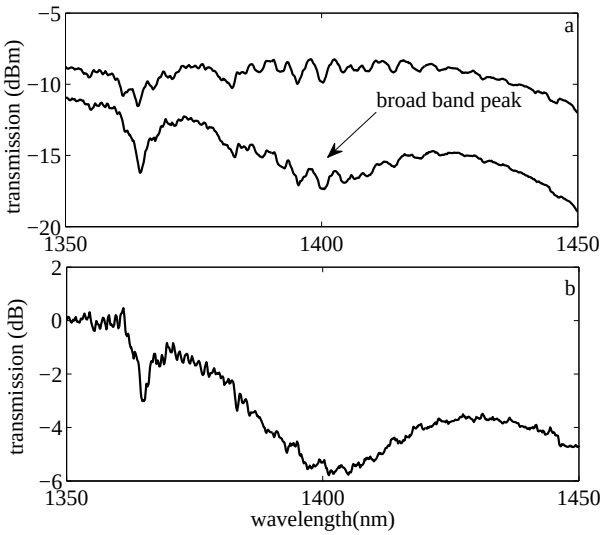

Figure 5-30: a) Transmission spectrum of the HC-PCF measured just after fabrication (top), and after 28 weeks of exposure (bottom). Note the surface peak growth and the appearance of a broad absorption feature. b) Transmission resulting from the difference between both spectra.

A final experiment to support the idea that water vapour contamination enters through the hollow structure of the PCF consisted of measuring the transmission of identical pieces of fibres A (25 m), C (35 m) and D (50 m) just after fabrication, and subsequently sealing the fibre ends using a fibre splicer. The PCF's with fused ends (illustrated in Figure 5-33) were stored for 11 weeks under the same laboratory conditions as the fibres that showed degradation in their transmission. After this period the sealed ends were carefully cleaved in

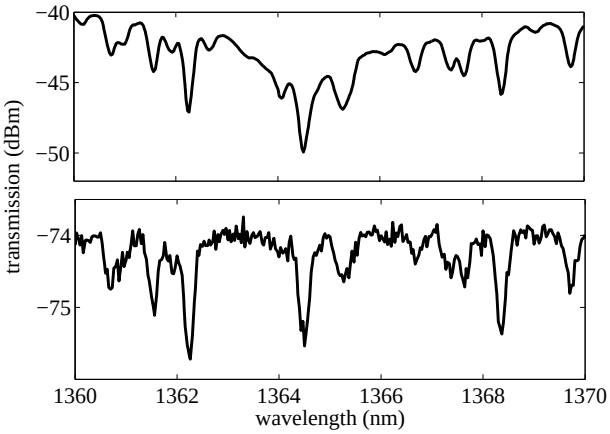

Figure 5-31: Fine spectral absorption bands of atmospheric water vapour [135] observed in the range from 1360 to 1370 observed in fibre D (top) and an SMF-28 (bottom) using 0.1 nm resolution.

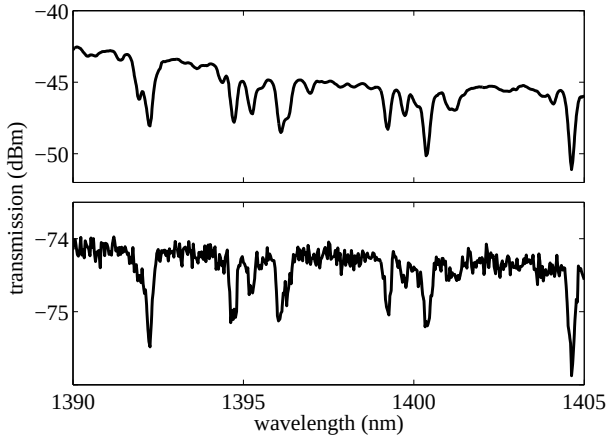

Figure 5-32: Fine spectral absorption bands of atmospheric water vapour [135] observed in the range from 1390 nm to 1405 nm observed in fibre D (top) and an SMF-28 (bottom) using 0.1 nm resolution.

order to perform transmission measurements. Both transmission measurements, before and after end sealing, are compared for each fibre in Figure 5-34, 5-35 and 5-36. Although there is a difference in transmission before and after end sealing it is modest, and small compared to that observed in the fibres left exposed to laboratory conditions the same amount of time with unprotected ends (see Figs. 5-10, 5-11 and 5-12) which confirms that the degradation for all the wavelengths observed is originated by the contamination entering through fibre holes.

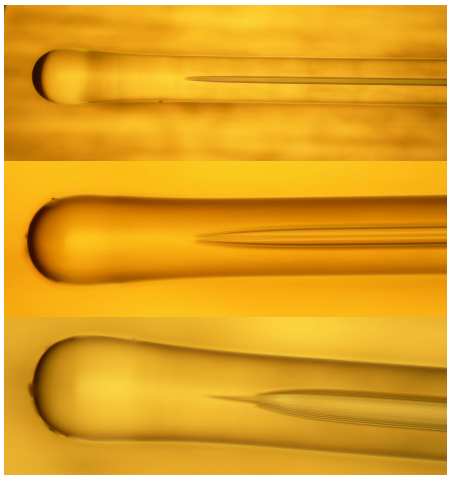

Figure 5-33: Pictures of the sealed ends of the different fibres from top to bottom the SC-PCF's with core diameter of 1.3 μm, 5.2 μm and HC-PCF.

In the case of a SC-PCF the residual valences of the silica core surface Si−O−Si (siloxane) and water vapour, that enters through the cladding holes, react at room temperature covering the core surface with silanol (OH groups) [35]. This causes scattering losses and increased background absorption noticeable in the cutback transmission measurements for all fibres (Figs. 5-13, 5-14, 5-15 and 5-16). OH can subsequently diffuse [40] into the silica fibre core explaining the increased absorption at the contaminated fibre ends at OH related wavelengths. After removing the contaminated fibre ends from all the fibres the losses return to the original levels including the background losses and those of the absorption bands at 1364 nm, 1383 nm and 1398 nm.

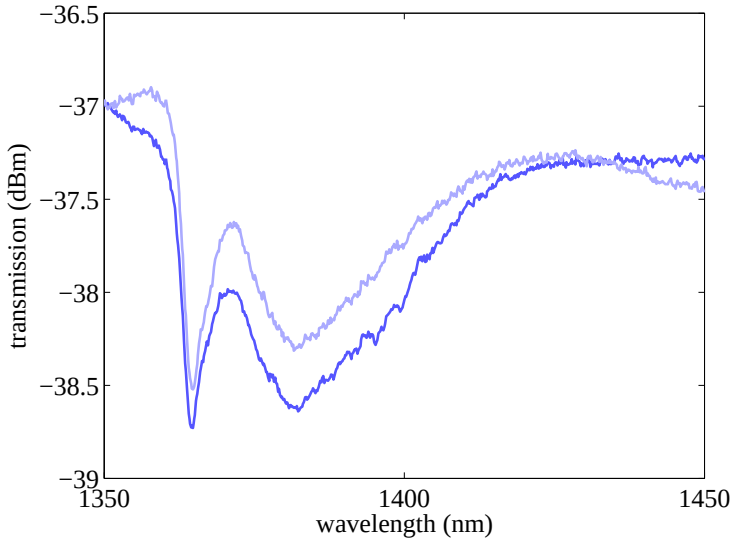

Figure 5-34: Transmission measurements before and after end sealing fibre A (1.3 μm). The fibre ends were sealed for 11 weeks.

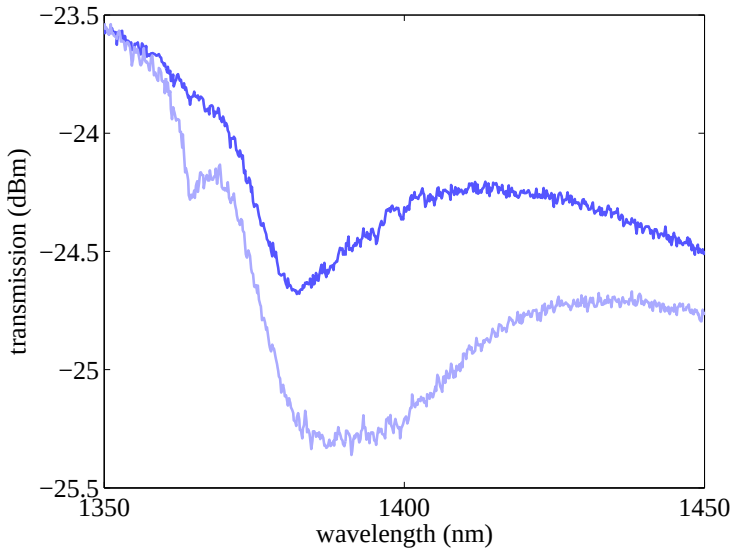

Figure 5-35: Transmission measurements before and after end sealing fibre C (5.2 μm). The fibre ends were sealed for 11 weeks.

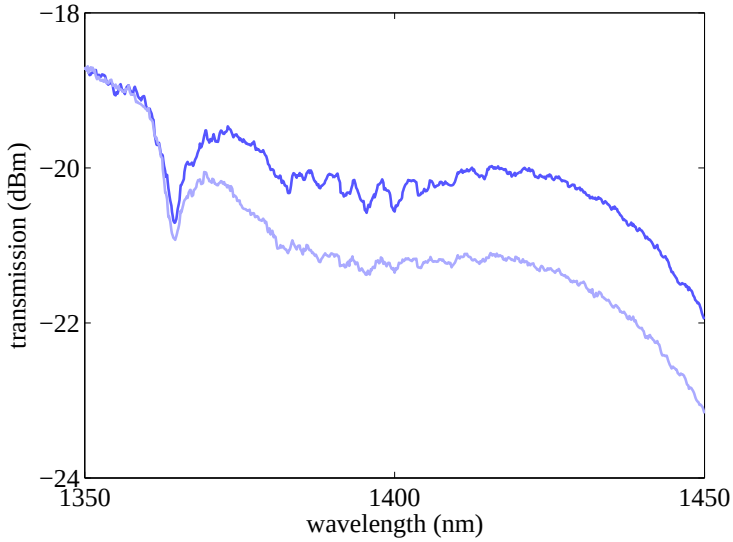

Figure 5-36: Transmission measurements before and after end sealing fibre D (HC-PCF). The fibre ends were sealed for 11 weeks.

5.6 Conclusions

Using PCF's with very low OH content allows one to establish the degradation of such fibres even after only a few days of exposure to the laboratory environment. Degradation of the analysed transmission wavelengths for the smallest core PCF occurs more rapidly than that for bigger cores The rapid degradation observed for small-core fibres recalls the dramatic increase at 1383 nm also observed for small solid core PCF's [37], such degradation stands out for fibre A (1.3μm) and it is speculated that the degradation driving mechanisms are related to the silica network structure in small-core fibres and its interaction with OH. Based on the experiments performed to investigate the time degradation and localization of degradation by OH contamination in PCF's it was found that the effect on fibre degradation of the size of the cladding holes surrounding the core is clearly not dominant. The core size and number of defects on the surface and in silica bulk seem to be more important.

To further understand the origin and nature of the broad absorption at 1398 nm a more specific technique like electron paramagnetic resonance (EPR), optical or vibrational spectroscopy is necessary.

Chapter 6

Widely tunable infra-red soliton fibre source

The low loss and low OH content achieved for small-core PCF's has motivated their application in pulsed wavelength tunable sources by means of soliton self-frequency shift and a suitable cladding design to engineer the group velocity dispersion (GVD). Such sources are desirable for applications like digital-to-analogue conversion (DAC) [136–138], communications [139–141], optical coherence tomography (OCT) [142] and non linear microscopy [143]. Using an adequate low loss SC-PCF design, the wavelength of the output can be tuned by varying the input pulse power over a large range, obtaining short pulses of a few tens of femtoseconds. Part of the experimental work was carried out in collaboration with the Centre for Ultrahigh-Bandwidth Devices for Optical Systems (CUDOS) in the University of Sydney, Australia. The GVD of the low OH fibres was characterised experimentally and supported by numerical simulations.

6.1 Introduction

Solitary waves were first observed in water [144] and are known as optical solitons in the optical field. These waves can only be excited when the dependence of the refractive index with the light intensity, i.e. non-linearity, is observable. The typical intensity levels required to excite optical nonlinear effects experimentally were only possible after the first laser source [145]. The optical refractive index of any material also depends on the frequency of light, yielding different propagation velocities for different optical frequencies. This gives rise to group velocity dispersion (GVD), responsible of the temporal broadening of optical pulses

in the linear regime. In this chapter the focus will be on the optical solitons existing in the anomalous GVD regime of the fibres which are localized bright pulses [146, 147]. Strictly there is a whole family of these type of optical solitons which are parametrised by integer values of N from equation 6.1. Solitons with N=1 are the only stable ones in this family. The fundamental soliton or first order soliton (N=1) preserves its temporal and spectral shapes throughout its propagation, neglecting wave-guide losses. Therefore, unless stated otherwise the word soliton refers to the fundamental soliton only. Equation 6.1 is derived from the non linear Schroedinger equation (NLSE) [146] which accounts for the GVD and fibre non-linearity through the parameters β_2 and γ [146] respectively. A soliton exists only under the right balance between linear (GVD) and non-linear (Kerr) effects [146].

$$N^2 \equiv \frac{L_D}{L_{NL}} = \frac{T_0^2 \gamma P_0}{|\beta_2|} \tag{6.1}$$

$$L_D \equiv \frac{T_0^2}{|\beta_2|} \tag{6.2}$$

and

$$L_{NL} \equiv \frac{1}{\gamma P_0} \tag{6.3}$$

where the dispersion length L_D , and the non linear length L_{NL} are the typical length scales at which the linear and non linear effects significantly affect the pulse propagation.

Once the soliton is formed in a silica fibre it will be inherently affected by the Raman effect [146]. As a consequence of this effect the soliton is continuously transferring energy to the optical phonons (noise) propagating in the glass. Such loss of energy manifests as the down-shift of the soliton carrier frequency, yielding the well known Raman induced soliton red-shift, also known as Raman induced frequency shift (RIFS) [146]. The frequency red-shift is approximately given by [148]

$$\Omega(z) = -\frac{8 T_R |\beta_2|}{15 T_0^4} z \tag{6.4}$$

where T_R is the first moment of the nonlinear response function [146] and z the distance along the fibre.

The Raman effect is therefore the fundamental underlying physical effect that provides the wavelength tuning capability of the soliton source presented here which is limited to the anomalous GVD spectral region of the PCF.

6.2 Fibre design and characterisation

6.2.1 Numerical calculation of the group velocity dispersion

The numerical calculation of the GVD allows one to estimate the wavelength of the first and second zero group velocity dispersion wavelengths (ZGVD) λ_{ZD1} and λ_{ZD2}, that delimit the anomalous region, for a particular design of the PCF. The calculation was carried out using a commercially available finite element method (FEM) [149] software (COMSOL) [150]. The software includes graphic tools that allow one to reproduce the structure of the object, in this case the cross sectional fibre geometry, and the calculations are performed over a mesh defined by the user. The programs were exported to Matlab (linked to COMSOL) to customize and automate the calculations. A cladding structure of three rings of air holes, as that shown in Figure 6-1, was used in the program. The core radius r, and air-hole to pitch ratio d/Λ were considered for the simulations where d is the hole diameter and Λ the distance between two consecutive hole centres. The dispersion of the bulk silica glass was taken into account through the Sellmeier equation (equation 6.5) that describes dependence of refractive index with wavelength [146]

$$n^2(\omega) = 1 + \sum_{j=1}^{m} \frac{B_j \omega_j^2}{\omega_j^2 - \omega^2} \tag{6.5}$$

where ω_j is the resonant frequency and B_j is the strength of resonance. The values of the parameters, obtained for silica fibres, for m=3 are B_1=0.6961663, B_2=0.4079426, and B_3=0.8974794, and ω_1=27.537 PHz ω_2=16.205 PHz and ω_3=190.34 THz. Numerical calculations were helpful to optimise and simplify the fibre fabrication process. The fibres were fabricated according to the geometry of the numerical model necessary to achieve a wide anomalous dispersion region. The GVD was calculated numerically for core diameters ranging from 1.7 μm to 2.4 μm for different values of d/Λ, in the wavelength range 500 nm to 2500 nm. Once the fibres were fabricated, with the approximate d and Λ the core diameter, d and Λ were measured from SEM images shown in Figure 6-1. d/Λ for the 1.5 μm core fibre was 0.88 and 0.76 for the 2.3 μm core diameter was estimated by obtaining the average of the measured values of d and Λ. New numerical calculations of the GVD were obtained using the measured values of d and Λ and were compared with the GVD experimental measurements. In Figure 6-2 the numerical dispersion curves obtained for 1.5 μm core for different d/Λ are plotted. In Figure 6-3 the dispersion curves corresponding to a d/Λ=0.76 for different core diameters are plotted.

The fibres used for experiments related to the red-shift of solitons were fabricated with the annealing method described in Chapter 4. The cladding of the fibres was designed to have a wide anomalous dispersion region and low losses at 1383 nm (contained in that region).

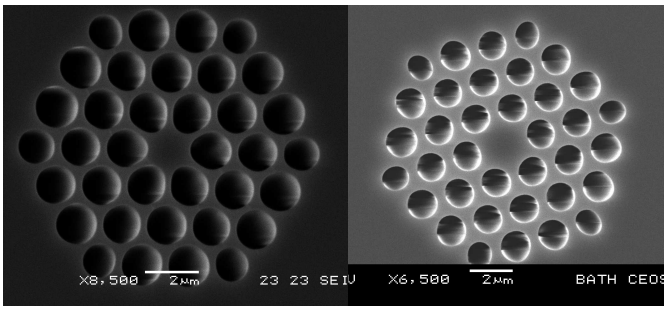

(a) (b)

Figure 6-1: SEM pictures of the fibres used in the SSFS experiments with different diameters. (a) 1.5 μm core and $d/\Lambda \approx 0.88$ and (b) 2.3 μm $d/\Lambda \approx 0.76$.

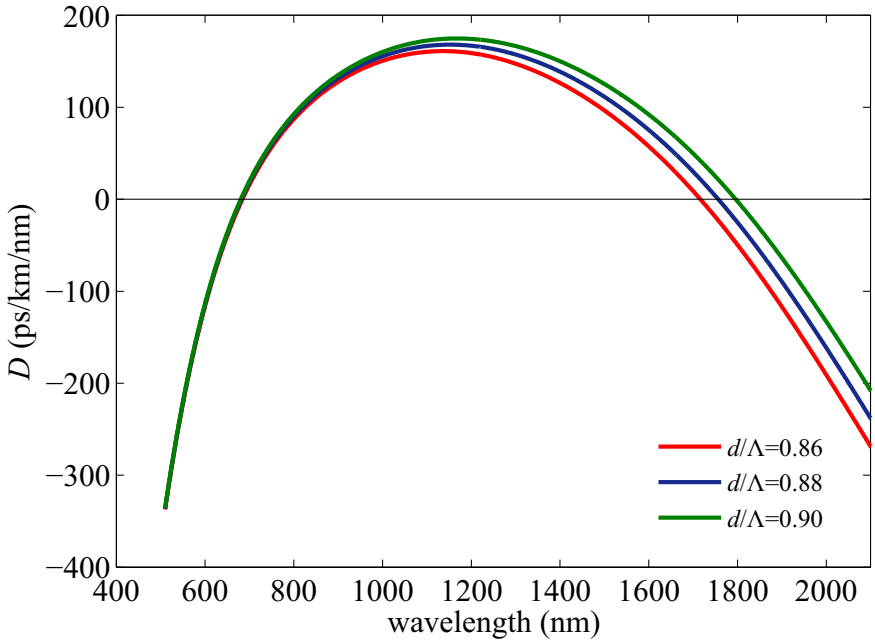

Figure 6-2: GVD curves obtained from numerical calculations for 1.5 μm core fibre and different d/Λ in the wavelength range from 500 nm to 2200 nm.

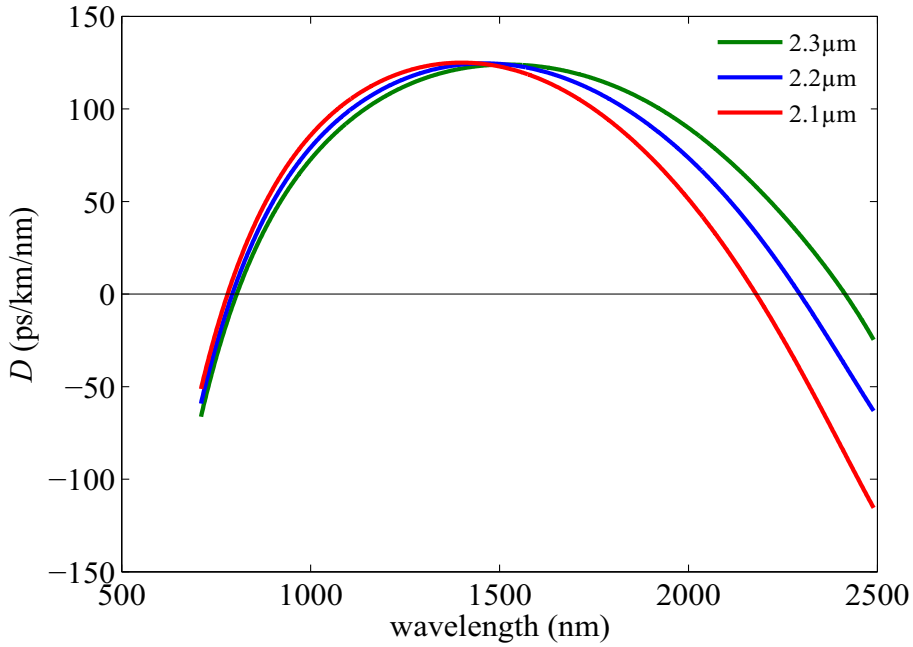

Figure 6-3: GVD curves obtained by numerical calculations for different core diameters and d/Λ=0.76 in the range wavelength from 500 nm to 2200 nm.

This allowed the SSFS span over the wide anomalous region achieving the maximum possible shift stopping just before the λ_{ZD2}, surpassing the OH absorption peak. In the following section the experimental characterisation of the fibre attenuation and GVD is presented.

6.2.2 Attenuation characterisation

The fibre attenuation was measured using a white light source (WLS) and an optical spectrum analyser (OSA) with the cutback technique. In figure 6-4 the attenuation curves obtained for the 1.5 μm and 2.3 μm core diameter in the wavelength range from 450 nm to 1700 nm are shown. The attenuation at 1383 nm is 70 dB/km for the 1.5 μm core fibre and 60 dB/km for the 2.3 μm core fibre.

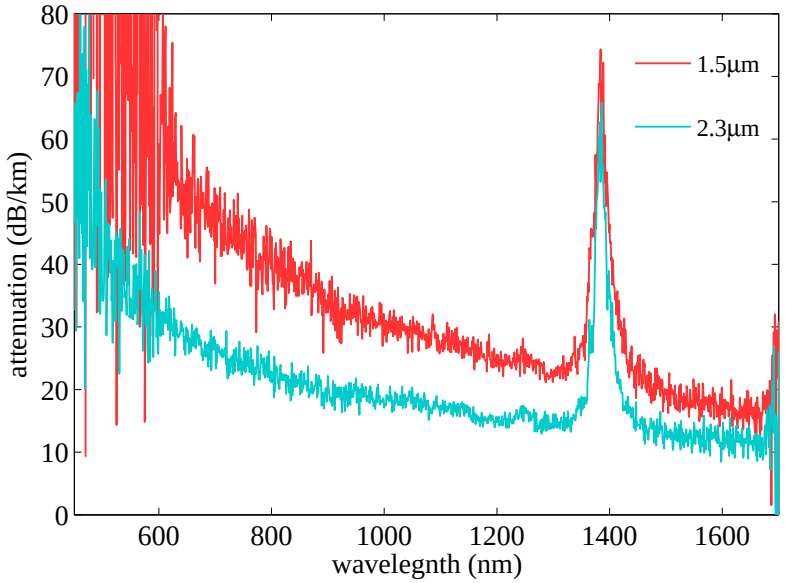

Figure 6-4: Attenuation of the fibres used in the SSFS experiments with, 1.5 μm and 2.3 μm core diameters. The fibres were fabricated using the annealing fabrication method.

6.2.3 Experimental group velocity dispersion characterisation

The GVD profile was characterised experimentally for the 1.5 μm core fibre using a set up based on a Mach-Zender interferometer. A schematic of the set up is shown in figure 6-5. A fibre based supercontinuum was used as a white light source. The beam was divided by a beam splitter (BS_1) into two arms, the test arm or fibre arm and the reference arm. The largest magnitude of the interference fringes occurred when the propagation times of the beams on the reference arm (t_{ref}) and the fibre arm (t_{fibre}) at the recombination point (BS_2) were equal (see equations 6.6 and 6.7). To compensate the delay introduced by the fibre on the fibre arm, the path length on the reference arm was modified by changing the position of the mirrors on the motorised translation stage by a length x. Both beams were recombined in a second beam splitter, and before entering the photo-receiver the beam passed through a NBP (narrow bandpass) filter that was selected to find the interference fringe position for the desired wavelength. The telescope in the reference arm was used to compensate the dispersion introduced by the objectives in the test arm, used to couple the light into the fibre and to collimate the beam afterwards. The signal from the fibre arm was usually weak, therefore it was modulated by a chopper and amplified using a lock-in amplifier. The signal from the lock-in amplifier was then sent to a PC to be analysed. An example of an interference fringe is shown in figure 6-6.

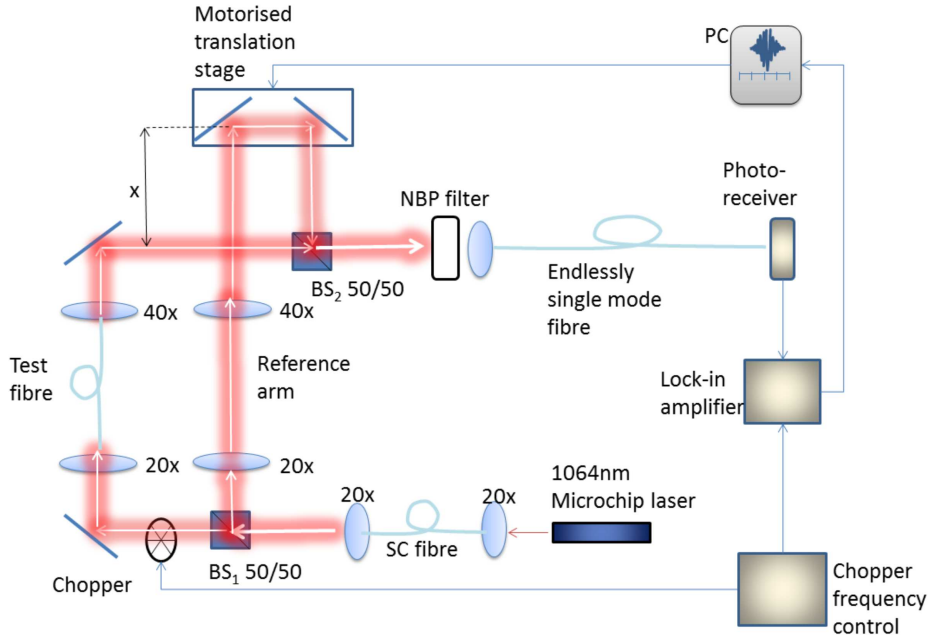

Figure 6-5: Experimental set up to characterise PCF's group velocity dispersion that includes a Mach-Zender interferometer to obtain interference fringes from 589 nm to 2150 nm.

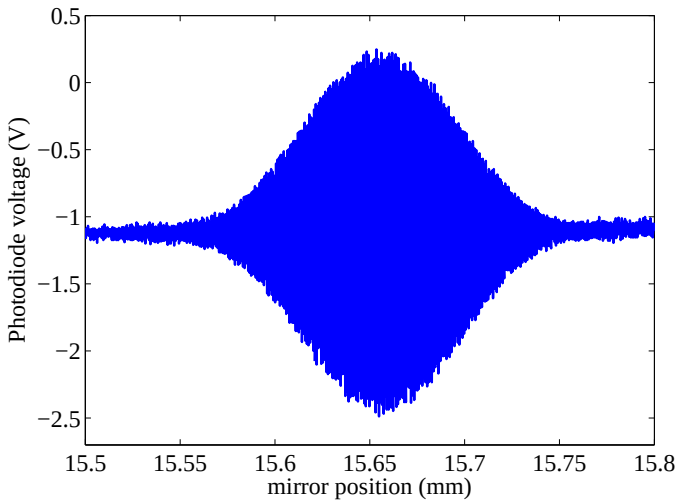

Figure 6-6: Example of an interference fringe obtained with the Mach-Zehnder interferometer. The mirror position x=15.652 is that of the maximum interference.

The propagation times in the reference and fibre arms t_{ref} and t_{fibre} respectively were calculated as follows:

$$t_{ref} = \frac{L_{x0}}{c} + \frac{2x}{c} \tag{6.6}$$

and

$$t_{fibre} = \frac{L_a}{c} + \frac{n_g L_f}{c} \tag{6.7}$$

Here L_{x0} is the path length of the reference arm when x=0, L_a is the free space path length on the fibre arm, L_f is the fibre length, x is the measured displacement to compensate the difference in optical paths and c is the speed of light in vacuum. If $t_{ref} = t_{fibre}$, then

$$n_g = \frac{2x + L_{x0} - L_a}{L_f} \tag{6.8}$$

and dispersion D is defined as [146]:

$$D = \frac{d\beta_1}{d\lambda} = -\frac{2\pi c \beta_2}{\lambda^2} \tag{6.9}$$

where β_1=$1/v_g$=n_g/c, v_g is the group velocity and n_g the group index.
D in terms of the measured displacement x is:

$$D = \frac{d\beta_1}{d\lambda} = \frac{1}{c}\frac{dn_g}{d\lambda} = \frac{2}{cL_f}\frac{dx}{d\lambda} \tag{6.10}$$

in ps/km/nm.

The curve presented in Figure 6-7 shows the experimental position of the maximum interference obtained for wavelengths ranging from 589 nm to 2150 nm (for the 1.5 μm core fibre). Experimental data were fitted to a tenth order polynomial. The characterisation of the GVD is usually done for a shorter range of wavelengths, but thanks to the low loss in the fibres used the dispersion measurements were possible in the whole anomalous GVD region, which allowed the experimental localisation of both λ_{ZD1} and λ_{ZD2}. To this effect three different photo-receiver detectors were used. A silicon PIN visible detector was used in the range from 589 nm to 1700 nm, an InGaAs PIN IR-detector was used from 1540 nm to 2000 nm (both from New Focus), and from 1750 nm to 2150 nm a high speed InGaAs detector (DET10D from Thorlabs) was used. The experimental GVD curve shown in Figure 6-8 was obtained by differentiating the fitted curve and multiplying by the factor $\frac{2}{cL_f}$ obtained in equation 6.10. Note that the n_g can also be derived experimentally if the lengths L_{x0} and L_a are known from equation 6.8. According to the experimental measurements of the 1.5 μm fibre the first and second ZGVD are λ_{ZD1}=687 nm and λ_{ZD2}=1921 nm, and those encountered by numerical simulations were λ_{ZD1}=680 nm and λ_{ZD2}=1763 nm. The GVD

derived numerically provided a good estimate of λ_{ZD1} obtained experimentally. The numerical estimation of λ_{ZD2} was located below that observed experimentally. Such discrepancy is attributable to the difference between the geometry used in the numerical calculations and that in the actual fibre and (marginally) to the uncertainty of the interference measurements. For the simulations circular holes were assumed (not accounting for the deformation of the first ring surrounding the core) and average values of d and Λ were used, which might have induced a different effective index leading to a shorter value of the λ_{ZD2}. Whilst the changes of air filling fraction modifies only slightly the λ_{ZD1} position, changes in the diameter of the fibre core shift the λ_{ZD1} position more significantly.

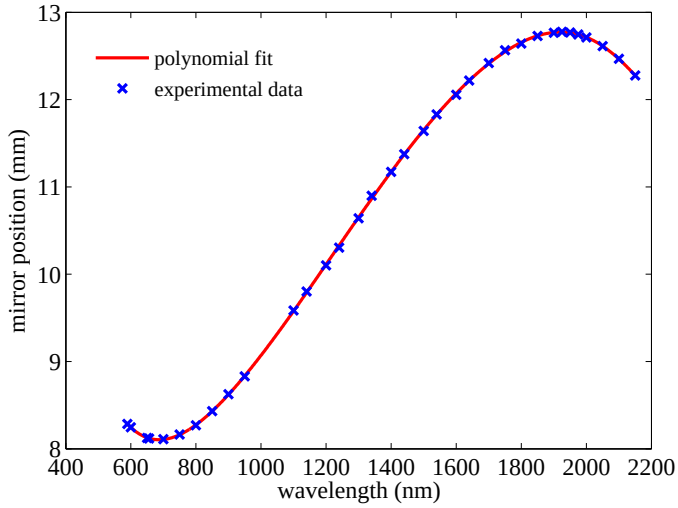

Figure 6-7: Mirror position x of the maximum interference found for a range of wavelengths from 589 nm to 2150 nm.

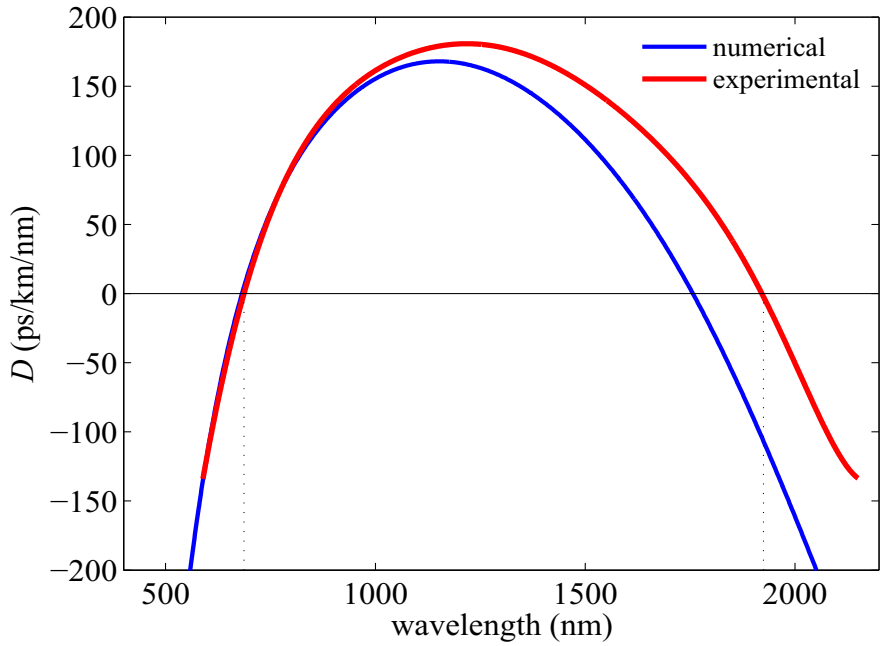

Figure 6-8: Experimental (red) and numerical (blue) GVD curves obtained for the 1.5 μm diameter SC-PCF with a d/Λ=0.88. Experimental λ_{ZD1}=687 nm and λ_{ZD2}=1921 nm, numerical λ_{ZD1}=680 nm and λ_{ZD2}=1763 nm.

6.3 Widely tunable infra-red soliton source using a low OH small-core PCF

In this section the experiment of soliton self frequency shift to prove the principle of a highly efficient tunable source over an octave carried out by S. A. Dekker at CUDOS in the University of Sydney, Australia is described. The fibre used for this purpose was the 1.5 μm core diameter fabricated and characterised by the author of this thesis, the main features of such fibre is the wide anomalous dispersion region of more than 1230 nm and low loss particularly at 1383 nm. Schematic of the set-up used is shown in Figure 6-9.

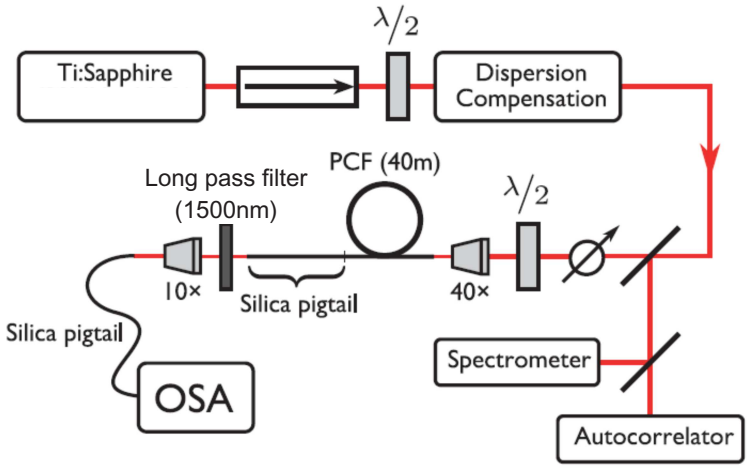

Figure 6-9: Schematic of the set up of the widely tunable infra-red soliton fibre based source using an ultra short pulse laser.

The short pulses obtained from a mode-locked Titanium-Saphire laser with a repetition rate of 83 MHz were coupled to 40 m of the 1.5 μm core PCF with a 40× microscope objective. To avoid disruptive feedback from back reflections an optical isolator was used at the output of the laser. Spectral measurements of the pulse were taken with an optical spectrometer Ocean Optics HR2000 showing that the pulses were close to transform limited. At the same time the pulse width was measured with an autocorrelator assuming a Gaussian pulse shape. Given that the maximum red-shift of the pulses is obtained at the highest input power, as the fibre was birefringent, to achieve a better performance the input polarization was optimized with a half-wave plate. The input power were tuned using a variable attenuator and the output spectra, shown in Figure 6-10, was recorded in the range from 600 nm to 1750 nm with an OSA (Ando AQ6317B) and with a Yokogawa (AQ6375) in the range from 1400 nm to 2200 nm. A long wavelength-pass filter transmitting wavelengths over 1500 nm, was used

to filter out spectral features related to higher order diffraction effects.

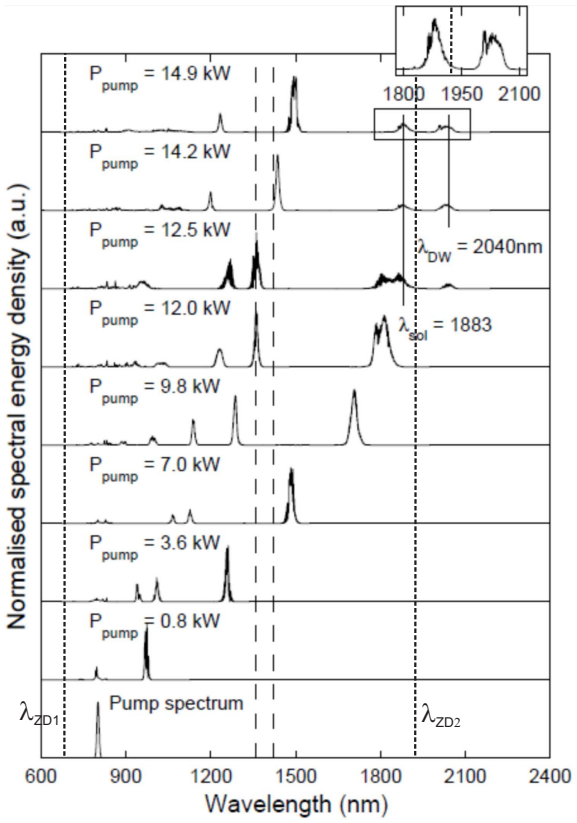

Figure 6-10: Spectra measured for a range of pump peak powers in a 40 m piece of low loss SC-PCF of 1.5 μm core diameter. The dispersive wave is observed to the right of the λ_{ZD2}=1921 nm, the soliton reaches its maximum red-shift at 1883 nm, before λ_{ZD2}.

Figure 6-10 corresponds to the spectra at the fibre output for different input powers. Because of the Raman effect the wavelength of the soliton moves continuously towards longer wavelengths as the pump peak power increases from 0.8 kW to 12.5 kW. Relative to the pump wavelength (801 nm), more than an octave red-shift is observed for the most red shifted soliton at an input power of 9.8 kW. The FWHM of the input pulse is 105 fs centred and the soliton number associated is N$\approx$ 8. The soliton experiencing the longest shift, centred at 1708 nm, contains 22% of the incident photons in the fibre which represents about 10% of the incident power and 52% of the output power. This is the longest soliton red-shift reported and the first time that a shift over an octave in SSFS experiments has been achieved [115, 151]. As the input power is increased further, illustrated in Figs. 6-10 and 6-11, the soliton keeps moving forward in wavelength until it is disrupted by the proximity

of the λ_{ZD2}=1921 nm and for powers of 12.5 kW and above the soliton reaches its shift limit at 1883 nm. Associated to this limit shift is the spectral feature at 2040 nm corresponding to the Cherenkov radiation also known as dispersive wave (DW) in the normal dispersion region. In this situation, the red-shift induced by the Raman effect is balanced by the spectral recoil effect (blue-shift in this case) associated with the emission of the dispersive waves across the λ_{ZD2} [152, 153] osberved in Figure 6-10 and represented as white circles in Fig 6-11.

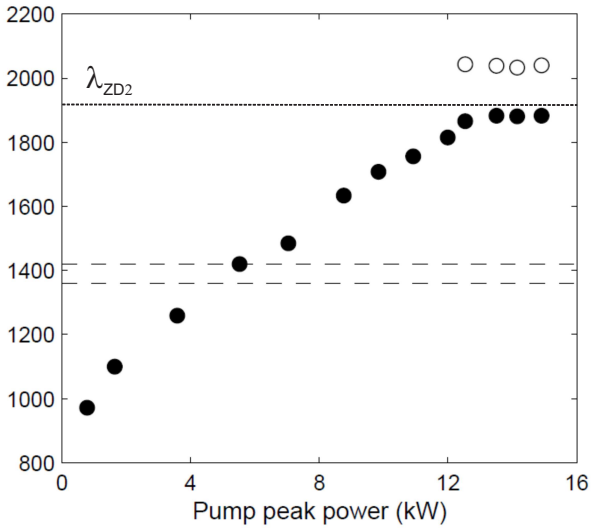

Figure 6-11: Wavelength of the most red-shifted soliton for different input powers (black circles). For powers of 12.5 kW and above the soliton stops shifting because of the close presence of the λ_{ZD2}. The DW's observed at 2040 nm are plotted as hollow circles.

6.3.1 Effects of OH contaminated PCF's on the soliton shift

As established in Chapter 5 the absorption strength of the OH peak at 1383 nm increases dramatically with time when exposed to laboratory moisture, particularly for small-core sizes. To illustrate the importance of low OH in SSFS, two experiments based on the same set up described in the previous section were carried out with 21 m of the 1.5 μm diameter fibre. For the first experiment the fibre with an absorption of 80 dB/km at 1383 nm was pumped at 785.5 nm with pulses of 100 fs FWHM of temporal width. The output spectra obtained for different input powers is presented in Figure 6-12.

Under the standard assumption that gamma and the soliton (with N=1 from equation 6.1) energy vary much more slowly than the GVD, then $T_0 \propto |\beta_2|$. Hence when the soliton is red shifted into a region of bigger $|\beta_2|$, T_0 increases proportionally and the magnitude of the red-shift Ω [146] from equation 6.4 decreases. The opposite occurs when the soliton is red

shifted into a wavelength where $|\beta_2|$ decreases leading to a larger red-shift. Despite the fact that unfavourable conditions coincide in wavelength (around 1400 nm), i.e. increasing and high $|\beta_2|$ and high OH absorption (see Figure 6-13), the soliton was observed to red-shift over an octave on the 21 m and 40 m fibre pieces as shown in Figs. 6-10 and 6-12 respectively.

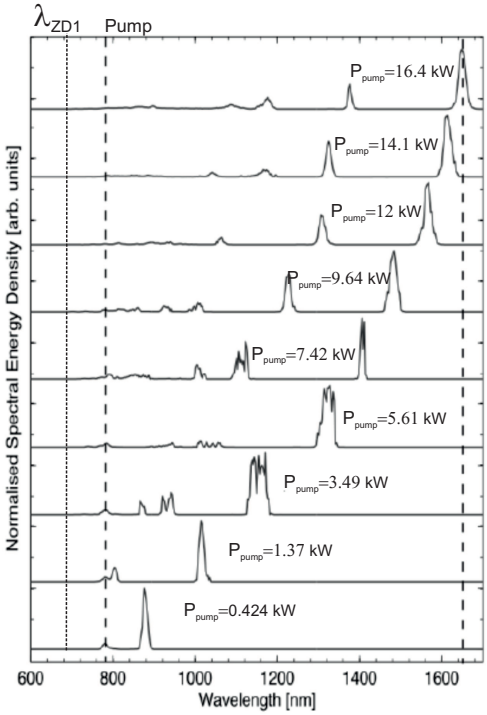

Figure 6-12: Spectra of the solitons observed at the output of the 21m fibre (1.5 μm core diameter) with low OH absorption at 1383 nm (80dB/km). The dashed line centred at 1708 nm points the wavelength of the most red-shifted soliton.

After three months of being exposed to laboratory conditions the attenuation associated with the OH absorption peak increased dramatically to 2.41 dB/m (2410 dB/km) as opposed to the 70 dB/km measured initially at this same wavelength. The same experiment was conducted by our collaborators at CUDOS, Sidney over the OH contaminated 21 m of 1.5 μm core fibre. A clear detriment in the fibre's performance is observed in the spectra showing the limited shift of the soliton in Figure 6-14. Although the soliton crosses the OH absorption barrier with increasing input power it does not move significantly with input powers above 13.3 kW, reaching its maximum red-shift at 1464 nm for 15.1 kW. In Figure 6-15 a comparison of the soliton shift with power for both experiments with low and high OH content fibres is presented.

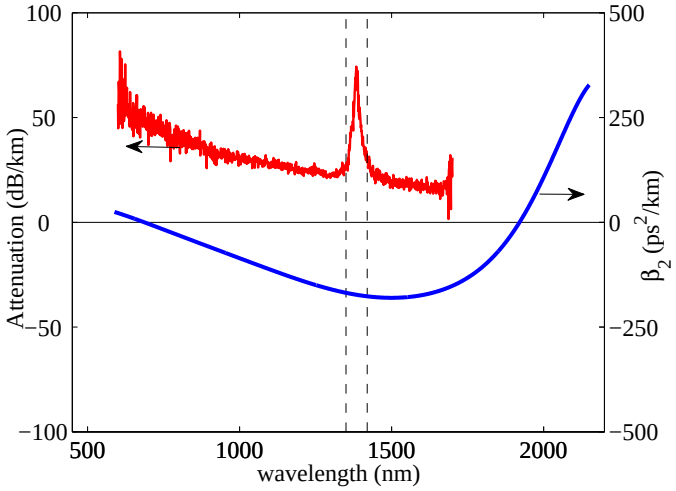

Figure 6-13: Attenuation and β_2 curves obtained experimentally for the 1.5 μm core fibre. The dashed lines indicate the approximate extent of the barrier of the absorption of the first stretching overtone in silica.

For very high losses the soliton peak power P_0 is reduced to the point where it can no longer excite non-linear effects. The Raman effect is therefore stopped by the losses and consequently the shift stops after the OH barrier as presented in Figure 6-14 for the 21 m fibre piece with an absorption of 2.41dB/m (2410 dB/km) at 1383 nm. The pulse now experiences the linear effects only and disperses generating a chirp in the pulse [154].

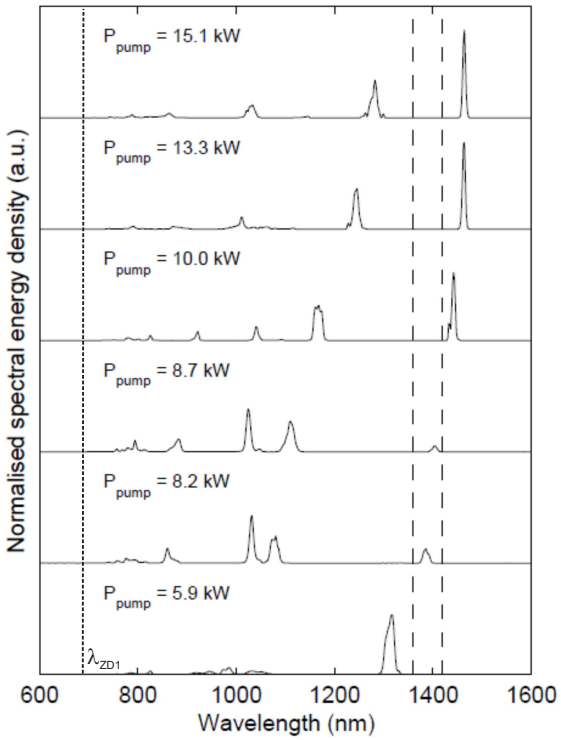

Figure 6-14: Spectra of the solitons observed at the output of the 21 m fibre (1.5 μm core diameter) exposed to OH contamination. The dashed lines around 1400 nm indicate the approximate extent of the OH absorption. The shift of the soliton is restrained due to the high absorption of the first stretching OH overtone in silica.

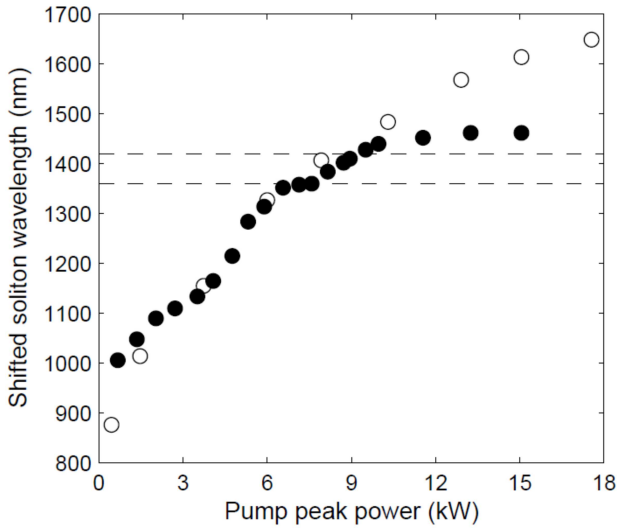

Figure 6-15: Wavelength shift of the solitons in the low OH and OH contaminated fibre (1.5 μm core) for different input powers represented as hollow circles and black circles respectively. The dashed lines around 1400 nm indicate the approximate extent of the OH absorption. The red-shift of the soliton is restrained due to the high absorption of the first stretching OH overtone in the OH contaminated fibre.

6.4 Looking for solitons beyond 2 μm

Using the 2.3 μm core fibre also with a broad anomalous region that according to the numerical simulations (see Figs. 6-3) ranges from λ_{ZD1}=806 nm to λ_{ZD2}=2413 nm the author of this thesis carried out two separate experiments at the University of Bath. One consisted of pumping 260 fs pulses from 20 MHz laser at 1064 nm to 50 m of fibre, measuring the output spectra for different input powers with a Bentham spectrometerr. The input power was adjusted by using two half-wave plates and a polarising beam splitter as shown in Figure 6-16.

In the spectra presented in Figure 6-17 a soliton shift towards long wavelengths is observed while the pump peak power increases from 7.5 kW to 27 kW, the most red-shifted soliton wavelength is 2120 nm. Above that input power the solitons spectra start to overlap. An artefact is observed around 2000 nm that corresponds to a change of grating of the spectrometer.

The second experiment consisted of maintaining the input pulse peak power constant at 53 kW, and measuring the output spectra for different fibre lengths. While maintaining the input coupled to the same fibre end, 5 m long pieces were removed from the the other end. The measurements were carried out first over 45 m then removing 5 m (2.5 m removed from

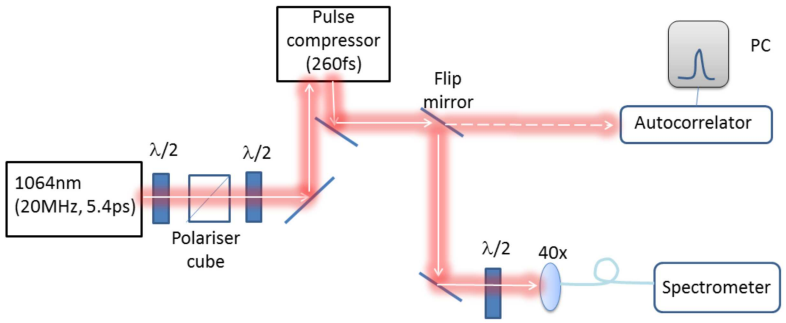

Figure 6-16: Schematic of the experimental set up used to generate solitons beyond 2 μm using a 2.3 μm fibre with d/Λ=0.76.

each end), each time measuring the output spectra until measuring over 5 m and finally over 4 m. In Figure 6-18 the evolution of the soliton for different fibre lengths is shown. There is a red-shift as the fibre length increases from 4 m to 15 m reaching 2220 nm for 53 kW input peak power. For lengths longer than 15 m solitons spectral overlap starts to appear. Another artifact is observed around 1600 nm that corresponds to a change of detector of the spectrograph.

The observed soliton red-shift was larger by 100 nm, showing the influence of absorption features as also observed for the 1383 nm absorption peak. The shift observed for the experiment with fixed fibre length and variable input power was 1056 nm, close to an octave shift relative to the pump wavelength (1064 nm). For the experiment carried out with a fixed power for different fibre lengths the shift was of at 1156 nm showing over an octave shift.

The absorption feature previously identified at 1900 nm in the experiments of degradation of PCF attenuation of section 5.3, is observed in the spectra recorded for the experiment done over 50 m of fibre. After removing 2.5 m from each end of the fibre the absorption at 1900 nm was not observed in the spectral measurements shown in Figure 6-18 with constant input power and variable fibre length. In Fig 6-19 the logarithmic scale on the intensity allows a better discernment of the changes at 1900 nm between the (superimposed) spectra before and after removing the degraded fibre ends at .

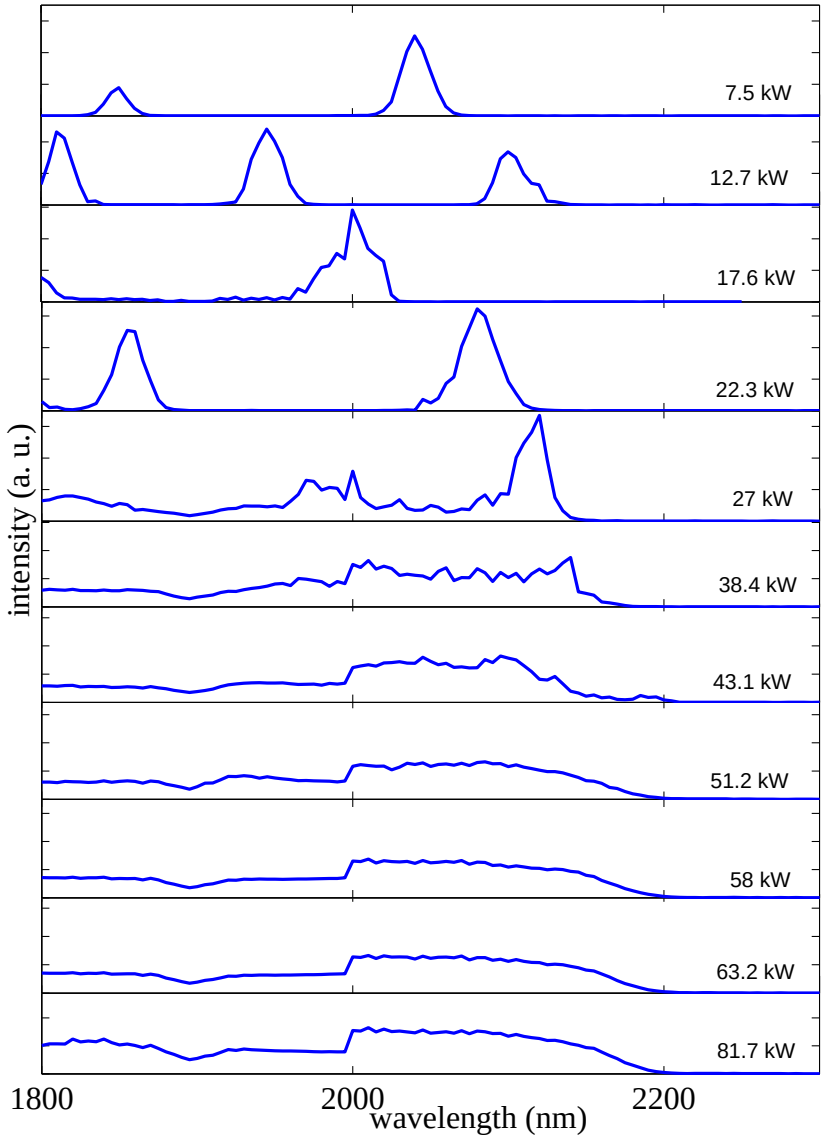

Figure 6-17: Soliton red-shift observed for a 2.3 μm core fibre with d/Λ=0.76 for different input powers after 50 m of fibre. The most red shifted soliton is observed at 2120 nm for 27 kW of peak power. The solitons spectral overlap is observed for powers above 27 kW. An absorption feature is observed at 1900 nm for peak powers of 27 kW and above.

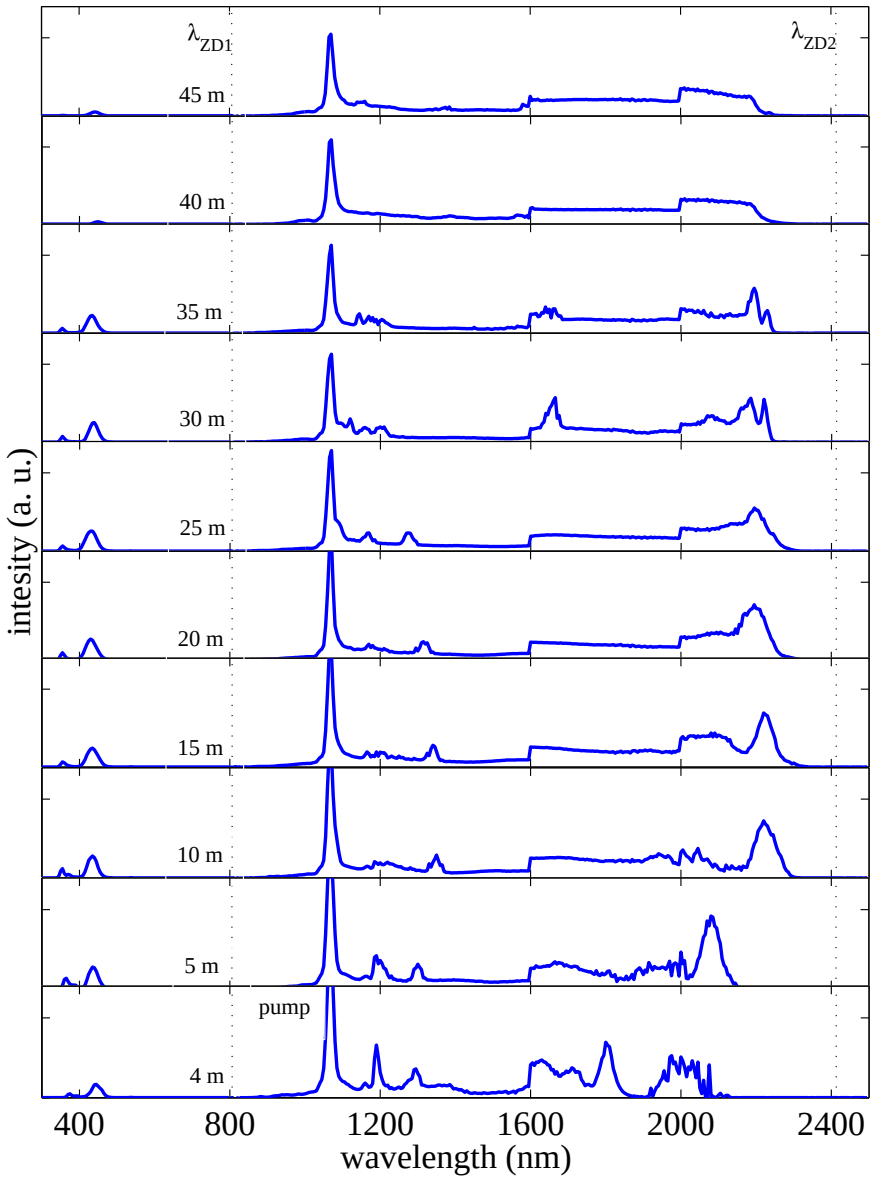

Figure 6-18: Soliton red-shift observed for 53 kW of input peak power for a 2.3 μm core fibre with d/Λ=0.76 for different fibre lengths. The most red shifted soliton is observed at 2220 nm after 15 m of fibre, for longer lengths (25 m and above) the spectral overlap of the solitons is observed. The absorption feature at 1900 nm is not observed, the contaminated ends were removed prior the experiment. The dotted lines denotes λ_{ZD1} and λ_{ZD2} estimated from numerical simulations.

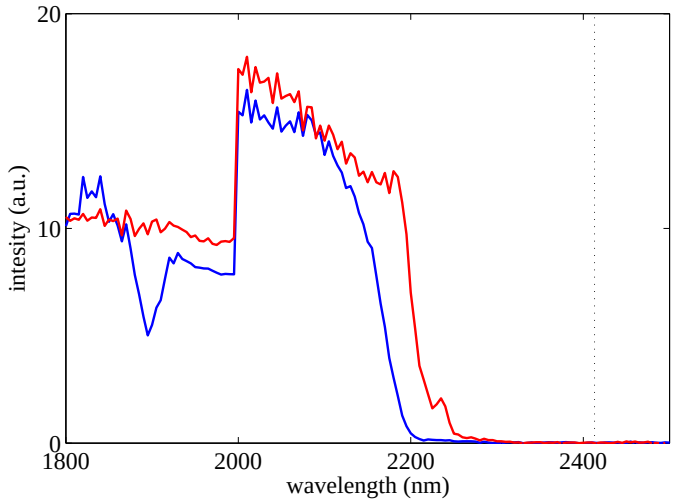

Figure 6-19: Comparison of the spectra from the same fibre. An absorption feature at 1900 nm is observed in blue for 50 m of the 2.3 μm core fibre. The spectrum in red corresponds to the same fibre after removing a 2.5 m from each end in which the feature at 1900 nm is not observed. The dotted line denotes λ_{ZD2} estimated from numerical simulations.

6.5 Conclusions

The proof of principle of SSFS over an octave using low OH solid-core PCF was demonstrated with a core diameter of 1.5 μm and OH content <1.3 ppm (corresponding to less than 80 dB/km of absorption due to OH at 1383 nm). Further improvement in the efficiency of the output could be attained by optimising the GVD profile by reducing the value of the local $|\beta_2|$ at the 1383 nm that would lead to better performance of the soliton red-shit. General low losses in the fibres used, including low absorption at the OH stretching overtones and the 1900 nm absorption band, were essential to achieve the best performance of the tunable source. SSFS was observed beyond 2 μm in a 2.3 μm core diameter fibre also with a very wide tunable range which is worth of further investigation. By using a doped fibre it would be possible to amplify the output pulses at long wavelengths.

Chapter 7

Conclusions

In this thesis low OH content SC-PCF's were successfully fabricated. Three different fabrication methods were independently implemented to reduce the final OH content of the fibre: control of atmospheric moisture, fast processing time and annealing. The exposure to the atmospheric water vapour of low OH content PCF's causes an increase in the optical absorption at OH related wavelengths. Low OH small-core SC-PCF's were used as part of infra-red femtosecond pulse sources demonstrating tuning of over an octave.

7.1 Summary of results

This thesis has focused on the reduction of OH content in SC-PCF's fibres. In Chapter 4 the effects of conditions during fibre fabrication like moisture, processing time and glass annealing, on the optical transmission of SC-PCF's at the first resonance of the OH-stretching mode in silica (1383 nm) were investigated.

In the atmospheric control method a constant N_2 flow was used whenever possible throughout the entire fabrication process to purge the moisture surrounding the glass. By reducing the contact of processed glass, i.e. capillaries, rods, and canes with the moisture present in the fabrication facilities the final levels of OH in a 5 μm SC-PCF were lowered to 8.6 dB/km, equivalent to 0.14 ppm at 1383 nm, close to the intrinsic material levels.

The reactivity of the silica surface to water vapour largely depends on the fictive temperature which is a parameter that defines glass properties like the number of defects where OH can attach. The time scale of the reaction of water vapour with the stressed silica surface is short, a few minutes after the fabrication of the material, OH attaches to the silica surface and diffuses further to the silica bulk network. The shorter the processed glass is exposed to environmental conditions (i.e. water vapour) the lowest OH content the fibres will have

and also the losses due to scattering will be lower. In the fast processing fabrication method the integration of the stacking and jacketing steps (of the *stack and draw* technique) into one step and the simple fibre design allowed a faster fabrication reducing the time glass is exposed to the atmospheric water vapour.

Low OH SC-PCF's were also obtained by the annealing fabrication method. With this method the silica network relaxes thus reducing the number of defects and OH of the fibre. Fabrication of low OH small-core PCF's was successfully achieved annealing the preform prior fibre drawing obtaining for a 2 μm core fibre an OH content of 0.19 ppm equivalent to 11.6 dB/km at 1383 nm, the lowest OH content reported to date for such diameter. The annealing method is easy to implement and the most effective method to obtain low OH SC-PCF's including the fibres derived from OH-contaminated canes. All the fabrication methods are described in detail so that low OH SC-PCF's can be reproduced.

From the investigation done in Chapter 5 on the degradation of different core-diameter PCF's exposed to the atmospheric water vapour present in laboratory is concluded that the water vapour enters through the holey structure by the fibre ends and interacts with glass forming OH groups in the fibres. The degradation is observed as an increased absorption at 1365 nm, 1383 nm and a broad absorption peak at 1398 nm. This degradation decreases exponentially from the fibre ends and towards the centre. The values of the local attenuation are remarkably higher for small-core fibre. After 6 months a few meters of the fibre ends are affected. By removing the contaminated ends it is possible to achieve the original attenuation levels. This solution can be acceptable for experiments using long lengths of fibres. On the other hand the fibre lengths commonly used in non-linear experiments are comparable to the length of the contaminated ends and although the original levels of attenuation can not be achieved, the losses using short lengths of fibre do not limit the experimental work.

Low losses particularly in the region of the first OH stretching overtone in small-core SC-PCF's made possible to achieve soliton sources in the infrared, tunable in a wide range of wavelengths, from 801 nm to 1883 nm. High OH content prevents a wide spanning of the soliton as observed in Figure 6-12, Figure 6-14 and Figure 6-15 where a fibre with contaminated ends was used. The longest wavelengths at which these solitons were observed was 2.22 μm.

Low OH SC-PCF's enable applications in nonlinear optics where low loss is crucial. The improvement in the fibres' performance is intrinsically associated with the material properties and the fabrication process. Lower losses can still be achieved by optimising fabrication processes, techniques and materials used.

7.2 Future work

Absorption at 1383 nm in SC-PCF's is directly related the number of defects which increase for smaller core diameters. Defects are sites where OH can bond to the silica matrix, a greater number leads to higher attenuation. Further work to quantify the number of defects and types of OH groups bonding in the silica core of of small-core PCF's is needed to clarify the strong relationship between absorption at 1383 nm and fibre core size.

The improvement in the fibres performance is intrinsically associated with the material and the fabrication process. Lower losses can still be achieved by optimising fabrication processes, techniques and materials used. The investigation of materials is particularly important to explore new possibilities at shorter and longer wavelengths for example glassy materials or resins less prone to defect formation [155] so to reduce reaction with water vapour (less soluble) [156], or with lower fictive temperature to reduce the Rayleigh scattering.

Spectral features observed at 900 nm, 1400 nm and 1900 nm are worth of further study to determine their origin and to identify their relation to OH and silica glass fibre defects.

To prevent or reduce fibre degradation with time further work is needed in order to obtain a long term solution whilst using the fibres for experiments or applications. For example sealing only the holes or perhaps by annealing the fibre.

Appendix A

List of publications

Journal Publications

1. **Time-dependent degradation of photonic crystal fibre attenuation around OH absorption wavelengths.**

   I. Gris-Sánchez and J. C. Knight

   Journal of Lightwave Technology **(30)** 23, (2012).

2. **Highly-efficient, octave spanning soliton self-frequency shift using a specialized photonic crystal fibre with low OH loss.**

   S. A. Dekker, A. C. Judge, R. Pant, I. Gris-Sánchez, J. C. Knight, C. Martijn de Sterke and B. J. Eggleton

   Optics Express **(19)** 18, 17767 (2011).

3. **Reducing spectral attenuation in small-core photonic crystal fibres.**

   I. Gris-Sánchez, B. J. Mangan and J. C. Knight

   Optical Materials Express **(1)** 2, 179 (2011).

Conference Publications

1. **2.04 μm Light Generation from a Ti:Sapphire Laser Using a Photonic Crystal Fiber with Low OH loss.**

   S. A. Dekker, A. C. Judge, R. Pant, I. Gris-Sánchez, J. C. Knight, C. Martijn de Sterke, and B. J. Eggleton , in *IQEC/CLEO Pacific Rim*, Sidney, 2011.

2. **Highly-Efficient, Octave Spanning Soliton Self-Frequency Shift Using a Photonic Crystal Fiber with Low OH Loss.**

   S. A. Dekker, R. Pant, A. C. Judge, C. Martijn de Sterke, B. J. Eggleton, I. Gris-Snchez and J. C. Knight, in *Frontiers in Optics*, Rochester, 2010, Post-dead line paper.

3. **Reducing Spectral Attenuation in Solid-Core Photonic Crystal Fibers.**

   I. Gris-Sánchez, B. J. Mangan and J. C. Knight, in *OFC/NFOEC*, San Diego, 2010.

Bibliography

[1] Y. Yamamoto, T. Sasaki, T. Taru, M. Hirano, S. Ishikawa, M. Onishi, E. Sasaoka, and Y. Chigusa. Water-free pure-silica-core fibre and its stability against hydrogen ageing. *Electronics Letters*, 40(22):1401–1403, 2004.

[2] K. H. Chang, D. Kalish, and M. L. Pearsall. New hydrogen aging loss mechanism in the 1400 nm window. In *Optical Fiber Communication Conference and Exposition and The National Fiber Optic Engineers Conference*, pages PD22–1, 1999.

[3] D. Colladon. On the reflections of a ray of light inside a parabolic liquid stream. *Comptes Rendus (Translated by Julian A. Carey, April 1, 1995)*, 15:800802, 1842.

[4] R. L. Mozzi and B. E. Warren. The structure of vitreous silica. *Journal of Applied Crystallography*, 2(4):164–172, 1969.

[5] G. Pacchioni, L. Skuja, and D. L. Griscom. *Defects in SiO_2 and related dielectrics: science and technology.* Kluwer Academic Publishers, USA, 2000.

[6] R. Brückner. Properties and structure of vitreous silica. I. *Journal of Non-Crystalline Solids*, 5(2):123–175, 1970.

[7] R. J. Bell and P. Dean. The structure of vitreous silica: Validity of the random network theory. *Philosophical Magazine*, 25(6):1381–1398, 1972.

[8] http://heraeus-quarzglas.com/en/home/Home.aspx.

[9] R. A. B. Devine, J.-P. Duraund, and E. Dooryhee. *Structure and imperfections in amorphous and crystalline silicon dioxide.* John Wiley & Sons, New York, 2000.

[10] H. S. Nalwa. *Silicon-based materials and devices.* Academic Press, USA, 2001.

[11] W. H. Zachariasen. The atomic arrangement in glass. *Journal of the American Chemical Society*, 196(1):3841–3851, 1932.

[12] A. Dunlop, F. Rullier-Albenque, C. Jaouen, C. Templier, and J. Davenas editors. *Materials under irradiation*. Trans Tech Publications, 1993.

[13] D. L. Griscom. On the natures of radiation-induced point defects in GeO_2-SiO_2 glasses: reevaluation of a 26-year-old ESR and optical data set. *Optical Materials*, 1(3):400–412, 2011.

[14] R. Brückner. Properties and structure of vitreous silica. II. *Journal of Non-Crystalline Solids*, 5(3):177–216, 1971.

[15] E. M. do Nascimento and C. M. Lepienski. Mechanical properties of optical glass fibers damaged by nanoindentation and water ageing. *Journal of Non-Crystalline Solids*, 352(3235):3556–3560, 2004.

[16] L. Skuja, M. Hirano, H. Hosono, and K. Kajihara. Defects in oxide glasses. *Physica Status Solidi (C)*, 2(1):15–24, 2005.

[17] D. L. Griscom. Optical properties and structure of defects in silica glass. *Journal of the Ceramic Society of Japan*, 99(10):923–942, 1991.

[18] L. Skuja. Optically active oxygen-deficiency-related centers in amorphous silicon dioxide. *Journal of Non-Crystalline Solids-crystalline Solids*, 239:16–48, 1998.

[19] D. Donadio, M. Bernasconi, and M. Boero. Ab Initio Simulations of photoinduced interconversions of oxygen deficient centers in amorphous silica. *Physical Review Letters*, 87(19):1–4, October 2001.

[20] E. J. Friebele, G. H. Sigel Jr., and D. L. Griscom. Drawing-induced defect centers in a fused silica core fiber. *Applied Physics Letters*, 28(9):516–518, 1976.

[21] P. Kaiser. Drawing-induced coloration in vitreous silica fibers. *Journal of the Optical Society of America*, 64(4):475, April 1974.

[22] G. H. Sigel Jr. and M. J. Marrone. Photoluminescence in as-drawn and irradiated silica optical fibres: an assesment of the role of non-bridging oxygen defects. *Journal of Non-Crystalline Solids*, 45:235–247, 1981.

[23] R. A. Weeks. Paramagnetic resonance of lattice defects in irradiated quartz. *Journal of Applied Physics*, 27(11):1376–1381, 1956.

[24] D. L. Griscom, E. J. Frieble, and G. H. Sigel. Observation and analysis of the primary Si hyperfine structure of the E' center in non-crystalline SiO_2. *Solid State Communications*, 15:479–483, 1974.

[25] D. L. Griscom. E'center in glassy SiO_2: Microwave saturation properties and confirmation of the primary Si hyperfine structure. *Physical Review B*, 20(5):1823–1834, 1979.

[26] R. A. Weeks and C. M. Nelson. Trapped electrons in irradiated quartz and silica: II, electron spin resonance. *Journal of the American Ceramic Society*, 43(8):399–404, 1960.

[27] H. Hanafusa, Y. Hibino, and F. Yamamoto. Formation mechanism of drawing-induced E' centers in silica optical fibers. *Journal of Applied Physics*, 58(3):1356–1361, 1985.

[28] Y. Hibino, H. Hanafusa, and S. Sakaguchi. Formation of drawing induced E' centers in optical fibres. *Japanese Journal of Applied Physics*, 24(9):1117–1121, 1985.

[29] Z. Yin and Y. Jaluria. Neck down and thermally induced defects in high-speed optical fiber drawing. *Journal of Heat Transfer*, 122(2):351–362, 2000.

[30] Y. Hibino and H Hanafusa. ESR study on E'-centers induced by optical fiber drawing process. *Japanese Journal of Applied Physics*, 22(12):L766–L768, 1983.

[31] H. Imai, K. Arai, J. Isoya, H. Hosono, Y. Abe, and H. Imagawa. Generation of E'centers and oxygen hole centers in synthetic silica glasses by γ irradiation. *Physical Review B*, 48(5):3116–3123, 1993.

[32] H. Nishikawa, R. Nakamura, R. Tohmon, Y. Ohki, Y. Sakurai, K. Nagasawa, and Y. Hama. Generation mechanism of photoinduced paramagnetic centers from preexisting precursors in high-purity silicas. *Physical Review B*, 41(11):7828–7834, 1990.

[33] Y. Hibino and H. Hanafusa. Defect structure and formation mechanism of drawing-induced absorption at 630 nm in silica optical fibers. *Journal of Applied Physics*, 60(5):1797–1801, 1986.

[34] K. Kajihara, L. Skuja, M. Hirano, and H. Hosono. Formation and decay of nonbridging oxygen hole centers in SiO_2 glasses induced by F_2 laser irradiation: In situ observation using a pump and probe technique. *Applied Physics Letters*, 79(12):1757, 2001.

[35] R. K. Iler. *The Chemistry of Silica*. John Wiley & Sons, New York, 1979.

[36] H. Kakiuchida, K. Saito, and A. J. Ikushima. Local structural relaxation around OH in silica glass. *Japanese Journal of Applied Physics*, 41(Part 1, No. 5A):2993–2998, 2002.

[37] I. Gris-Sánchez, B. J. Mangan, and J. C. Knight. Reducing spectral attenuation in small-core photonic crystal fibers. *Optical Materials Express*, 1(2):179–184, 2011.

[38] R. H. Doremus. *Diffusion of reactive molecules in solids and melts.* John Wiley & Sons, New York, 2002.

[39] L. Nuccio, S. Agnello, and R. Boscaino. Annealing of radiation induced oxygen deficient point defects in amorphous silicon dioxide: evidence for a distribution of the reaction activation energies. *Journal of physics. Condensed matter : an Institute of Physics journal*, 20(38):385215, September 2008.

[40] H. Mehrer. *Diffusion in solids.* Springer-Verlag, Berlin Heidelberg, 2007.

[41] J. E. Shelby. *Introduction to glass science and technology.* The Royal Society of Chemistry, Cambridge, 2005.

[42] P. G. Shewmon. *Diffusion in solids.* McGraw-Hill Book Company, 1963.

[43] A. Einstein. Annalen der physik. 17:549, 1905.

[44] A. Einstein. *Investigations on the theory of the brownian movement.* edited with notes by R. Fürth, Dover publications, 1956.

[45] J. Kirchhof, S. Unger, and B. Knappe. Diffusion processes in lightguide materials. In *Optical Fiber Communication Conference*, page WM1. Optical Society of America, 2000.

[46] R. H. Doremus. *Glass science.* John Wiley & Sons, New York, 1994.

[47] N. P. Bansal and R. H. Doremus. *Handbook of glass properties.* Academic Press, USA, 1986.

[48] A. J. Moulson and J. P. Roberts. Entry of water into silica glass. *Nature*, 182:200–201, 1958.

[49] K. Nassau. The diffusion of water in optical fibers. *Mat. Res. Bull.*, 13(1):67–76, 1978.

[50] (See for example), W. A. Weyl, and E. C. Marboe. *The constitution of glasses: a dynamic interpretation, Vol II: Part one.* Interscience Publishers, Inc., New York, 1964.

[51] B. J. Finlayson-Pittts. Interaction of gas-phase deuterium atoms with silica surfaces. *Journal of Physical Chemestry*, 1375(1969):3499–3501, 1982.

[52] M. J. D. Low and E. S. Argano. Sorption of activated hydrogen on vycor glass. *Journal of Vacuum Science and Technology*, 3(6):324–328, 1966.

[53] I. Langmuir. A chemically active modification of hydrogen. *Journal of the American Chemical Society*, 186(7):1310–1325, 1912.

[54] O. Sneh and S. M. George. Thermal stability of hydroxyl groups on a well-defined silica surface. *The Journal of physical chemistry*, 99(13):4639–4647, 1995.

[55] K. M. Davis and M. Tomozawa. Water diffusion into silica glass: Structural changes in silica glass and their effect on water solubility and diffusivity. *Journal of Non-Crystalline Solids*, 185(3):203–220, June 1995.

[56] R. H. Doremus, ed., J. W. Mitchell, R. C. DeVries, Roberts R. W., and P. Cannon. *Reactivity of Solids*. John Wiley & Sons, New York, 1969.

[57] G. J. Roberts and J. P. Roberts. Influence of thermal history on the solubility and diffusion of 'water' in silica glass. *Physics and Chemestry of Glasses*, 5:391–401, 1964.

[58] P. B. McGinnis and J. E. Shelby. Diffusion of water in vitreous silica. *Journal of Non-Crystalline Solids*, 179(94):185–193, 1994.

[59] A. Q. Tool. Relation between inelastic deformability and thermal expansion of glass in its annealing range. *Journal of the American Ceramic Society*, 29(9):240–253, 1946.

[60] D.-L. Kim, M. Tomozawa, S. Dubois, and G. Orcel. Fictive temperature measurement of single-mode optical-fiber core and cladding. *Journal of Lightwave Technology*, 19(8):1155–1158, 2001.

[61] M. Yamaguchi, K. Saito, and A. Ikushima. Fictive-temperature-dependence of photoinduced self-trapped holes in a-SiO_2. *Physical Review B*, 68(15):153204–1–153204–4, 2003.

[62] G. E. Walrafen. Raman spectra from SiOH groups in solid optical fibers. *The Journal of Chemical Physics*, 62(1):297–298, 1975.

[63] G. E. Walrafen and S. R. Samanta. Infrared absorbance spectra and interactions involving OH groups in fused silica. *The Journal of Chemical Physics*, 69(1):493–495, 1978.

[64] J. Stone and G. E. Walrafen. Overtone vibrations of OH groups in fused silica optical fibers. *The Journal of Chemical Physics*, 76(4):1712–1722, 1982.

[65] Y. Yokomachi, R. Tohmon, K. Nagasawa, and Y. Ohki. Hydrogen bond of OH-groups in silica glass and its relation to the 1.39 μm absorption. *Journal of Non-Crystalline Solids*, 95-96:663–670, 1987.

[66] K. M. Davis and M. Tomozawa. An infrared spectroscopic study of water-related species in silica glasses. *Journal of Non-Crystalline Solids*, 201(3):177–198, 1996.

[67] V. G. Plotnichenko, V. O. Sokolov, and E. M. Dianov. Hydroxyl groups in high-purity silica glass. *Inorganic Materials*, 36(4):404–410, 2000.

[68] M. Bredol, D. Leers, L. Bosselaar, and M. Hutjens. Improved model for OH absorption in optical fibers. *Journal of Lightwave Technology*, 8(10):1536–1540, 1990.

[69] R. T. Bise and D. J. Trevor. Surface absorption in microstructured optical fibers. *Optical Fiber Communication Conference and Exposition and The National Fiber Optic Engineers Conference*, page WI4, 2004.

[70] A. Burneau and C. Carteret. Near infrared and ab initio study of the vibrational modes of isolated silanol on silica. *Physical Chemistry Chemical Physic*, 2(14):3217–3226, 2000.

[71] J. Hecht. *City of light*. Oxford University Press, 1999.

[72] K. Nagayama, M. Kakui, M. Matsui, I. Saitoh, and Y. Chigusa. Ultra-low-loss (0.1484 dB/km) pure silica core fibre and extension of transmission distance. *Electronics Letters*, 38(20):1168–1169, 2002.

[73] J. C. Knight, T. A. Birks, P. St. J. Russell, and D. M. Atkin. All-silica single-mode optical fiber with photonic crystal cladding. *Optics Letters*, 21(19):1547–1549, 1996.

[74] P. Russell. Photonic crystal fibers. *Science*, 299(5605):358–362, 2003.

[75] J. C. Knight. Photonic crystal fibres. *Nature*, 424(6950):847–51, 2003.

[76] P. St. J. Russell. Photonic-Crystal Fibers. *Journal of Lightwave Technology*, 24(12):4729–4749, 2006.

[77] T. A. Birks, J. C. Knight, and P. St. J. Russell. Endlessly single-mode photonic crystal fiber. *Optics Letters*, 22(13):961–963, 1997.

[78] J. C. Knight, J. Broeng, T. A. Birks, and P. St. J. Russell. Photonic band gap guidance in optical fibers. *Science*, 282(5393):1476–1478, 1998.

[79] R. F. Cregan, B. J. Mangan, J. C. Knight, T. A. Birks, P. St. J. Russell, P. J Roberts, and D. C. Allan. Single-mode photonic band gap guidance of light in air. *Science*, 285(5433):1537–1539, 1999.

[80] T. M. Monro, K. M. Kiang, J. H. Lee, K. Frampton, Z. Yusoff, R. Moore, J. Tucknott, D. W. Hewak, H. N. Rutt, and D. J. Richardson. High nonlinearity extruded single-mode holey optical fibers. In *Optical Fiber Communication Conference and Exposition and The National Fiber Optic Engineers Conference*, pages FA1–1, 2002.

[81] T. Hasegawa, E. Sasaoka, M. Onishi, M. Nishimura, Y. Tsuji, and M. Koshiba. Hole-assisted lightguide fiber for large anomalous dispersion and low optical loss. *Optics Express*, 9(13):681–686, 2001.

[82] R. T. Bise and D. J. Trevor. Sol-gel derived microstructured fiber: fabrication and characterization. In *Optical Fiber Communication Conference and Exposition and The National Fiber Optic Engineers Conference*, page OWL6, 2005.

[83] K. Yoshida, Y. Furui, S. Sentsui, and T. Kuroha. Loss factors in optical fibres. *Optical and Quantum Electronics*, 13(1):85–89, 1981.

[84] O. Humbach, H. Fabian, U. Grzesik, U. Haken, and W. Heitmann. Analysis of OH absorption bands in synthetic silica. *Journal of Non-Crystalline Solids*, 203:19–26, 1996.

[85] M. C. Phan-Huy, J.-M. Moison, J. A. Levenson, S. Richard, G. Melin, M. Douay, and Y. Quiquempois. Surface roughness and light scattering in a small effective area microstructured fiber. *Journal of Lightwave Technology*, 27(11):1597–1604, 2009.

[86] P. J. Roberts, F. Couny, H. Sabert, B. J. Mangan, T. A. Birks, J. C. Knight, and P. St. J. Russell. Loss in solid-core photonic crystal fibers due to interface roughness scattering. *Optics Express*, 13(20):7779–7793, 2005.

[87] R. H. Stolen. Raman oscillation in glass optical waveguide. *Applied Physics Letters*, 20(2):62, 1972.

[88] R. H. Stolen and E. P. Ippen. Raman gain in glass optical waveguides. *Applied Physics Letters*, 22(6):276, 1973.

[89] E. P. Ippen and R.H. Stolen. Stimulated Brillouin scattering in optical fibers. *Applied Physics Letters*, 21(11):539–540, 1972.

[90] R. G. Smith. Optical power handling capacity of low loss optical fibers as determined by stimulated Raman and Brillouin scattering. *Applied Optics*, 11(11):2489–2494, 1972.

[91] D. Ferrarini, L. Vincetti, M. Zoboli, A. Cucinotta, and S. Selleri. Leakage properties of photonic crystal fibers. *Optics Express*, 10(23):1314–1319, 2002.

[92] T. P. White, R. C. McPhedran, C. Martijn de Sterke, L. C. Botten, and M. J. Steel. Confinement losses in microstructured optical fibers. *Optics Letters*, 26(21):1660–1662, 2001.

[93] K. Saitoh and M. Koshiba. Confinement losses in air-guiding photonic bandgap fibers. *Photonics Technology Letters, IEEE*, 15(2):236–238, 2003.

[94] T. Sørensen, J. Broeng, A. Bjarklev, E. Knudsen, and S. E. Barkau Libori. Macrobending loss properties of photonic crystal fibre. *Electronics Letters*, 37(5):287–289, 2001.

[95] N. A. Mortensen and J. R. Folkenberg. Low-loss criterion and effective area considerations for photonic crystal fibres. *Journal of Optics A: Pure and Applied Optics*, 5(3):163–167, 2003.

[96] J. C. Baggett, T. M. Monro, J. R. Hayes, V. Finazzi, and D. J. Richardson. Improving bending losses in holey fibers. In *Optical Fiber Communication Conference and Exposition and The National Fiber Optic Engineers Conference*, page OWL4, 2005.

[97] G. Cancellieri and U. Ravaioli. *Measurments of optical fibres and devices: theory and experiments*. Artech house, 1984.

[98] Manfred Börner. Mehrstufiges Übertragungssystem für pulscodemodulation dargestellte nachrichten. Telefunken Patentverwertungsgesellschaft m.b.H, 11 1967. DE 1254513.

[99] K. C. Kao and G. A. Hockham. Dielectric-fibre surface waveguides for optical frequencies. *Optoelectronics, IEE*, 113(7):1151–1158, 1966.

[100] F. P. Kapron, D. B. Keck, and R. D. Maurer. Radiation losses in glass optical waveguides. *Applied Physics Letters*, 17(10):423–425, 1970.

[101] J. B. MacChesney, P. B. O'Connor, F. V. DiMarcello, J. R. Sompson, and P. D. Lazay. Preparation of low loss optical fibers using simultaneous vapor phase deposition and fusion. In *10th International Congress of Glass*, volume 6, pages 40–51, Kyoto, Japan, 1974.

[102] M. Horiguchi and H. Osanai. Spectral losses of low-OH-content optical fibres. *Electronics Letters*, 12(12):310–312, 1976.

[103] T. Miya, Y. Terunuma, T. Hosaka, and T. Miyashita. Ultimate low-loss single-mode fibre at 1.55 μm. *Electronics Letters*, 15(4):106–108, 1979.

[104] G. A. Thomas, B. I. Shraiman, P. F. Glodis, and M. J. Stephens. Towards the clarity limit in optical fibre. *Nature*, 404(6775):262–264, 2000.

[105] K. H. Chang, J. P. Fletcher, J. Rennell, A. Nakajima, J. Vydra, and R. Sattmann. Next generation fiber manufacturing for the highest performing conventional single mode fiber. In *Optical Fiber Communication Conference and Exposition and The National Fiber Optic Engineers Conference*, page JWA5, 2005.

[106] K. H. Chang. Alkali impurities and the long-wavelength hydrogen-induced aging loss in Ge-doped silica fibers. In *Optical Fiber Communication Conference and Exposition and The National Fiber Optic Engineers Conference*, page OThQ3, 2005.

[107] K. Saito, M. Yamaguchi, H. Kakiuchida, A. J. Ikushima, K. Ohsono, and Y. Kurosawa. Limit of the Rayleigh scattering loss in silica fiber. *Applied Physics Letters*, 83(25):5175–5177, 2003.

[108] H. Kanamori, H. Yokota, G. Tanaka, M. Watanabe, Y. Ishiguro, I. Yoshida, T. Kakii, S. Itoh, Y. Asano, and S. Tanaka. Transmission characteristics and reliability of pure-silica-core single-mode fibers. *Journal of Lightwave Technology*, 4(8):1144–1150, 1986.

[109] A. Kudlinski, G. Bouwmans, O. Vanvincq, Y. Quiquempois, A. Le Rouge, L. Bigot, G. Mélin, and A. Mussot. White-light cw-pumped supercontinuum generation in highly GeO_2-doped-core photonic crystal fibers. *Optics Letters*, 34(23):3631–3633, 2009.

[110] B. A. Cumberland, J. C. Travers, S. V. Popov, and J. R. Taylor. Toward visible cw-pumped supercontinua. *Optics Letters*, 33(18):2122–2124, 2008.

[111] J. C. Travers, R. E. Kennedy, S. V. Popov, J. R. Taylor, H. Sabert, and B. Mangan. Extended continuous-wave supercontinuum generation in a low-water-loss holey fiber. *Optics Letters*, 30(15):1938–1940, 2005.

[112] C. Guo, S. Ruan, P. Yan, E. Pan, and H. Wei. Flat supercontinuum generation in cascaded fibers pumped by a continuous wave laser. *Optics Express*, 18(11):11046–11051, 2010.

[113] W. J. Wadsworth, N. Joly, J. C. Knight, T. A. Birks, F. Biancalana, and P. St. J. Russell. Supercontinuum and four-wave mixing with Q-switched pulses in endlessly single-mode photonic crystal fibres. *Optics Express*, 12(2):299–309, 2004.

[114] J. M. Stone and J. C. Knight. Visibly "white" light generation in uniform photonic crystal fiber using a microchip laser. *Optics Express*, 16(4):2670–2675, 2008.

[115] S. A. Dekker, A. C. Judge, R. Pant, I. Gris-Sánchez, J. C. Knight, C. Martijn de Sterke, and B. J. Eggleton. Highly-efficient, octave spanning soliton self-frequency shift using a specialized photonic crystal fiber with low OH loss. *Optics Express*, 19(18):17766–17773, 2011.

[116] J. D. Harvey, R. Leonhardt, S. Coen, G. K. L. Wong, J. C. Knight, W. J. Wadsworth, and P. St J. Russell. Scalar modulation instability in the normal dispersion regime by use of a photonic crystal fiber. *Optics Letters*, 28(22):2225–2227, 2003.

[117] N. V. Wheeler, M. N. Petrovich, R. Slavík, N. Baddela, E. Numkam, J. R. Hayes, D. R. Gray, F. Poletti, and D. J. Richardson. Wide-bandwidth, low-loss, 19-cell hollow core photonic band gap fiber and its potential for low latency data transmission. In *Optical Fiber Communication Conference and Exposition and The National Fiber Optic Engineers Conference*, volume 1, page PDP5A.2, 2012.

[118] K. Tajima, J. Zhou, K. Kurokawa, and K. Nakajima. Low water peak photonic crystal fibers. In *Optical Fiber Communication Conference and Exposition and The National Fiber Optic Engineers Conference*, pages 523–524, 2002.

[119] K. Tajima. Low loss PCF by reduction of hole surface imperfection. In *33rd European Conference and Exhibition on Optical Communication*, pages 1–2, 2007.

[120] A. Monteville, D. Landais, O. LeGoffic, D. Tregoat, N. J. Traynor, T. N. Nguyen, S. Lobo, T. Chartier, and J.-C. Simon. Low loss, low OH, highly non-linear holey fiber for Raman amplification. In *Conference on Lasers and Electro-Optics*, page CMC1, 2006.

[121] http://www.nktphotonics.com/fiber.

[122] I. Gris-Sánchez, B. J. Mangan, and J. C Knight. Reducing spectral attenuation in solid-core photonic crystal fibers. In *Optical Fiber Communication Conference and Exposition and The National Fiber Optic Engineers Conference*, page OWK1, 2010.

[123] R. H. Stolen and G. E. Walrafen. Water and its relation to broken bond defects in fused silica. *The Journal of Chemical Physics*, 64(6):2623–2631, 1976.

[124] Y. Morimoto, S. Nozawa, and H. Hosono. Effect of Xe_2 light (7.2 eV) on the infrared and vacuum ultraviolet absorption properties of hydroxyl groups in silica glass. *Physical Review B*, 59(6):4066–4073, 1999.

[125] L. Nuccio, S. Agnello, and R. Boscaino. Intrinsic generation of OH groups in dry silicon dioxide upon thermal treatments. *Applied Physics Letters*, 93(15):151906–1–151906–3, 2008.

[126] F. Benabid, G. Antonopoulos, J. C. Knight, and P. St. J. Russell. Applications of hollow-core photonic crystal fiber. In *Conference on Lasers and Electro- Optics/International Quantum Electronics Conference*, page CTuC3, 2003.

[127] T. M. Monro, W. Belardi, K . Furusawa, J. C. Baggett, N. G. R. Broderick, and D. J. Richardson. Sensing with microstructured optical fibres. *Measurement Science and Technology*, 12(7):854–858, 2001.

[128] D. Monzón-Hernández, J. Villatoro, D. Talavera, and D. Luna-Moreno. Optical-fiber surface-plasmon resonance sensor with multiple resonance peaks. *Applied Optics*, 43(6):1216–1220, 2004.

[129] A. Wang, A. Docherty, B. T. Kuhlmey, F. M. Cox, and M. C. J. Large. Side-hole fiber sensor based on surface plasmon resonances. *Optics Letters*, 34(24):3890–3892, 2009.

[130] Y.-Q. Li, S.-S. and Huang, Z.-D. and Song, X.-S. and Zhang, S.-Y. and Zhong, Q. and Xu, F. and Lu. Photonic crystal fibre based high temperature sensor with three-beam path interference. *Electronics Letters*, 46(20):1394 –1396, 2010.

[131] D. Callaghan, M McGrath, G. Rajan, Y. Semenova, G. Farrell, and E. Coyle. Comparing FBG and PCF force sensors in a laparoscopic smart surgical scissor instrument. In *Joint Workshop on New Technologies for Computer/Robot Assisted Surgery*, pages 1–4, 2011.

[132] J. P. Carvalho, H. Lehmann, H. Bartelt, F. Magalhães, R. Amezcua-Correa, J. L. Santos, J. Van Roosbroeck, F. M. Araújo, L. A. Ferreira, and J. C. Knight. Remote system for detection of low-levels of methane based on photonic crystal fibres and wavelength modulation spectroscopy. *Journal of Sensors*, 2009:1–10, 2009.

[133] S. H. Aref, R. Amezcua-Correac, J. P. Carvalho, O. Frazão, J. L. Santos, F. M. Araújo, H. Latifi, F. Farahi, L. A. Ferreira, and J. C. Knight. Spectral characterization of a photonic bandgap fiber for sensing applications. *Applied Optics*, 49(10):1870–1875, 2010.

[134] I. Gris-Sanchez and J. C. Knight. Time-dependent degradation of photonic crystal fiber attenuation around OH absorption wavelengths. *Journal of Lightwave Technology*, 30(23):3597–3602, 2012.

[135] J. A. Curcio, L. F. Drummeter, and G. L. Knestrick. An atlas of the absorption spectrum of the lower atmosphere from 5400 Å to 8520 Å. *Applied Optics*, 3(12):1401–1409, 1964.

[136] T. Konishi, K. Tanimura, K. Asano, Y. Oshita, and Y. Ichioka. All-optical analog-to-digital converter by use of self-frequency shifting in fiber and a pulse-shaping technique. *Journal of the Optical Society of America B*, 19(11):2817–2823, 2002.

[137] C. Xu and X. Liu. Photonic analog-to-digital converter using soliton self-frequency shift and interleaving spectral filters. *Optics Letters*, 28(12):986–988, 2003.

[138] G. C. Valley. Photonic analog-to-digital converters. *Optics Express*, 15(5):1955–1982, 2007.

[139] S. Oda and A. Maruta. All-optical tunable delay line based on soliton self-frequency shift and filtering broadened spectrum due to self-phase modulation. *Optics Express*, 14(17):7895–7902, 2006.

[140] M. Kato, K. Fujiura, and T. Kurihara. Asynchronous all-optical bit-by-bit self-signal recognition and demultiplexing from overlapped signals achieved by self-frequency shift of Raman soliton. *Electronics Letters*, 40(6):2–3, 2004.

[141] J. H. Lee, J. van Howe, C. Xu, and X. Liu. Soliton self-frequency shift: experimental demonstrations and applications. *IEEE Journal of Selected Topics in Quantum Electronics*, 14(3):713–723, 2008.

[142] K. Sumimura, Y. Genda, T. Ohta, K. Itoh, and N. Nishizawa. Quasi-supercontinuum generation using 1.06 μm ultrashort-pulse laser system for ultrahigh-resolution optical-coherence tomography. *Optics Letters*, 35(21):3631–3633, 2010.

[143] R. Aviles-Espinosa, G. Filippidis, C. Hamilton, G. Malcolm, K. J. Weingarten, T. Südmeyer, Y. Barbarin, U. Keller, S. Santos, D. Artigas, and P. Loza-Alvarez. Compact ultrafast semiconductor disk laser: targeting GFP based nonlinear applications in living organisms. *Biomedical Optics Express*, 2(4):739–747, 2011.

[144] J. S. Russell. *Report of 14th Meeting of the British Association for Advancement of Science*, pages 311–390. York, September, 1844.

[145] T. H. Maiman. Stimulated optical radiation in ruby. *Nature*, 187(4736):493–494, 1960.

[146] G. P. Agrawal. *Non linear fibre optics*. Academic Press, San Diego, fourth edition, 2007.

[147] Y. S. Kivshar and G. P. Agrawal. *Optical solitons. From fibers to photonic crystals*. Academic Press, San Diego, 2003.

[148] J. P. Gordon. Theory of the soliton self-frequency shift. *Optics Letters*, 11(10):662–664, 1986.

[149] J. Jin. *The finite element method*. John Wiley & Sons, New York, 2002.

[150] http://www.uk.comsol.com/.

[151] S. A. Dekker, R. Pant, A. C. Judge, C. Martijn de Sterke, B. J. Eggleton, I. Gris-Sánchez, and J. C. Knight. Highly-efficient, octave spanning soliton self-frequency shift using a photonic crystal fiber with low OH loss. In *Frontiers in Optics/ Laser Science*, page PDPB6, 2010.

[152] D. V. Skryabin, F. Luan, J. C. Knight, and P. St J. Russell. Soliton self-frequency shift cancellation in photonic crystal fibers. *Science*, 301(5640):1705–1708, 2003.

[153] D.V. Skryabin and A. V. Gorbach. Colloquium: looking at a soliton through the prism of optical supercontinuum. *Reviews of Modern Physics*, 82(2):1287–1299, 2010.

[154] J. Santhanam and G. P. Agrawal. Raman-induced spectral shifts in optical fibers: general theory based on the moment method. *Optics Communications*, 222(16):413 – 420, 2003.

[155] H. Hosono and Y. Ikuta. Interaction of F_2 excimer laser with SiO_2 glasses: Towards the third generation of synthetic SiO_2 glasses. *Nuclear Instruments and Methods in Physics Research Section B: Beam Interactions with Materials and Atoms*, 166-167:691–697, 2000.

[156] D. Montarnal, M. Capelot, F. Tournilhac, and L. Leibler. Silica-like malleable materials from permanent organic networks. *Science*, 334(6058):965–968, 2011.